Optomechanotransduction and Optorheology

Luo, Justin C.

2018

UNIVERSITY OF CALIFORNIA,
IRVINE

Optomechanotransduction and Optorheology

DISSERTATION

submitted in partial satisfaction of the requirements
for the degree of

DOCTOR OF PHILOSOPHY

in Biomedical Engineering

by

Justin C. Luo

Dissertation Committee:
Professor Vasan Venugopalan, Chair
Professor Elliot L. Botvinick, Co-Chair
Assistant Professor Michelle A. Digman

2018

DEDICATION

To

my mother, father, and brother

TABLE OF CONTENTS

LIST OF FIGURES

LIST OF TABLES

LIST OF ABBREVIATIONS

Roman

2-APB	2-aminoethoxydiphenyl borate
2D	two-dimensional
3D	three-dimensional
AFM	atomic force microscopy
ATP	adenosine triphosphate
CCD	charge-coupled device
DAG	diacylglycerol
DMSO	dimethyl sulfoxide
EBM-2	endothelial basal medium-2
ECM	extracellular matrix
EGM-2	endothelial growth medium-2
EGTA	egtazic acid
ER	endoplasmic reticulum
FBS	fetal bovine serum
GPCRs	G Protein-Coupled Receptors
HBSS-	Hank's Balanced Salt Solution without Ca^{2+} and Mg^{2+} ions
HBSS+	Hank's Balanced Salt Solution with Ca^{2+} and Mg^{2+} ions
HEPES	4-(2-hydroxyethyl)-1-piperazineethanesulfonic acid
HHBSS-	HEPES buffered HBSS- supplemented with Mg^{2+} ions
HHBSS+	HEPES buffered HBSS+

HTS	high-throughput screening
HUVECs	human umbilical vein endothelial cells
IBA	inverse Bremsstrahlung absorption
ICCD	intensified charge-coupled device
IP_3	inositol 1,4,5-triphosphate
IP_3R	inositol 1,4,5-triphosphate receptor
LICR	laser-induced cavitation rheology
MECs	mammary epithelial cells
PEG (600) DA	polyethylene glycol (600) diacrylate
PES	polyethersulfone
PIP_2	phosphatidylinositol 4,5-biphosphate
PLCβ	phospholipase C β
PP2	phosphoprotein phosphatase 2
R&D	research and development
ssGPCRs	stretch-sensitive G Protein-Coupled Receptors
UV	ultraviolet

Greek

µCB	microcavitation bubble
µM	micromolar
µTsunami	microtsunami

NOMENCLATURE

Roman

b	rigid body translation vector, [m]
B	Tait equation parameter, [Pa]
c	speed of sound, [m $\cdot$ s^{-1}]; Cauchy deformation tensor, [–]
c_∞	sound velocity in the fluid far from the bubble at infinity, [m $\cdot$ s^{-1}]
C	sonic velocity at the bubble wall, [m $\cdot$ s^{-1}]
$\det(F)$	determinant of F, [–]
E	material elasticity, [Pa]
E_f	material elasticity following plastic deformation, [Pa]
E_L	linear material elasticity, [Pa]
E_p	laser microbeam pulse energy, [kg $\cdot$ m^{2} $\cdot$ s^{-2}]
E_R	material elasticity during recovery, [Pa]
f	focal length, [m]
F	deformation gradient tensor, [–]
H	enthalpy difference between liquid pressure at the bubble wall and infinity, [m^{2} $\cdot$ s^{-2}]
I	identity matrix, [–]
J	shear stress impulse, [Pa $\cdot$ s]
k	number of photons necessary for photoionization, [–]
$\max(x)$	maximum value of array variable x, [–]
n	Tait equation parameter, [–]

p	fluid pressure, [Pa]
p_B	pressure within the bubble, [Pa]
p_v	vapor pressure, [Pa]
p_∞	fluid pressure at an infinite distance from the bubble or hydrostatic pressure, [Pa]
P	pressure at the bubble wall, [Pa]
r	radial position or material points in the deformed state, [m]
r_o	material coordinates in the initial unstrained configuration, [m]
R_B	bubble wall radius, [m]
$\dot{R}_B$	bubble wall velocity, [$\mathrm{m} \cdot \mathrm{s}^{-1}$]
$\ddot{R}_B$	bubble wall acceleration, [$\mathrm{m} \cdot \mathrm{s}^{-2}$]
R_f	bubble wall radius at which the material ruptures, [m]
R_{max}	maximum bubble wall radius, [m]
R_n	equilibrium or initial bubble wall radius, [m]
R_o	bubble wall radius in equilibrium or initial configuration, [m]
S	surface tension, [$\mathrm{N} \cdot \mathrm{m}^{-1}$]
t	time, [s]
T	transpose, [–]
T_B	bubble oscillation duration, [s]
u	material point displacement, [m]
V_B	bubble wall velocity, [$\mathrm{m} \cdot \mathrm{s}^{-1}$]
V_∞	fluid velocity beyond the bubble wall, [$\mathrm{m} \cdot \mathrm{s}^{-1}$]

Greek

ΔE	band gap energy, [eV]
ε	Almansi strain tensor, [–]
ε_{bw}	bubble wall strain, [–]
ε_f	material rupture strain, [–]
ε_{max}	strain at maximum bubble wall radius, [–]
η	elastic modulus, [Pa]
κ	polytropic constant, [–]
λ	laser wavelength, [m]
μ_l	liquid viscosity, [kg · m^{-1} · s^{-1}]
ν_l	kinematic viscosity, [m^2 · s^{-1}]
π	3.14159…, [–]
ρ	liquid density, [kg · m^{-3}]
ρ_B	liquid density evaluated at the bubble wall, [kg · m^{-3}]
ρ_{cr}	critical free electron density, [m^{-3}]
ρ_∞	liquid density at infinity or far from the bubble, [kg · m^{-3}]
τ_w	wall shear stress, [Pa]
χ^2	least squares error, [–]

ACKNOWLEDGMENTS

I express sincere gratitude to my advisors, Prof. Vasan Venugopalan and Prof. Elliot Botvinick, for their scholarly tutelage. Thank you for the opportunity to conduct research in your labs and providing me with rigorous scientific training. Your commitment and dedication in guiding me is deeply appreciated.

Thank you Prof. Michelle Digman, Prof. Jennifer Prescher, Prof. Weian Zhao, and Prof. Ali Mohraz for your gracious guidance as well as supporting my research.

A cordial thanks to Dr. Mark Keating, Dr. Abhishek Kurup, Dr. Bhupinder Shergill, Dr. Shreyas Ravindranath, Tim Tran, Max Kaganyuk, Todd Thorson, and Herman Ching. I am grateful for your friendship, support, and willingness to always discuss research with me.

Thank you kindly to Dr. Jonathan Compton, Dr. Huan Ma, Dr. Adam Gardner, Dr. Carole Hayakawa, Dr. Janaka Ranasinghesagara, and Dr. Rolf Saager. Your mentorship in experimentation and writing software is greatly appreciated.

My sincere gratitude to Royce Liang, Andy Shaw, and Albert Chang for their support. Your friendship is truly appreciated.

I express loving appreciation for my mother, father, and brother. Thank you for the encouragement and always believing in me. I cherish and love you.

CURRICULUM VITAE

Justin C. Luo

Education

University of California, Irvine

Graduate
Ph.D., Biomedical Engineering 2018
M.S., Biomedical Engineering 2015

Undergraduate
B.S., Biomedical Engineering; Chemistry; Biology 2011

Appointments

Graduate Student Researcher 2012-2018
Department of Biomedical Engineering; University of California, Irvine
Advisors: Prof. Elliot L. Botvinick and Prof. Vasan Venugopalan

Teaching Experience

Teaching Assistant
Department of Biomedical Engineering; University of California, Irvine
BME 150 – Biotransport Phenomena: Spring 2015

Honors and Awards

NSF Integrative Graduate Education and Research Traineeship

Publications

2. **Luo, J.C.**, Botvinick, E.L., and Venugopalan, V. Reply to 'Mechanism for microtsunami-induced intercellular mechanosignalling'**.** *Nature Photonics*. **9**, 624-625 (2015).

1. Compton, J.L., **Luo, J.C.**, Ma, H., Botvinick, E., and Venugopalan, V. High-throughput optical screening of cellular mechanotransduction. *Nature Photonics*. **8**, 710-715 (2014).

Conference Presentations

3. **Luo, J.C.**, Compton, J.L., Ma, H., Botvinick, E.L., and Venugopalan, V. µTsunamis: An optical platform for high-throughput screening of cellular mechanotransduction. *NIH NHLBI Innovation Conference – West*, Irvine, CA, Poster, November 2015.

2. **Luo, J.C.**, Compton, J.L., Ma, H., Botvinick, E.L., and Venugopalan, V. µTsunamis: An optical platform for high-throughput screening of cellular mechanotransduction. *2015 BMES Annual Meeting*, Tampa, FL, Poster, October 2015.

1. **Luo, J.C.**, Compton, J.L., Ma, H., Botvinick, E., and Venugopalan, V. µTsunamis: A method for high-throughput screening of cellular mechanotransduction using laser-generated cavitation bubbles. *SPIE: Optical Trapping and Optical Micromanipulation XI*, San Diego, CA, Podium, August 2014.

ABSTRACT OF THE DISSERTATION

Optomechanotransduction and Optorheology

By

Justin C. Luo

Doctor of Philosophy in Biomedical Engineering

University of California, Irvine, 2018

Professor Vasan Venugopalan, Chair

Professor Elliot L. Botvinick, Co-Chair

Cellular mechanotransduction refers to the process of converting external mechanical stimuli into internal biochemical signals. This conversion mediates many cellular functions where defects in mechanotransduction can lead to the initiation and progression of disease. Given its importance, a technology capable for activating mechanosignalling via application of mechanical stimuli to investigate and screen mechanotransduction in either two-dimensional (2D) or three-dimensional (3D) context can provide a powerful tool for basic cellular studies as well as identifying potential/repurposing current therapeutic compounds.

Here, we present the development of a high-throughput optical technology known as the µTsunami platform that utilizes a pulsed laser microbeam to mechanically perturb cells by microcavitation bubble (µCB) generated impulsive fluid shear stresses and standard fluorescence microscopy for evaluating the resultant cellular mechanosignalling. We establish the capability of µTsunami induced shear stress impulses to activate cellular mechanotransduction. This was confirmed via µTsunami exposure of primary adherent human umbilical vein endothelial cells (HUVECs) plated on fibronectin coated glass-bottomed dishes which led to initiation of Ca^{2+} signalling. Moreover, we demonstrate the capacity of our platform to accurately measure suppression of Ca^{2+} mechanosignalling in a dose-dependent fashion when putative inhibitors were administered and completed a mock high-throughput screening (HTS) experiment.

We hypothesize µTsunamis initiate Ca^{2+} mechanosignalling by mechanical stimulation of stretch-sensitive G Protein-Coupled Receptors (ssGPCRs) which activate the IP_3 pathway. Ca^{2+} signalling due to diffusible factors released by cells proximal to the µTsunami which turn on purinergic receptors remains an alternative postulate. To differentiate between these two hypotheses, we conducted studies to investigate the effect of chemical inhibitors of key molecular proteins along the IP_3 pathway and purinoceptors on µTsunami-initiated mechanosignalling. Our results demonstrate that µTsunami-induced Ca^{2+} signalling in HUVECs was activated mechanically and does not arise via the chemical activation of purinergic receptors. Moreover, we determined the spatial extent of Ca^{2+} signalling is dependent on the magnitude of shear stress impulse that the cells are exposed to independent of laser microbeam pulse energy. This establishes a clear mechanical dose-response relationship for µTsunami activated mechanosignalling.

Lastly, we introduce a non-invasive technique to measure the viscoelastic properties of soft matter at high strain-rates known as Laser-Induced Cavitation Rheology (LICR). LICR utilizes experimental measurement of cavitation dynamics within hydrogels, theoretical prediction of bubble dynamics using a viscoelastic model that accounts for potential material failure, and retrieval of material properties using non-linear least squares optimization. For biologically and synthetically derived hydrogels, we demonstrated LICR not only is capable of quantifying the maximum cavitation radius R_{max} and elastic moduli η as well as the strain at which the viscoelastic material fails ε_f . Furthermore, we presented preliminary evidence of mechanically activating Ca^{2+} signalling in HUVECs embedded within fibrin gels which demonstrates the ability of our technique to apply physical stimuli in a 3D context.

Collectively, these results effectively establishes our technologies in providing mechanical perturbation in both 2D and 3D context for the investigation and screening of cellular mechanotransduction. This platform presents unique opportunities for the investigation of mechanosignalling pathways and characterization of materials at high strain-rates.

Chapter 1

Introduction

1.1 Background and Motivation

This chapter introduces the central themes of this dissertation. We discuss the rationale behind developing and characterizing an optical platform that provides impulsive mechanical stimulations and measures the resulting biochemical response in cells cultured within either the 2D or 3D context while also having the capability to measure the elastic properties of soft matter in 3D. The application of our platform for HTS and investigation of cellular mechanotransduction in which mechanical perturbation produced by pulsed laser radiation influences the activity of cellular signaling pathways represents the optomechanotransduction aspect of this research. Utilization of our platform to determine the mechanical properties of soft biological and synthetic viscoelastic materials represents the optorheological aspect. The interested reader is directed to the bibliography for a more comprehensive overview concerning the topics of mechanotransduction[1], drug screening[2], and context of cell dimensionality[3].

Mechanotransduction refers to the process whereby cells sense external mechanical inputs and convert these cues into internal biochemical signals[4]. Fig. 1-1 depicts multiple cellular components capable of receiving physical stimuli either via neighboring cells or their surrounding microenvironment; including from the extracellular matrix (ECM) or external fluid flow. Force-sensitive receptors adorning the surface of the plasma cell membrane serve as the primary upstream molecular mediators that initiate mechanosignalling as portrayed in Fig. 1-2. When deformed, these mechanosensors are hypothesized to undergo a conformational change into their active state upon activation[5]. This leads to the activation of biochemical cascades further downstream, triggered by the release of second messengers or other biomacromolecules, which regulate gene expression governing cellular responses such as proliferation, differentiation, and migration[6-8]. Several hallmark examples of cellular systems capable of mechanotransduction include: inner hair cells involved in audition[9], endothelial cells in blood pressure regulation[10], and osteoblasts in plating bone[11]. Moreover, the inception, progression, or exacerbation of a wide spectrum diseases originate from defective mechanosignalling[12-14]. Unsurprisingly, these include hearing loss[15], cardiovascular disease[16], cancer[17], and osteoporosis[18,19]. This attests not only to the importance of mechanical forces in biology, but also highlights the significance in a mechanistic approach towards the development of new methodologies for investigating mechanotransduction and drug discovery/development with the aim of modifying the activity of dysfunctional mechanosignalling pathways. Studying the basic mechanisms of mechanotransduction would provide insight into targeting specific pathways for designing treatment strategies. Indicated as such, we require platforms capable of activating mechanosignalling pathways in cells via application of mechanical perturbation to investigate cellular mechanotransduction.

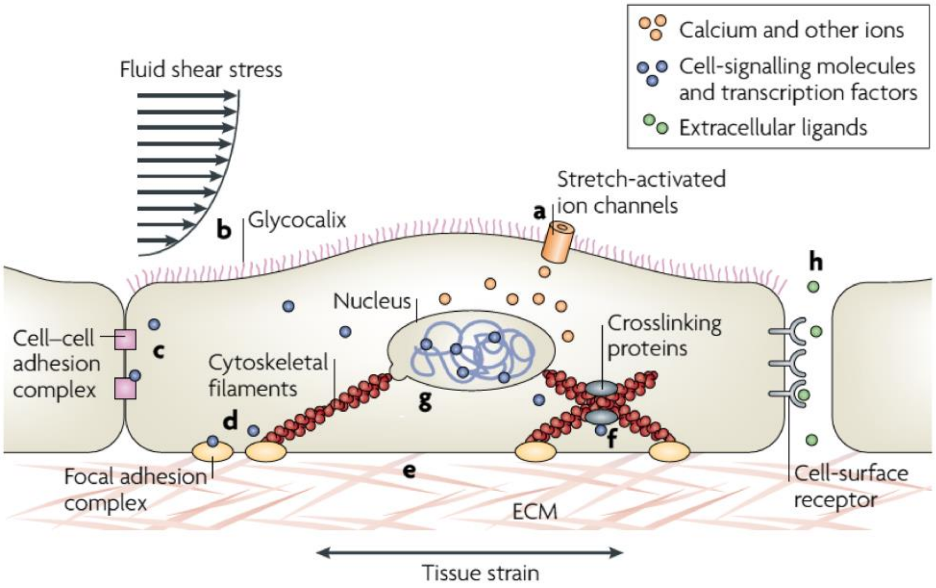

Fig. 1-1 | Cellular mechanotransduction activated by multiple modes of mechanical perturbation. Adapted from [12].

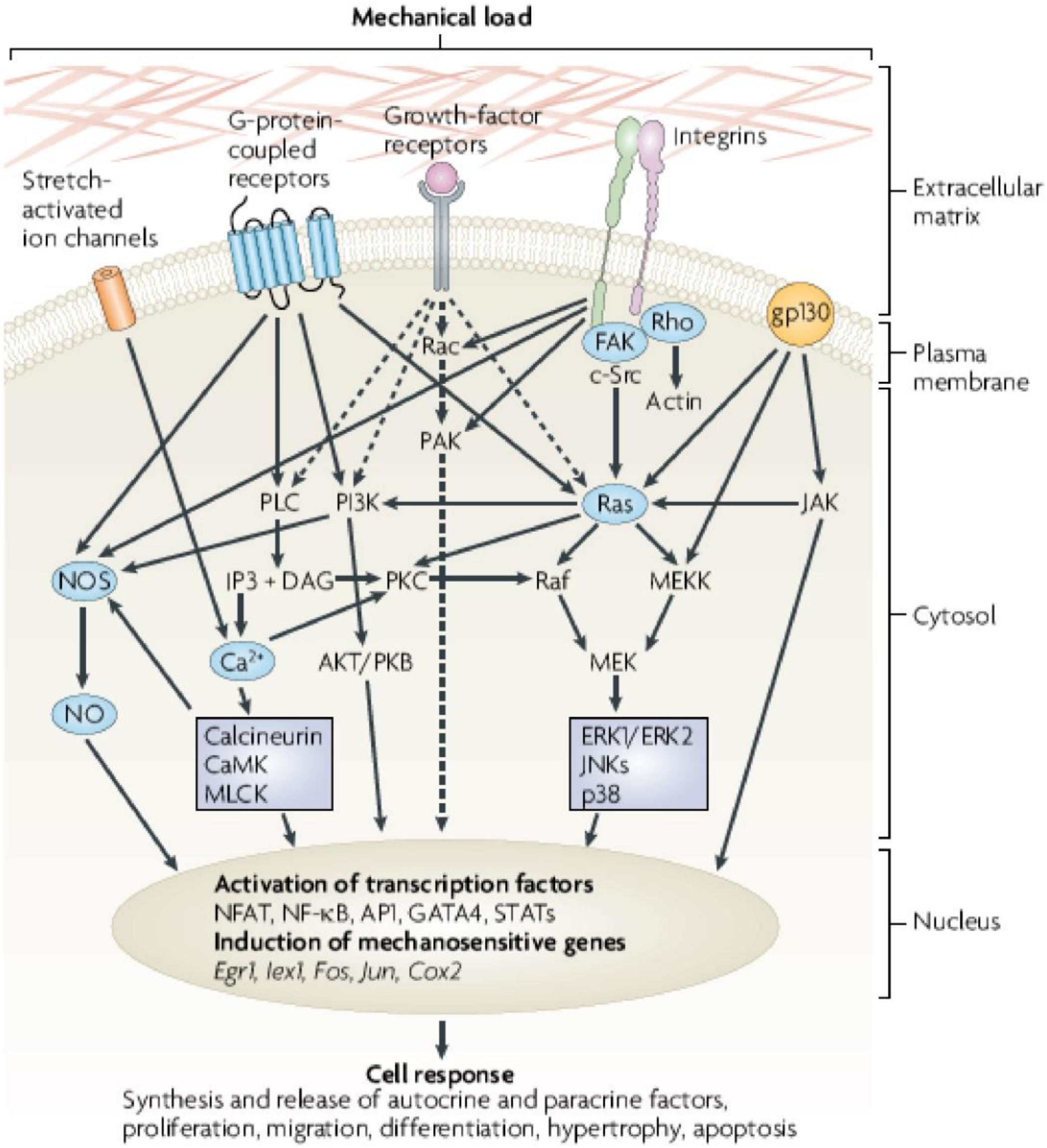

Fig. 1-2 | Mechanosignalling pathways activated by force-sensitive cell surface receptors. Adapted from [12].

The development of an optical platform that can rapidly assess cellular mechanotransduction activity has the potential to positively impact the process of drug discovery. Drug discovery and development is a costly process that consists of multiple complex phases to identify new medicine capable of treating diseases of interest[20]. Identification/validation of a 'druggable' target, defining 'hits', selection/optimization of a lead compound, and pre-clinical are stages that constitute the discovery portion of the process. The drug development portion of the process covers phases I-III of clinical trials and regulatory approval submission for market launch[21]. The timespan for launching a new therapeutic to the market, relative to initiation of the drug discovery program, typically requires at least a decade which demonstrates the need to streamline this process[22]. Our focus is on hit discovery via screening to determine potential chemical compounds effective in modifying cellular processes linked to pathologies endemic to dysfunctional mechanotransduction. Conventionally, the screening process typically involves assessing small molecule libraries by administering potential drug chemicals into 2D in vitro biochemical assays and evaluating their efficacy in modulating biological activity conveyed as a measurable readout. The chemical compounds capable of interfering with disease associated signalling pathways are deemed as ‘hits’ and considered for further evaluation. With the availability of numerous potential drug compounds from chemical libraries, high-throughput methodologies are adopted in attempt to hasten the screening process through automation and attrition of ineffective small molecules. However, methods that pertain to conventional screening are unable to rapidly discern compounds that are effective in modifying the activity of dysfunctional mechanotransduction pathways. Screening from a mechanobiological standpoint would require the delivery of mechanical stimulation to cells cultured in a 2D/3D context to either elicit or suppress mechanotransduction following administration of potential therapeutics and quantifying the efficacy of these compounds in modifying mechanosignalling.

While awareness is increasing regarding the significance of mechanobiology in the drug development and discovery, it has yet to be clearly addressed[23,24]. This potentially translates to a lack of available technologies for HTS of cellular mechanotransduction which likely limits the ability of pharmaceutical companies to identify new approaches to target mechanosignalling pathways. Moreover, the pharmaceutical industry is releasing fewer new molecular entities due to decrease in R&D productivity[25]. A HTS platform with the ability to discover hits and repurpose current drugs on the market would potentially enable big pharma to increase productivity by targeting mechanotransduction.

Much of our current comprehension of mechanotransduction and mechanobiology is based on studies where cells were cultured in 2D configurations. In 2D cultures, cells *in vitro* are typically plated on either plastic or glass surfaces coated with proteins for attachment including fibronectin and vitronectin which interact with integrins[26]. However, cell cultivation on flat substrates is not a faithful representation of the physiological context. Cells *in vivo* reside within a 3D microenvironment known as the ECM. The ECM is a fibrous mesh of biological soft matter, synthesized and assembled by the resident cells themselves[27]. Embedded in this niche microenvironment, cells adhere to their fibrillar surroundings which serve as a structural scaffold that provides biochemical as well as mechanical cues and diffusion limited medium for accessing sustenance[28]. Encapsulated cells sense stiffness of their surroundings via integrins directly linked to the ECM as illustrated in Fig. 1-3. This connection enables transducing external physical stimuli internally through adhesion complexes, recruited following integrin activation, tethered to the cytoskeletal network which is capable of influencing gene expression and cell response[29]. The findings of numerous studies have established the importance of matrix stiffness in commanding cellular processes and decisions, notably cell fate[30,31]. This indicates the influence that the ECM exerts on cell behavior, function, and phenotype. Conversely, cells retain the ability to migrate and actively remodel the ECM which demonstrates the dynamic reciprocity of this bi-directional interaction[32]. The value of 2D cell cultivation is limited since their native biological form and function cannot be fully recapitulated. A specific example of this is demonstrated by mammary epithelial cells (MECs) which are commonly employed to investigate the fundamental mechanisms of morphogenesis, oncogenesis, and carcinogenesis in breast cancers[33]. MECs cultured in the 3D context reconstitute into their respective *in vivo* morphologies and express physiological markers as indicated by formation of a hollow spheroid structure as well as secretion of milk proteins[34]. The physiological limitations of 2D cell culture has shifted efforts towards investigating and screening cellular mechanotransduction in the context of 3D systems[35]. In 3D culture systems, cells are typically enclosed in viscoelastic hydrogels fabricated from ECM-derived materials for mimicking the endemic cellular microenvironment *in vivo*[36]. This further reinforces a need for technologies with the capability to not only mechanically stimulate cells in 2D culture configurations, but also deliver physical perturbation within the 3D context and characterize the viscoelastic properties of the local cellular microenvironment. Such a methodology would provide the means to interpret the effects of applied stresses and ECM stiffness in dictating cellular response.

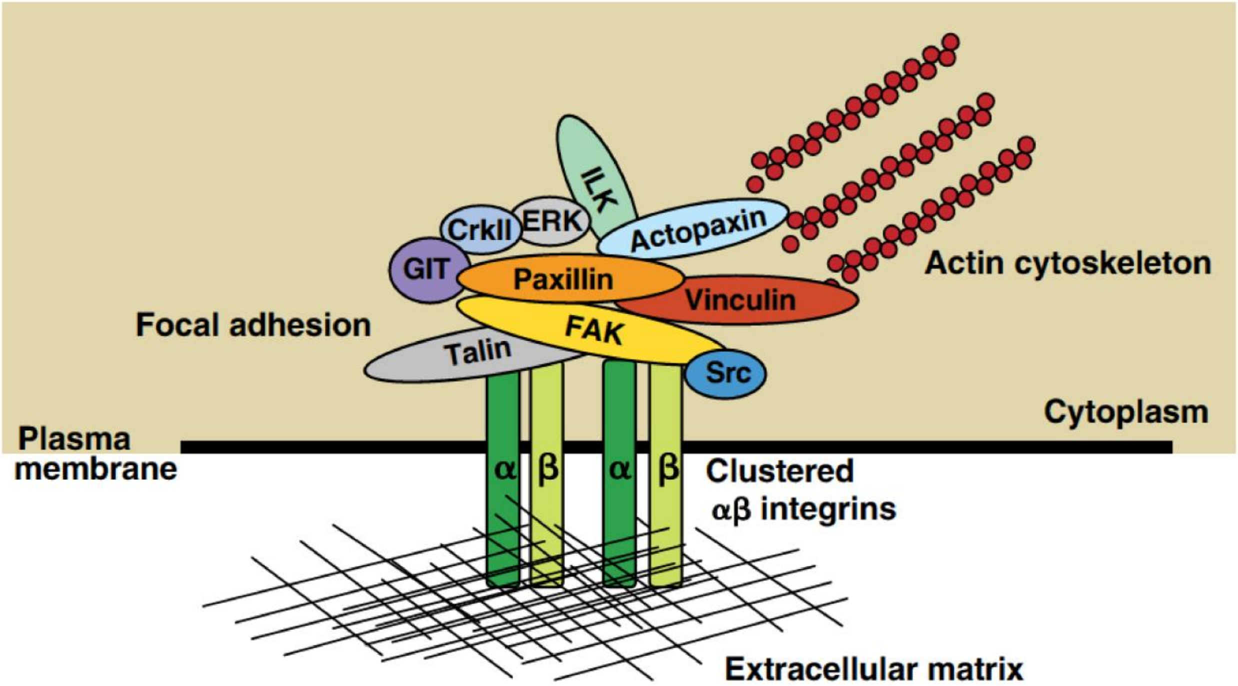

Fig. 1-3 | Structural and signalling connection enabling transmittance of mechanical cues from the ECM into internal biochemical cascades. Adapted from [29].

1.2 Research Objectives

The focus of this dissertation is developing a platform capable of providing mechanical perturbation for conducting high-throughput screening and investigating the basic mechanisms of mechanotransduction in either 2D or 3D context since mechanical forces are implicated in governing critical cellular functions. Given this goal, the remaining chapters of this thesis are structured as follows. Chapter 2 introduces the development of an optical platform for high-throughput screening of cellular mechanotransduction that combines pulsed laser microbeam and optical imaging based technologies. In Chapter 3, we characterize the underlying molecular and stimulation mechanism in which our platform activates cellular mechanotransduction. Chapter 4 establishes a method to quantify the elastic moduli and mechanically stimulate cellular mechanotransduction in 3D scaffolds. Lastly, Chapter 5 summarizes this dissertation with concluding remarks and provides the framework for future directions while suggesting further research.

Chapter 2

Optical High-Throughput Investigation and Screening of µTsunami Initiated Cellular Mechanotransduction

2.1 Introduction

The previous chapter introduced cellular mechanotransduction and conventional drug screening process. We discussed the rationale for a mechanistic approach towards the screening of molecules to identify those capable of modulating mechanosignalling pathways. This chapter presents an optical platform for high-throughput screening and investigation of cellular mechanotransduction. We further demonstrate the use of this platform to conduct high-throughput drug screening[37].

Screening cellular mechanotransduction is contingent on the activation of mechanosignalling pathways in cells via mechanical perturbation. While conventional drug screening methodologies are capable of rapid and precise assessment of exogenously administered potential drugs to chemically modify the activity of dysfunctional signalling pathways using technologies such as imaging cytometers[38], they lack the means to provide mechanical forces and cannot physically stimulate cells in a high-throughput manner. Several established methods for applying mechanical forces include atomic force microscopy[39], optical[40] or magnetic[41] traps, substrate stretching apparatus[42], and laminar flow chambers[43]. However, these techniques are not only unable to provide mechanical stimulation at high-throughput but also their integration into existing drug screening or imaging systems is non-trivial due to specialized and non-standardized instrumentation requirements. These limitations prevent the discovery of mechano-active therapeutics which we postulate is a class of drugs with the potential to target and modulate mechanosignalling pathways. Therefore, we developed and characterized a high-throughput platform capable of providing rapid physical stimulation for screening mechano-active drugs to treat diseases due to malfunctioning mechanotransduction.

2.2 Background and Approach

Platform Design

In designing a high-throughput drug screening platform, we opted for an optical approach that consists of laser and imaging-based technologies. The platform combines a (1) pulsed laser for initiating a single microcavitation bubble (µCB) that provides mechanical stimulation to individual or cell populations and (2) standard fluorescence microscopy which is essentially an imaging cytometer for dynamic evaluation of signalling activity. The µCB is created from focusing single pulsed laser microbeam at 10 µm above a confluent cell monolayer. µCB expansion as well as collapse displaces the surrounding aqueous culture media and instantaneously exposes adherent cells to a microtsunami (µTsunami) which exposes cells in a 2D culture to transient impulsive hydrodynamic shear stresses at the micro-scale level. µTsunamis can be delivered to precise locations or specific times to cells while imparting impulsive fluid shear with high controllability in the duration, magnitude, and spatial coverage of exposure[44]. In a previous study, we exposed adherent cells to µTsunami generated shear stresses and mapped distinct zones of cellular outcomes. Relative to the position where µTsunamis were initiated with increasing radial distance, we reported regions with cells that are: (1) lytic, (2) necrotic, (3) optically perforated for molecular delivery, and (4) still viable[45]. We demonstrate here the ability to activate mechanotransduction in adherent cells beyond the zone of optoinjection with µTsunamis. This combination which includes providing cells with tunable mechanical perturbation and real-time imaging enables assaying potential drug compounds and their effects on cellular mechanosignalling elicited by external physical inputs.

Optical Breakdown Physics

The creation of µCBs to stimulate cellular mechanotransduction involves nonlinear absorption of pulsed laser irradiation in a transparent aqueous medium. Cavitation is a consequence of optical breakdown that occurs within the laser microbeam focal volume. Plasma is formed from optical breakdown and evaporates the surrounding liquid environment which creates a vapor cavity or bubble. Inducing optical breakdown or plasma formation requires exceeding a critical density threshold of quasi-free electrons during the laser pulse duration. This threshold of critical free electron density is achieved through the coaction between multiphoton and avalanche or cascade ionization processes as depicted in Fig. 2-1. In order to become quasi-free, overcoming a band gap energy of ΔE = 6.5 eV is necessary for the promotion of a bound electron into the conduction band. The energy for photoionization was calculated by assuming pure liquid water as an amorphous dielectric material[46].

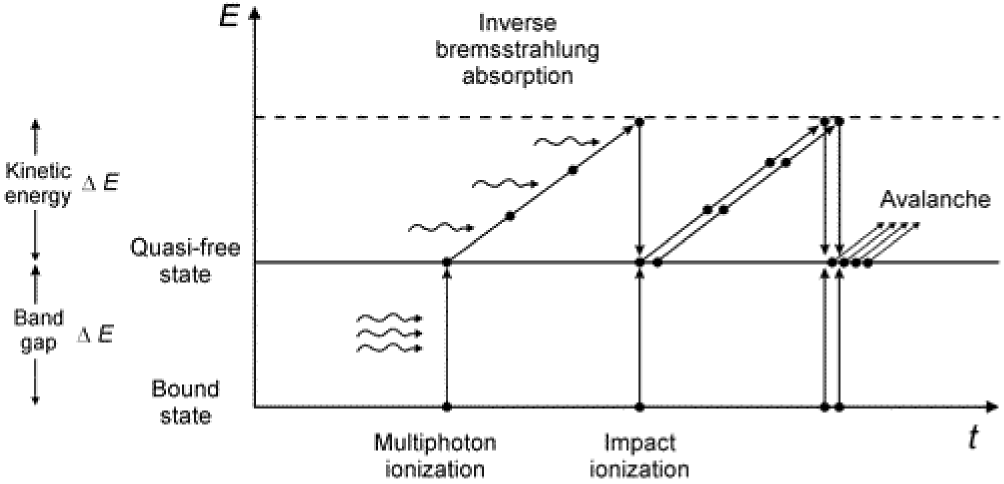

Fig. 2-1 | Avalanche ionization which involves the interplay between multiphoton ionization, inverse Bremsstrahlung absorption, and impact ionization in plasma formation. Adapted from [49].

Multiphoton absorption in water molecules supplies an initial seed of one or more free electrons. These seed electrons absorb photons through inverse Bremsstrahlung absorption (IBA) to increase their kinetic energy[47]. Another free electron is produced by impact ionization which occurs following k, the number of photons required for photoionization, IBA events when the accrued kinetic energy of the initial electron exceeds ΔE[48]. Impact ionization essentially doubles the number of free electrons, except with low kinetic energy. Free electrons with low kinetic energy can reenergize by absorbing photons again through IBA. The reiterative nature of this process enables exponential increase in the number of free electrons to achieve the required critical density for plasma formation. Together, the series of events involving IBA and impact ionization describes avalanche or cascade ionization.

In the µTsunami platform, we employ a λ = 532 nm laser that pulses for a duration of 500 ps to create µCBs. With picosecond lasers, exceeding a critical free electron density threshold of ρ_{cr} = 10^{21} cm^{-3} is required for optical breakdown in water[49]. Moreover, a single photon at 532 nm contains 2.34 eV and three photons are essential to surpass the ΔE barrier to photoionize. We elected to utilize a pulsed laser of visible wavelength due to several reasons: (1) delivery of high-throughput mechanical perturbation to cells without requiring physical contact, (2) relative ease of incorporation into standard imaging systems as well as alignment, and (3) minimal absorption of visible wavelengths in aqueous environments which is evidenced in Fig. 2-2. Laser-induced optical breakdown is well characterized and employed in many biomedical applications including intracellular ablation[50], intraocular surgery[51], and laser lithotripsy[52].

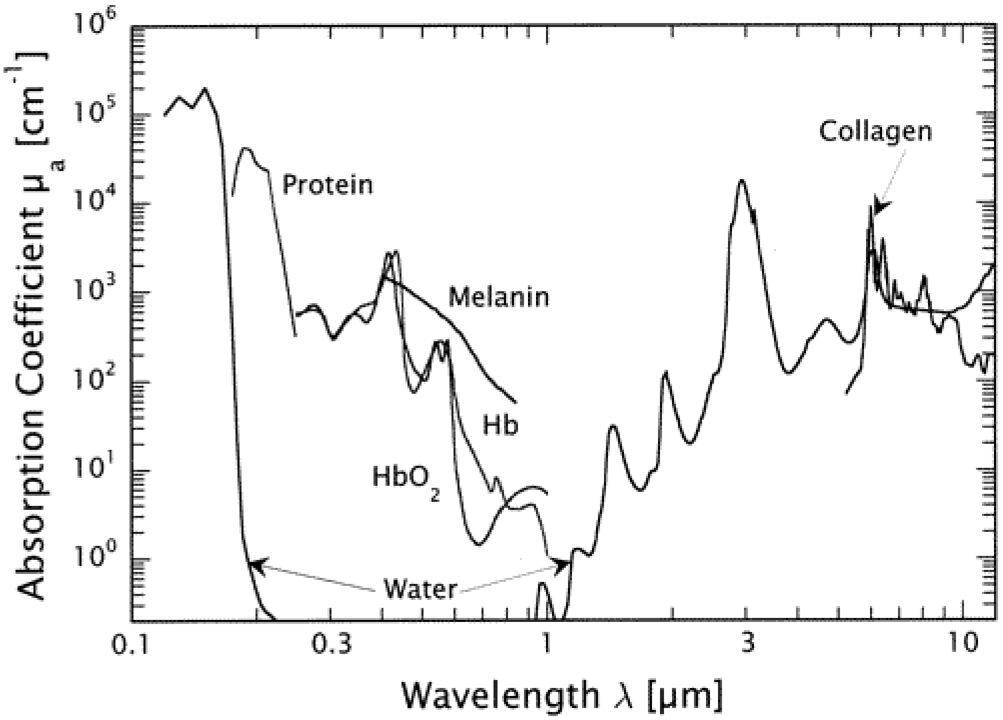

Fig. 2-2 | Optical absorption coefficients of water and principal tissue chromophores within the spectral range of 0.1-12 µm. Adapted from [49].

Shear Stress Impulse Modelling and Computation

Quantifying the shear stress impulse field is essential for correlating cellular exposure of µTsunamis with the observed signalling response. This requires predicting µCB dynamics and utilizing these quantities in hydrodynamic models to determine the distribution of wall shear stress generated by the µTsunami. We employed the Gilmore equation to obtain quantitative predictions of the time-varying bubble wall radius and velocity, $R_B(t)$ and $V_B(t)$, respectively[53,54]. This model accounts for effects of surface tension, viscosity, and compressibility of the liquid medium on bubble dynamics. In spherical coordinates, the assumptions include irrotational flow and constant vapor content within the cavity while neglecting heat as well as mass transfer across the bubble wall. The Gilmore model that describes bubble dynamics is given by:

$$\ddot{R}_B = \left[-\frac{3}{2}\left(1-\frac{\dot{R}_B}{3C}\right)\dot{R}_B^2 + \left(1+\frac{\dot{R}_B}{C}\right)H + \frac{\dot{R}_B}{C}\left(1-\frac{\dot{R}_B}{C}\right)R_B\frac{dH}{dR_B}\right]\left[R_B\left(1-\frac{\dot{R}_B}{C}\right)\right]^{-1}$$

where R_B represents the bubble wall radius, $\dot{R}_B$ being the bubble wall velocity, $\ddot{R}_B$ signifies the bubble wall acceleration, C denotes sonic velocity at the bubble wall, and H the enthalpy difference between liquid pressure at the bubble wall and far away from the bubble or hydrostatic pressure[55]. Pressure in the fluid at the bubble wall is defined as:

$$P = \left(p_\infty + \frac{2S}{R_n}\right)\left(\frac{R_n}{R_B}\right)^{3\kappa} - \frac{2S}{R_B} - \frac{4\mu_l}{R_B}\dot{R}_B$$

where p_∞ = 101325 Pa signifies fluid pressure at an infinite distance from the bubble or static pressure, S = 0.072 N · m^{-1} denotes surface tension, μ_l = 0.894 x 10^{-3} kg·m^{-1}·s^{-1} symbolizes liquid viscosity, κ = 4/3 is a polytropic constant, and R_n is the equilibrium bubble radius. The equilibrium or initial bubble radius is formulated as:

$$R_n = \sqrt[3]{\frac{{R_{max}}^3 p_v}{p_\infty}}$$

where R_{max} is the maximum bubble wall radius and p_v = 3169 Pa as the vapor pressure within the bubble. C and H were derived from the Tait equation of state for liquids. The Tait equation is defined by:

$$\frac{P + B}{p_\infty + B} = \left(\frac{\rho}{\rho_\infty}\right)^n$$

where ρ is liquid density, ρ_∞ = 997 kg·m^{-3} designates the liquid density at infinity, and B = 314 MPa as well as n = 7 are constants. C is described by the following expression:

$$c^2 = \frac{dp}{d\rho} \rightarrow C = \sqrt{c_\infty^2 + (n-1)H}$$

with c symbolizing the speed of sound, p corresponds to fluid pressure, and c_∞ = 1483 m·s^{-1} being the sound velocity in liquid far from the bubble at infinity. H is expressed by:

$$H = \int_{p_\infty}^{P} \frac{dp}{\rho} \rightarrow H = \frac{n(p_\infty + B)}{(n-1)\rho_\infty}\left[\left(\frac{P+B}{p_\infty + B}\right)^{\frac{n-1}{n}} - 1\right]$$

All listed parameter values are for water at 25°C.

The Gilmore model has been extensively applied to model cavitation bubble dynamics, even for pulsed laser generated µCBs where we confirmed the predictions to be accurate with time-resolved imaging[56]. With $R_B(t)$ as well as $V_B(t)$ predicted numerically, we consider the model problem portrayed in Fig. 2-3 for hydrodynamic modelling and formulate expressions to compute impulsive shear stresses imparted by µCB dynamics in the fluid[57].

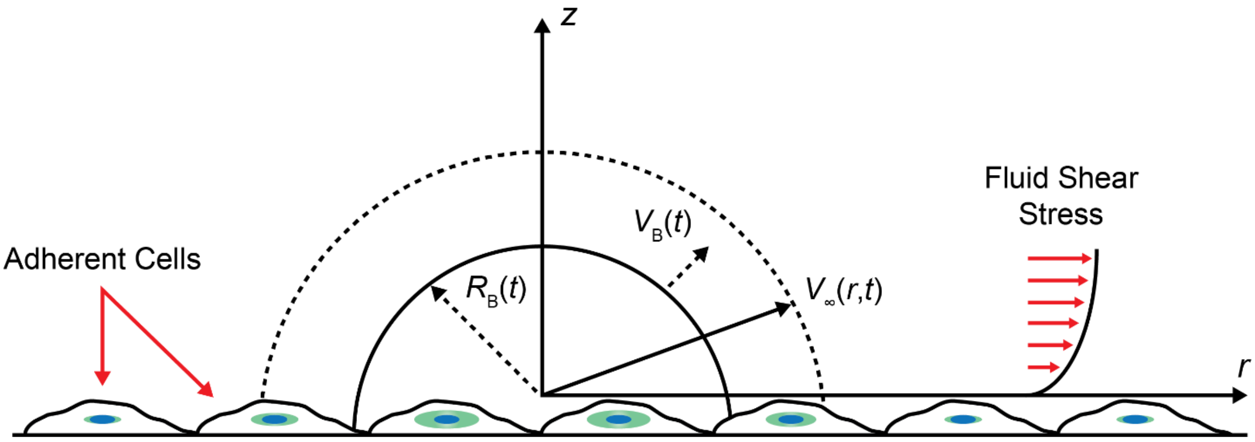

Fig. 2-3 | Model problem schematic considered for hydrodynamic modelling of µTsunami shear stress impulses applied over a monolayer of cells. $R_B(t)$ and $V_B(t)$ represents the time-varying bubble wall radius and velocity theoretically predicted by the Gilmore equation, respectively. The fluid velocity for radial positions beyond the µCB wall is denoted by $V_\infty(r,t)$. Adapted from [37].

Our model assumes the adherent HUVEC monolayer serves as a fixed boundary that is exposed to shear forces via impulsive parallel fluid displacement from the expanding µCB. By invoking mass conservation, we obtain fluid velocities at any radial location beyond the µCB wall which is given as:

$$V_\infty(r,t) = \frac{\rho_B(t){R_B}^2 V_B - \int_{R_B(t)}^{r} \frac{\partial \rho(r,t)}{\partial t} r^2 dr}{r^2 \rho_\infty}$$

where ρ_B is the density evaluated at the bubble wall determined from the Tait equation of state for water.

Application of momentum conservation by using the solution to Stokes' first problem and Duhamel's superposition integral with $V_\infty(r,t)$ provides the following equation for the wall shear stress, spatially and temporally, generated by µCB expansion:

$$\tau_w(r,t) = \rho_\infty \sqrt{\frac{\nu_l}{\pi}} \int_0^t \frac{\partial V_\infty(r,t)}{\partial t'} \frac{dt'}{\sqrt{t-t'}}$$

where $\nu_l = \mu_l \cdot \rho_\infty^{-1}$ describes the kinematic viscosity of the fluid medium. The total shear stress impulse at any radial location relative to the µCB origin is derived by integration which is expressed as:

$$J(r) = \int_0^{T_B} \tau_w(r,t)dt$$

where T_B corresponds to the oscillation duration or time of a single µCB cycle.

µTsunami Stimulated Intracellular Ca^{2+} Mechanosignalling

We hypothesized that µTsunamis are capable of stimulating cellular mechanotransduction. In order to confirm this assertion, our platform was tested for its ability to mechanically activate and fluorescently monitor intracellular calcium signalling within primary human umbilical vein endothelial cells (HUVECs). Endothelial cells are a classic model for mechanotransduction of prominence in the vascular system[58]. This cell type lines the blood vessel lumen and is constantly exposed to impulsive shear from pulsatile blood flow pumped by the heart[59]. Due to having the disposition of being exquisitely sensitive to flow, exposing HUVECs to impulsive shear stresses generated from µTsunamis is an appropriate context of physiological relevance for evaluating our platform capabilities. The perturbation of endothelial cells mechanically is established to result in Ca^{2+} signalling[60]. Calcium is a prevalent and crucial ion, typically as a second messenger, that influences cytosolic signalling pathways[61]. For instance, intracellular Ca^{2+} signalling regulates downstream endothelial cell processes including the production/release of nitric oxide and prostacyclin which have vasodilatory effects[62,63]. The ions for calcium signalling in endothelial cells are derived from either internal or external sources. Intracellularly, Ca^{2+} ions are stored within the endoplasmic reticulum (ER) and mitochondria organelles[64]. The extracellular cationic influx through specifically gated ion channels poses an alternative for endothelial cells to increase their cytosolic Ca^{2+} levels. We postulated µTsunami generated shear stress impulses activate the IP_3 pathway by mechanical stimulation of G Protein-Coupled Receptors (GPCRs), either directly or indirectly, where Ca^{2+} is internally released from the ER and results in the cytosolic signalling cascade[65].

With our platform, we investigated whether µTsunamis are able to initiate intracellular Ca^{2+} signalling in HUVECs. In these studies, HUVECs were cultured in fibronectin coated glass-bottomed petri dishes and labelled with Fluo-3/AM which is a fluorescent dye that increases emission when bound to cytosolic Ca^{2+} for indication of signalling. During the experiment, HUVECs were kept on calcium-free buffer to remove calcium ions from their external environment. The buffer was also supplemented with EGTA to chelate traces of Ca^{2+} possibly still present in the media, if any. These steps were taken to ensure the observed Ca^{2+} signalling response originated intracellularly as opposed to extracellularly from transport across ion channels on the cell surface. To establish that our platform is capable of identifying potential drugs such as putative inhibitors that act on mechhanosignalling pathways, we administered 2-aminethoxydiphenyl borate (2-APB) for suppressing Ca^{2+} signalling. Moreover, we conducted a mock screening experiment in a standard 96 well-plate to determine the applicability of our automated platform in an actual setting for HTS of cellular mechanotransduction.

2.3 Materials and Methods

Shear Stress Impulse Computation

We implemented the Gilmore equation and our hydrodynamic model by writing a script in MATLAB for numerically computing the cellular exposure to shear stress impulse at any radial position from the µCB center. Refer to Appendix A for the actual code.

µTsunami Platform

Fig. 2-4 illustrates our laser microscope setup for initiating µTsunamis. µCBs were generated by 500 ps duration pulses at λ = 532 nm emitted from a Q-switched pulsed microchip laser (PNG-M03012, Teem Photonics). We utilized a diverging lens as well as a converging optic with focal length *f* of -25 mm and 500 mm to expand and collimate the laser microbeam, respectively. Pulse energy was controlled via λ/2 wave-plate and polarizing beamsplitter. An iris cropped the outer laser beam edge for allowing only the central portion to enter the right port of an inverted microscope (IX-81, Olympus). The laser pulse was directed by a dichroic mirror (ZT532NBDC, Chroma) to the rear aperture of a 20x 0.45 NA objective (LUCPlanFLN, Olympus) which focused the beam 10 µm above the HUVEC monolayer. This offset was introduced by slightly defocusing the laser microbeam collimation which enabled delivery of µTsunamis 10 µm above the imaging plane whilst acquiring in focus fluorescence images simultaneously.

On the same inverted microscope platform, epi-illumination was provided from a mercury vapor short arc lamp (X-Cite 120PC Q, Lumen Dynamics) for fluorescence imaging. The filter turret contains a cube equipped with 480/40 excitation, 535/50 emission, and 505 long pass dichroic filters (41001, Chroma) which were selected based on the fluorescent dye spectra. Fluorescence emission was imaged by a charge-coupled device (CCD) camera (Orca-R2, Hamamatsu) mounted to the left port of the inverted microscope. Micromanager software (https://micro-manager.org/) was utilized to control image acquisition and timing the delivery of laser pulses[66]. Coupling the laser to a microcontroller board (UNO, Arduino) enabled the ability to time microbeam delivery via computer software.

Time-resolved imaging to photograph µCBs and determine their dynamics was accomplished using an ultra-fast gated intensified charge-coupled device (ICCD) camera (4-Picos, Stanford Computer Optics). The illumination for imaging was provided by fluorescence emission from a dye cell (LDS 698, Exciton) pumped with a separate λ = 532 nm frequency-doubled Q-switched Nd:YAG laser (Brilliant B, Quantel). Illumination from the dye cell was collected and directed to the microscope condenser via fiber optic. Timing of the µCB producing laser, imaging illumination, and camera gate were controlled with a delay generator (BNC Model 575, Berkeley Nucleonics Corporation). Electronic signals were examined on an oscilloscope (TDS 2024, Tektronix) for synchronizing the camera gate and illumination relative to the µCB inducing laser.

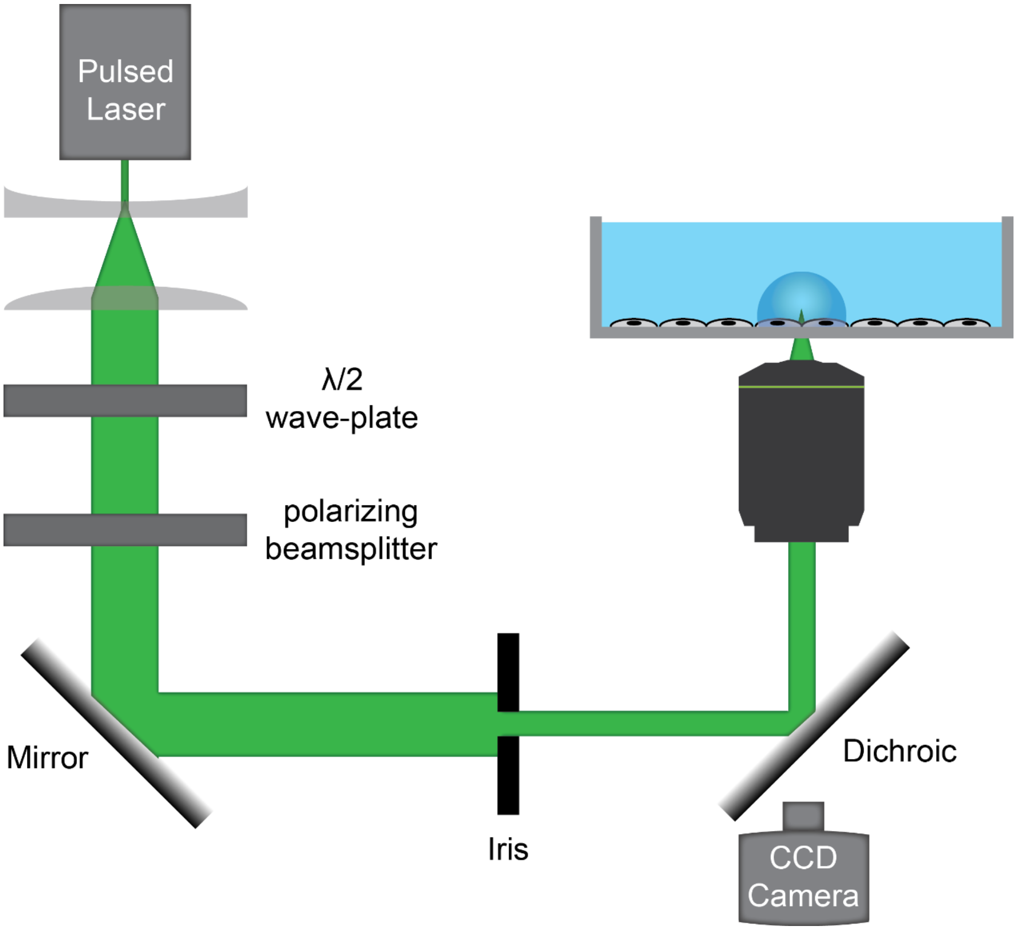

Fig. 2-4 | µTsunami platform. Pulsed laser integrated into a standard inverted fluorescence microscope. An objective focuses the pulsed laser microbeam and initiates the µTsunami 10 µm above a monolayer of cells. The cellular response from shear stress impulse exposure is imaged by a CCD camera. The laser microbeam pulse energy is tuned via λ/2 wave-plate and polarizing beamsplitter.

Cell Culture

Primary HUVECs (generously provided by Prof. Chris Hughes; University of California, Irvine) at passage 4 were cultured in 35 mm #1.5 glass-bottomed dishes (FluoroDish, WPI) coated with 4.61 µg·cm^{-2} fibronectin derived from human plasma (F2006, Sigma) to confluency in Endothelial Cell Basal Medium-2 (EBM-2) supplemented with Endothelial Cell Growth Medium-2 (EGM-2) BulletKit (CC-3162, Lonza).

Ca^{2+} Indicator Loading and Imaging Experiment

Prior to indicator loading, HUVEC cultures were washed thrice using Hank's Balanced Salt Solution with Ca^{2+} as well as Mg^{2+} ions (HBSS+) and no phenol red (14025-092, Gibco). Fluo-3/AM (F-1242, Molecular Probes), a fluorescent dye that increases emission upon binding to intracellular calcium, was dissolved in 20 mM HEPES (15630-080, Gibco) buffered HBSS+ (HHBSS+) supplemented with 2 g·L^{-1} D-(+)-glucose (G7021, Sigma) and 0.5% DMSO (276855, Sigma) as the probe vehicle. HUVECs were incubated in 5 µM Fluo-3/AM for 45 min at 37°C and 5% CO_2. The cells were rinsed thrice with HBSS+ following dye loading and incubated in EGM-2 for 30 min at 37°C and 5% CO_2. Before experimentation, HUVECs were cleansed thrice using Hank's Balanced Salt Solution with neither Ca^{2+} nor Mg^{2+} ions (HBSS-) and without phenol red (14175-095, Gibco). During the imaging experiment, HUVECs were kept on Ca^{2+}-free 20 mM HEPES buffered HBSS- (HHBSS-) supplemented with Mg^{2+} ions, 2 g·L^{-1} D-(+)-glucose, and 3 mM EGTA to chelate any remaining traces of extracellular calcium[67].

A time-series of the Ca^{2+} signalling response was acquired over 35 s in intervals of 1 s with µTsunami delivery following the 5 s mark. Application of µTsunamis to HUVEC cultures and Ca^{2+} imaging were performed at room temperature.

Chemical Agonist and Antagonists

HUVEC cultures following µTsunami exposure were chased with 50 µM ATP (A6559, Sigma) to confirm their responsivity by chemically initiating Ca^{2+} signalling. The IP_3 receptor was inhibited by the addition of 10, 30, and 100 µM 2-APB (D9754, Sigma).

Cell Patterning

HUVECs were patterned in a pinwheel configuration using standard soft lithography and microfluidic techniques[68,69].

HUVEC Lysate

HUVECs were grown to confluency in a T25 tissue culture flask, lifted using TrypLE (12605-010, Gibco), and resuspended in HBSS- without phenol red at a concentration of 1.5 x 10^7 cells·mL^{-1}. HUVEC lysate was prepped by subjecting cells to repeated freeze-thaw cycles at -80°C followed by sonication on ice for 30 s.

Mock High-Throughput Screen

HUVECs were plated in #1.5 glass-bottomed 96 well-plates (P96-1.5H-N, In Vitro Scientific) coated with fibronectin. For the HTS conditions, we administered the following small molecules to every well in each column: (1-2) 100 µM 2-APB, (3-4) 10 µM 2-APB, (5) 10 µM PP2 (P0042, Sigma), (6) 50 nM (±)-Verapamil hydrochloride (V4629, Sigma), (7) 10 µM Cytochalasin D (C8273, Sigma), (8) 20 µM Nocodazole (M1404, Sigma), (9) 20 µM (–)-Blebbistatin (B0560, Sigma), (10-11) no compounds or control, and (12) 5% DMSO.

2.4 Results and Discussion

A full cavitation bubble oscillation cycle acquired by time-resolved photography for µCBs initiated 10 µm above a monolayer of HUVECs is portrayed in Fig. 2-5. A single full µCB cycle which consists of the formation, expansion, and collapse was observed to occur within tens of microseconds. Cavitation bubble dynamics are characterized from these images by measuring their sizes in order to determine the maximum radius. With R_{max} of the µCB empirically determined, we input this value into the Gilmore equation to predict dynamics theoretically. The theoretical µCB dynamics utilized in conjunction with our hydrodynamic model enable computation of the shear stress impulse at any location radially relative to the site of µTsunami delivery. The R_{max} is particularly important as it alone not only uniquely dictates µCB dynamics, but also determines cellular exposure to µTsunami initiated shear stress impulses. Moreover, µCB R_{max} is readily varied by adjusting laser pulse energy to enable application of tailored shear stress impulse profiles. These features of cavitation bubble dynamics provide tunability in our application of mechanical perturbation. For our experiments, we utilized a pulse energy of E_p = 5 µJ which resulted in R_{max} = 108 µm µCBs.

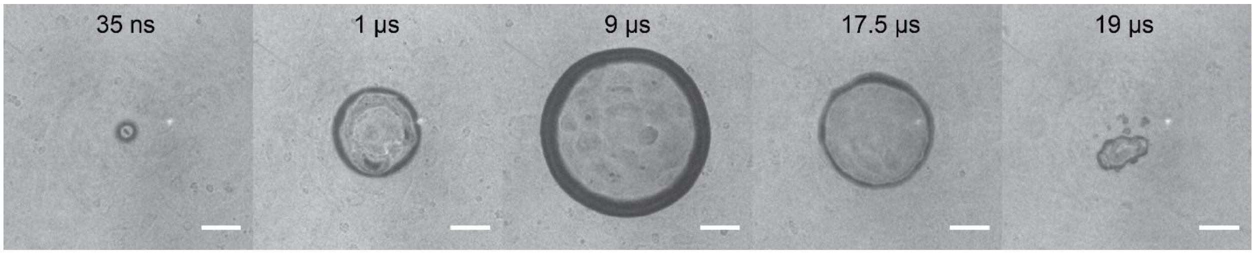

Fig. 2-5 | µCB cycle captured by time-resolved imaging above a HUVEC monolayer. Images of µCBs with R_{max} = 108 µm produced at separate time points by E_p = 5 µJ laser pulses. Scale bar = 50 µm.

Fig. 2-6 illustrates the shear stress impulse computed for µCBs of varying maximum sizes plotted against increasing radial distance relative to the µTsunami delivery site. Our hydrodynamic model predicted the reduction of impulse at further radial distances due to fluid compressibility as intuitively expected. Other than the impulse at radial regions immediately proximal to the site of µTsunami initiation, the quantities we calculated are slightly lower than physiological shear stress impulses experienced by human vascular endothelial cells which ranges from 0.1-10 Pa·s[70]. This is easily rectified by tuning laser pulse energy to alter the µCB size to achieve induction of µTsunamis that generate impulses within physiological ranges.

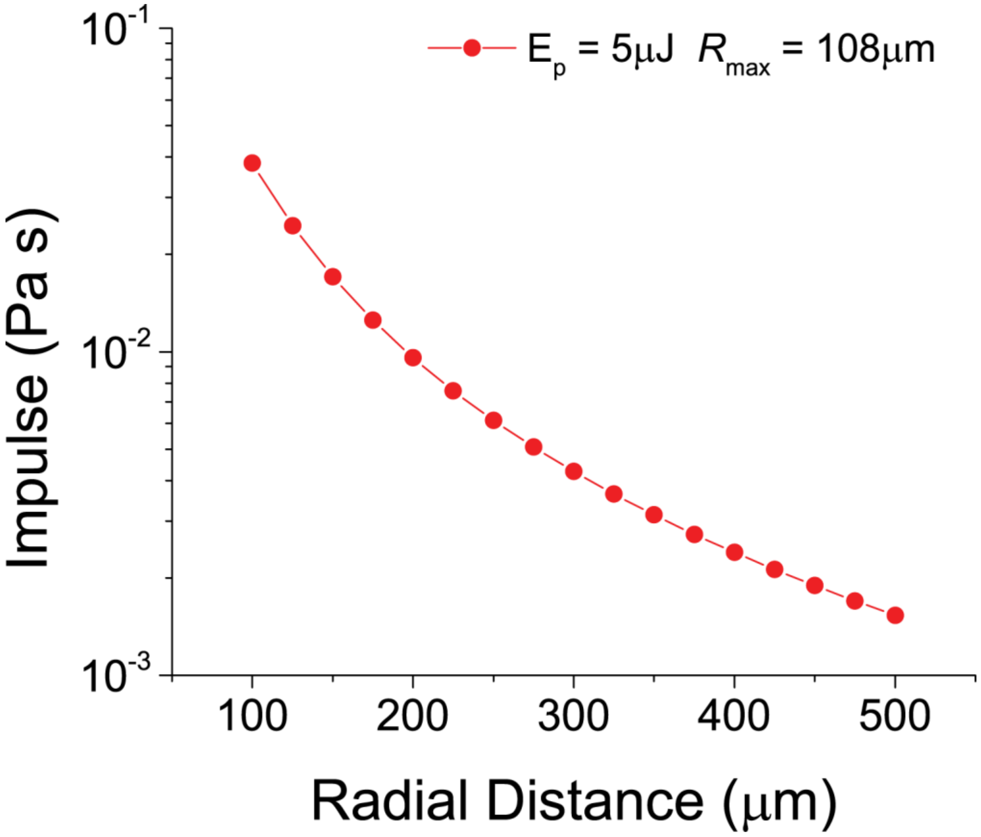

Fig. 2-6 | μTsunami generated shear stress impulse for R_{max} = 108 μm μCBs produced by E_p = 5 μJ laser pulses.

HUVECs initiated Ca^{2+} signalling following exposure to μTsunami shear stress impulses produced by μCBs with R_{max} = 108 μm generated by delivery of a single E_p = 5 μJ laser pulse. The Ca^{2+} cascade, indicated by an intensity increase, propagated radially outward from the site of μTsunami initiation as observed in Fig. 2-7.

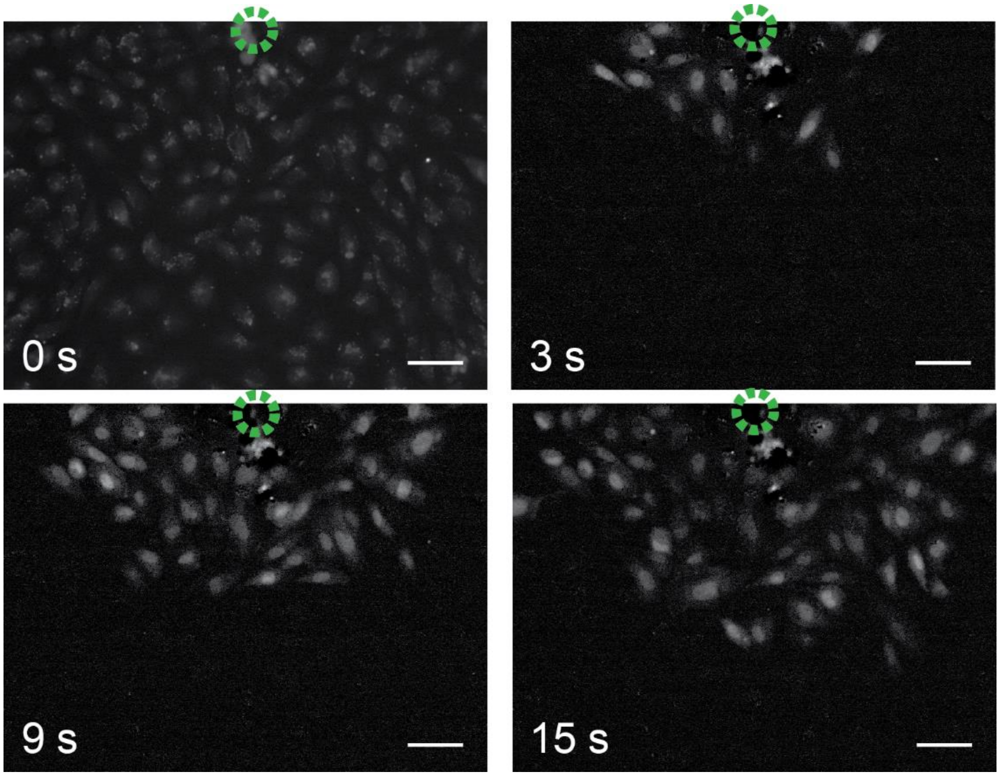

Fig. 2-7 | Fluorescence image-series of µTsunami initiated intracellular Ca^{2+} signalling in a HUVEC monolayer. The dotted green circle signifies the location where a µCB of R_{max} = 108 µm from E_p = 5 µJ laser pulse was delivered for µTsunami exposure. Scale bar = 50 µm.

From the image time-series, we discovered latency in the calcium signalling propagation with increasing radial distance. Fig. 2-8 demonstrates this latency where we plotted signalling delay, the point in time at which HUVECs exhibited the Ca^{2+} cascade relative to time of the laser pulse, against radial distance from the µCB center. By linear regression, we estimated the slope or calcium wave speed as 4.5 ± 0.3 $\mu m \cdot s^{-1}$ which corroborates the increase in delay with further radial distance. This latency was also reported in a study of cytosolic Ca^{2+} signalling stimulated in endothelial cells from the bovine aorta in response to high shear stress conditions using flow chambers[71]. Interestingly, we also discovered signalling delays in cells immediately proximal to the µTsunami initiation site.

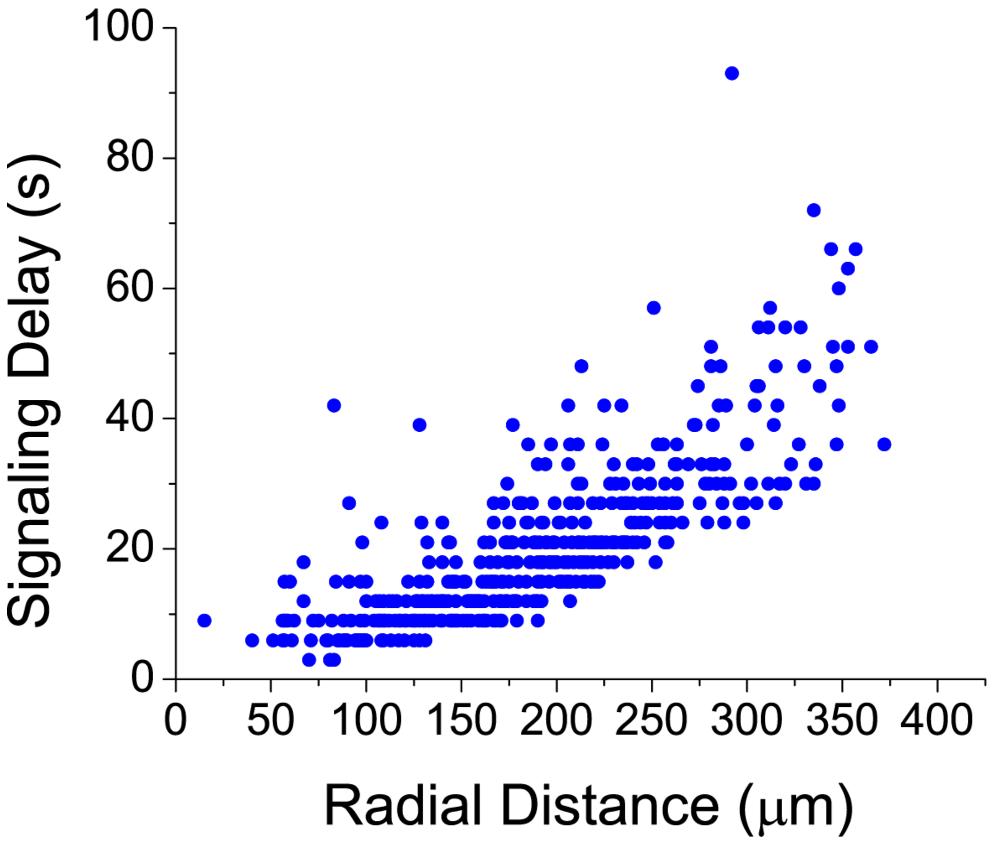

Fig. 2-8 | Ca^{2+} signalling latency with increasing radial distance relative to the R_{max} = 108 µm µCB center. The delay was characterized in 447 cells that exhibited signalling from monitoring a total of 765 HUVECs.

We postulated that the observed signalling dynamics is due to the concentration of diffusible mediator IP$_3$ available within the cytosol of each cell for the probabilistic induction of Ca^{2+} signalling. Potentially, this is dictated by the magnitude of shear stress impulse exposed to each cell depending on their radial location which translates to the amount of IP$_3$ produced. The amount generated as well as transport of IP$_3$ by diffusion to its receptor would result in the observed latency and modulate the probability of Ca^{2+} signalling. This entails decreasing Ca^{2+} signalling probabilities in HUVECs producing less IP$_3$ due to being exposed to lower impulses with increasing radial distance from the µCB center. We plotted in Fig. 2-9 the Ca^{2+} signalling probability and impulse, both initiated from R_{max} = 108 µm µCBs by a single E_p = 5 µJ pulsed laser microbeam, against radial distance. These results confirm our postulate where the signalling probability and impulse decline with increasing radial distances. HUVECs situated close to the µCB displayed low signalling probabilities which is likely due to becoming lysed, necrotic, and transiently permeabilized as supported by our previous work[44,45,57].

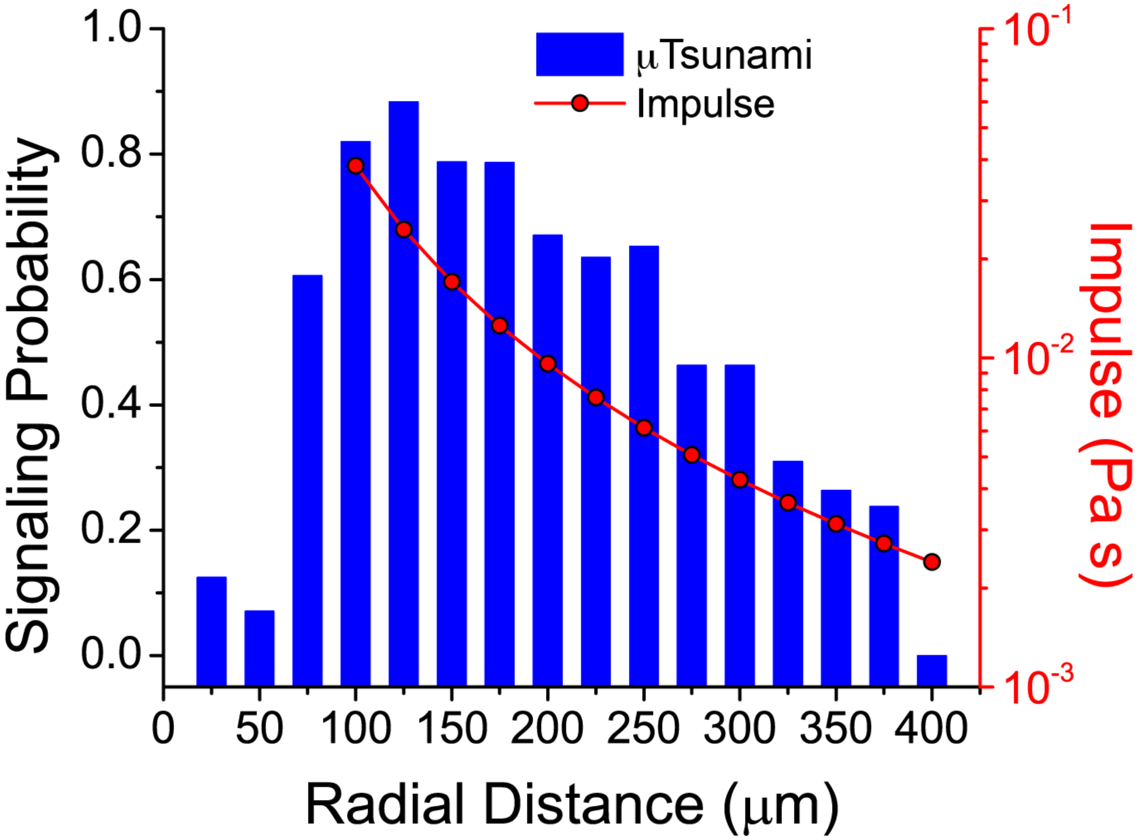

Fig. 2-9 | Ca^{2+} signalling probability and shear stress impulse with increasing distance radially from the delivery site of a µTsunami generated by R_{max} = 108 µm µCB.

For use in HTS, it is imperative that the µTsunami platform is capable of detecting alterations in mechanosignalling from administered potential therapeutic molecules such as putative inhibitors. With Ca^{2+} signalling as our readout, we tested the capability of our platform to screen for mechano-active drugs by administering a known inhibitor. 2-aminoethoxydiphenyl borate (2-APB) which inhibits Ca^{2+} signalling via competitively binding to the IP_3R for averting cationic efflux from the ER was supplied to HUVEC cultures at concentrations of 10, 30, and 100 µM. Inhibition of Ca^{2+} signalling by 2-APB with these concentrations was demonstrated previously in a study on bovine aortic endothelial cells following chemical stimulation using a bolus of ATP[72]. Application of 2-APB at varying concentrations led to the attenuation, spatially and temporally, of µTsunami induced Ca^{2+} signalling in a dose-dependent manner as depicted in Fig. 2-10 and Fig. 2-11. This demonstrates the µTsunami platform is able to detect the dose-dependent effects of exogenous inhibitors.

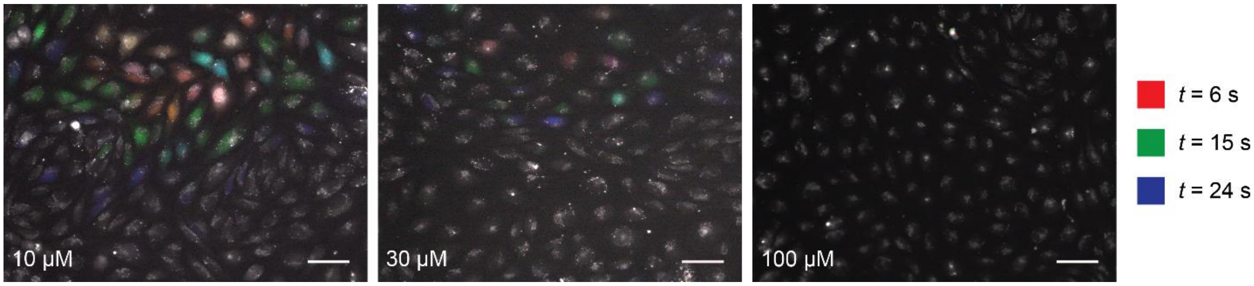

Fig. 2-10 | Dose-dependent inhibition of µTsunami initiated Ca^{2+} signalling in HUVEC monolayers administered with 10, 30, and 100 µM 2-APB. Time is mapped in color to depict the propagation of Ca^{2+} signalling for each inhibition condition: red – t = 6 s; green – t = 15 s; blue – t = 24 s. Scale bar = 50 µm.

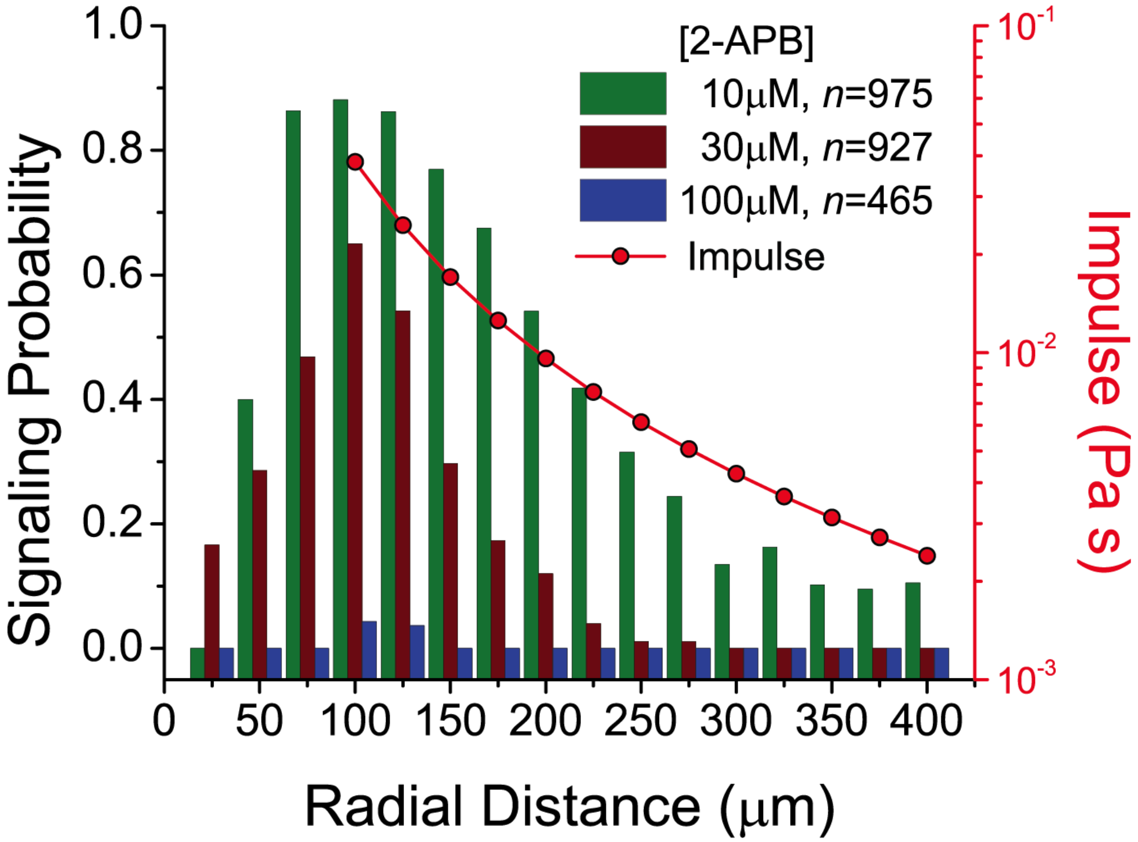

Fig. 2-11 | Dose-dependent inhibition of Ca^{2+} signalling probability with increasing concentrations of 2-APB. The variable n represents number of cells analyzed.

We automated the µTsunami platform to be high-throughput capable and conducted a mock screening experiment due to the assertion that our approach is suitable for HTS of cellular mechanotransduction. The effects of various known molecules, each with multiple replicates, on Ca^{2+} signalling were assayed in a standard 96 well-plate to determine whether they could essentially be rediscovered. For each column, the following putative compounds which served as our screening conditions were applied: (1-2) 100 µM 2-APB; (3-4) 10 µM 2-APB; (5) 10 µM phosphoprotein phosphatase 2 (PP2), a selective inhibitor for Src family tyrosine kinases; (6) 50 nM Verapamil, voltage-dependent Ca^{2+} channel blocker for hypertension treatment; (7) 10 µM Cytochalasin D, which is an anti-actin polymerization agent; (8) 20 µM Nocodazole, an inhibitor of microtubule polymerization; (9) 20 µM (-)-Blebbistatin, a selective blocker of non-muscle myosin II, (10-11) no compound or control; and (12) 5% DMSO, the dye as well as drug vehicle.

The results of our mock HTS are summarized in Fig. 2-12 where we reported the Ca^{2+} signalling probability within a 100-150 µm annulus for each well. This annular region is where the highest probabilities of Ca^{2+} signalling are exhibited by HUVECs situated at a radial distance closest to the maximum µCB radius. The degree of inhibition in the signalling probability potentially enables us to determine the effectiveness of potential drug compounds. For 2-APB added in columns 1-2 and 3-4 at 100 µM and 10 µM, respectively, we observed a dose-dependent inhibitory effect on Ca^{2+} signalling which affirms our earlier results. PP2 as well as Verapamil, administered in columns 5 and 6, appeared to have no effect on calcium signalling as anticipated since these chemicals act on specific pathways unrelated to cationic release from the ER. Interestingly, we discovered disrupting the HUVEC cytoskeleton led to contrasting results. Administering Cytochalasin D as well as Nocodazole for columns 7 and 8 mildly inhibited calcium signalling whereas the addition of (-)-Blebbistatin in column 9 did not appear to affect the cascade. Perhaps, further studies are required to investigate the role of cytoskeleton in mechanosensing and Ca^{2+} signalling. In columns 10-11, the control where HUVECs were kept on Ca^{2+}-free buffer only without any small molecules administered signalled as anticipated. For column 12, Ca^{2+} signalling was observed from HUVECs in the presence of 5% DMSO which demonstrates the dye and drug vehicle itself was neither cytotoxic nor affected the cellular response. The duration of time to conduct this mock HTS experiment on calcium mechanosignalling was approximately 56 min. This time was necessary due to the constraints of Ca^{2+} signalling dynamics where we imaged each well for 35 s with 1 s intervals. A readout with signalling dynamics occurring on a faster timescale potentially enables quicker screens. These results not only establish the µTsunami platform as suitable for HTS of cellular mechanotransduction, but also the capability to rapidly perform experiments and investigate mechanosignalling pathways while building strong statistics.

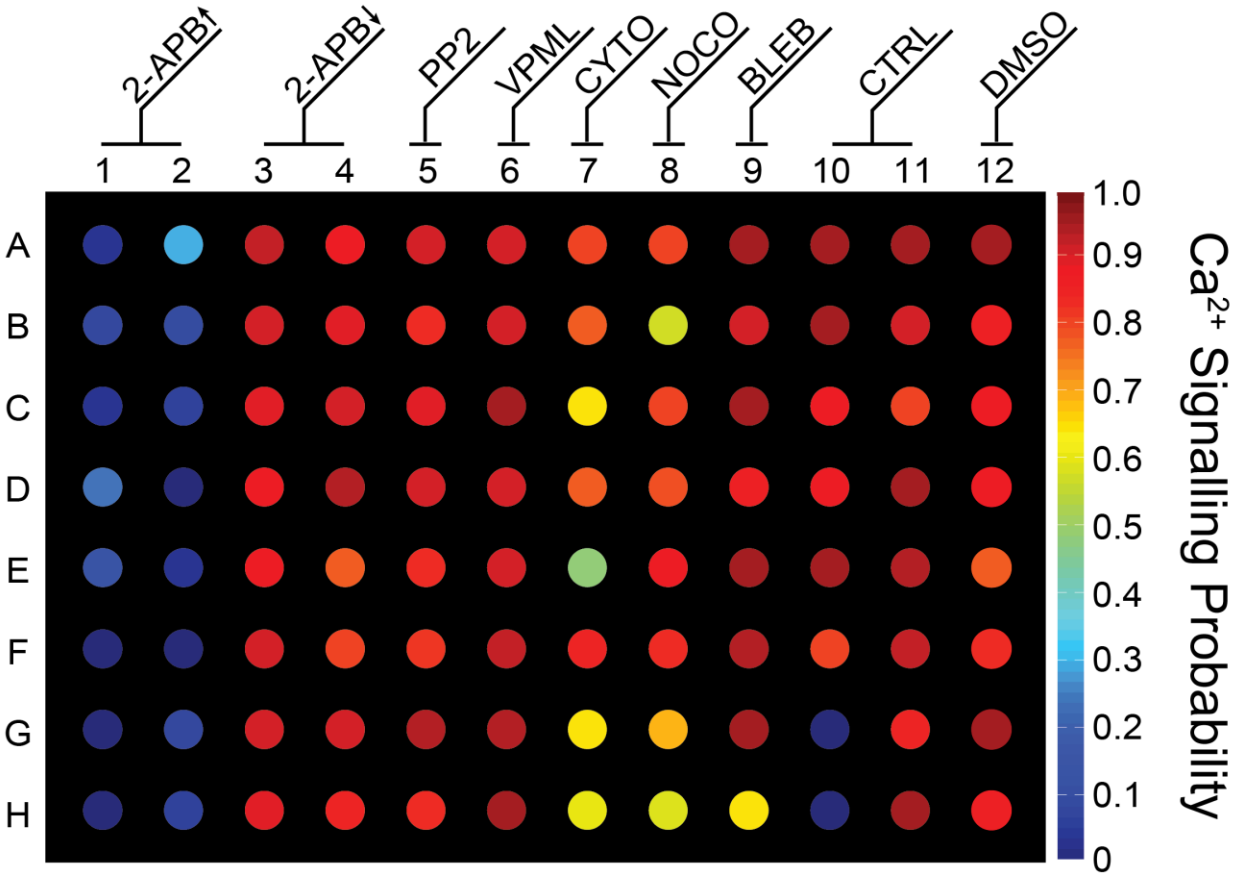

Fig. 2-12 | Mock high-throughput screening of Ca^{2+} mechanosignalling in a standard 96 well-plate. HUVECs were in the presence of the following exogenous putative compounds: (1-2) 100 µM 2-APB, (3-4) 10 µM 2-APB, (5) 10 µM PP2, (6) 50 nM (±)-Verapamil hydrochloride, (7) 10 µM Cytochalasin D, (8) 20 µM Nocodazole, (9) 20 µM (–)-Blebbistatin, (10-11) Control, and (12) 5% DMSO. Color represents the Ca^{2+} signalling probability reported in a 100-150 µm annular region. The median percentage of HUVECs that signalled for columns 1-12: 3, 6, 94, 93, 91, 96, 75, 84, 99, 92, 98, and 91%.

We postulated the Ca^{2+} signalling response observed in HUVECs was initiated mechanically via exposure to µTsunami generated shear stress impulses. Instead of stimulating mechanotransduction, it remains a possibility that intracellular Ca^{2+} signalling was activated via HUVEC lysate produced from µCB initiation. Lysate presumably contains diffusible factors, capable of inducing the Ca^{2+} cascade including ATP, which are transported to distal cells. To counter this notion, we must confirm that lysate alone is not responsible for the observed Ca^{2+} signalling. Fig. 2-13 depicts our results from investigating the effects of lysate when administered into HUVEC cultures. As expected in our negative control, HUVECs without exposure to µTsunami, lysate, and ATP exhibited no Ca^{2+} signalling. HUVECs exposed to lysate alone also displayed no Ca^{2+} signalling response. Interestingly, the addition of lysate following µTsunami exposure resulted in low levels of Ca^{2+} signalling comparable to the negative control. Chasing with ATP itself and following the administration of lysate, instead of µTsunami, led to signalling probabilities >90% and 60%, respectively.

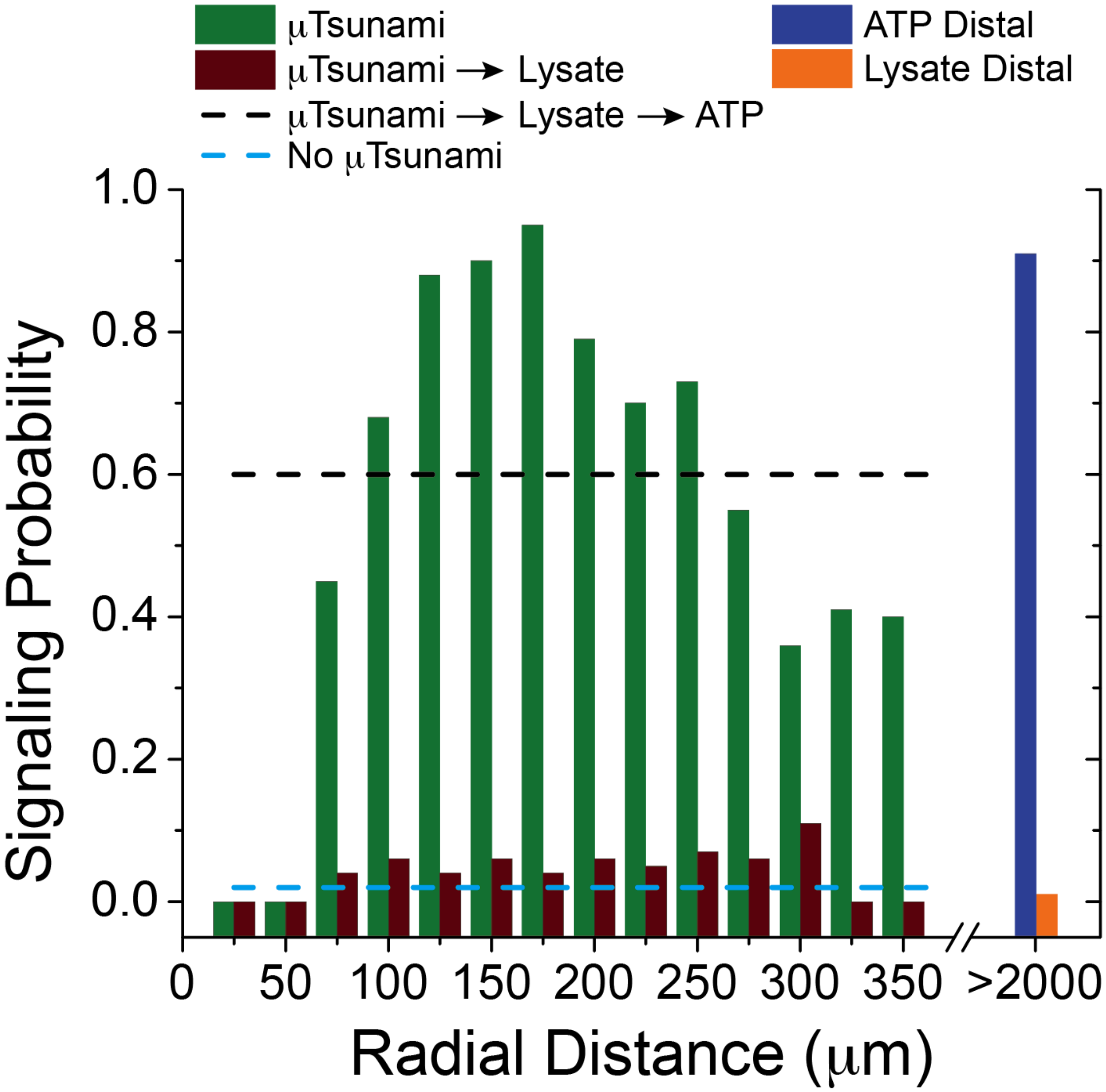

Fig. 2-13 | Ca^{2+} signalling probability of HUVECs in response to lysate. The dotted cyan line denotes Ca^{2+} signalling probability response in n = 239 HUVECs exposed to no µTsunami, lysate, and ATP which is our negative control. Green bars indicate the Ca^{2+} signalling response initiated by µTsunamis alone analyzed in n = 356 cells. Burgundy bars signify the addition of lysate following µTsunami exposure in n = 716 cells where low levels of Ca^{2+} signalling comparable to the negative control was observed. Probability of the Ca^{2+} cascade monitored in n = 310 HUVECs exposed to lysate alone corresponds to the orange bar which also yielded low levels of signalling. Our positive control from chasing n = 310 cells with ATP is indicated by the single blue bar. The black dotted line designates administration of ATP to n = 712 cells following µTsunami and lysate exposure.

HUVECs were cultured in a pinwheel configuration by patterning fibronectin using standard microfluidic and soft lithography methods as portrayed in Fig. 2-14a. Following µTsunami delivery within a region free of cells for preventing lysate production, the strip of HUVECs immediately adjacent to the induction site as well as HUVECs in a distal strip separated by a separate cell-free zone displayed Ca^{2+} signalling which is evidenced in Fig. 2-14b. These results demonstrate the Ca^{2+} signalling response observed in HUVECs following µTsunami exposure was initiated from shear stress impulse exposure and not dictated by lysate/diffusible factors generated proximal to the µCB or µCB-cell contact.

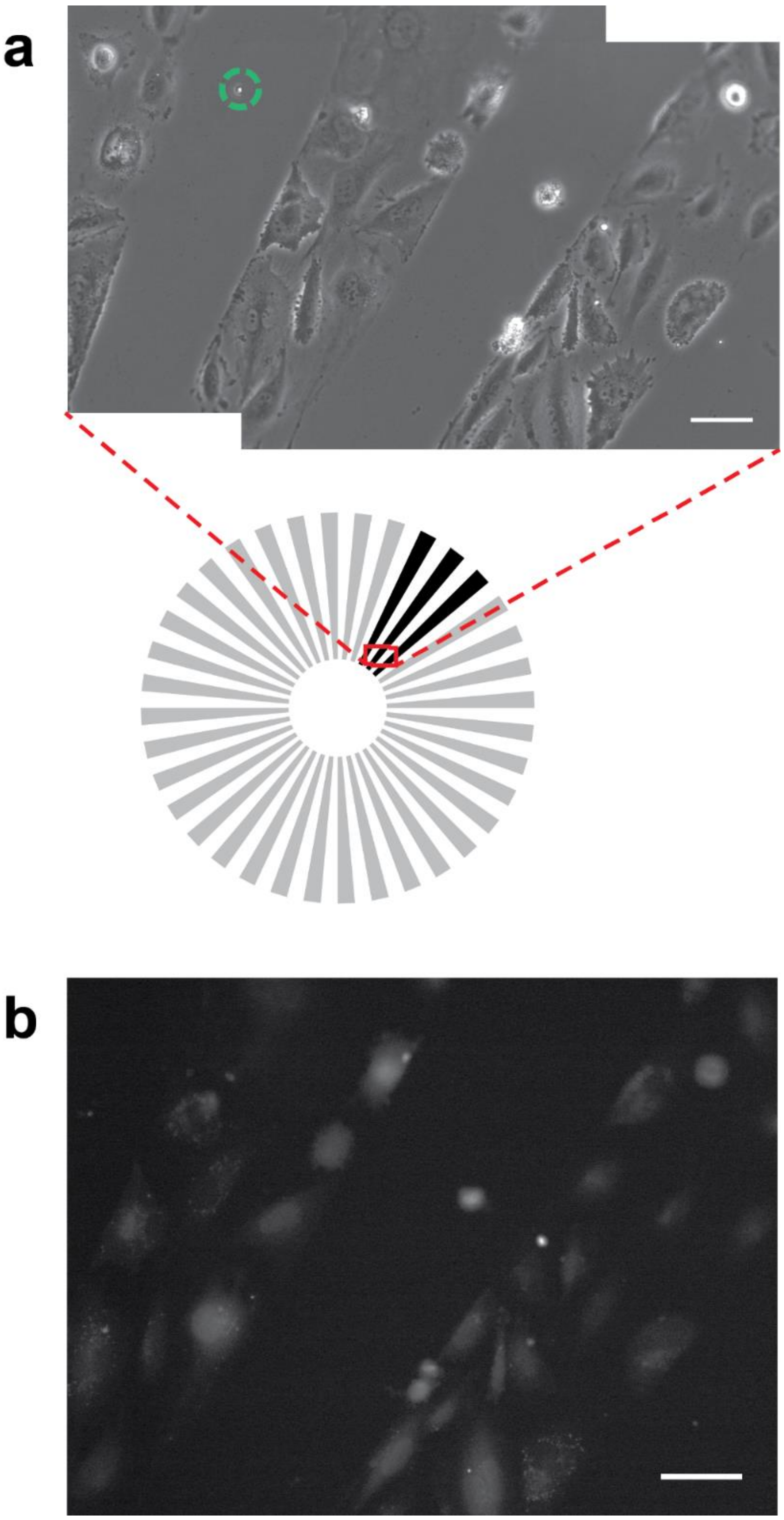

Fig. 2-14 **|** µTsunami initiated Ca^{2+} signalling is independent of diffusible factors and µCB-cell contact. **a**, HUVECs cultured in a pinwheel configuration by patterning fibronectin to form alternating regions with confluent spokes and cell-free zones. The dotted green circle marks µCB origin. **b**, Fluorescence image of HUVECs in the confluent pinwheel spokes exhibiting cytosolic Ca^{2+} signalling initiated by a µTsunami delivered in the cell-free zone. Scale bar = 50 µm.

2.5 Conclusion

These reported findings collectively establishes the µTsunami platform we developed, which integrates pulsed laser-induced µCBs and standard fluorescence microscopy, is capable of HTS and investigation of cellular mechanotransduction. This was demonstrated through a series of investigations that involved: (a) quantifying the magnitude of shear stress impulses to correlate µTsunami exposure with the signalling response, (b) determining µTsunamis are capable of activating mechanotransduction in primary adherent HUVECs as indicated by initiation of Ca^{2+} signalling, (c) detecting dose-dependent Ca^{2+} signalling inhibition by adding the putative inhibitor 2-APB to HUVEC cultures which affirmed the usability of our platform for screening, and (d) conducting a mock screening HTS experiment in a standard 96 well-plate using the automated µTsunami platform. Moreover, we also determined µTsunami initiated Ca^{2+} signalling is independent of lysate/diffusible factors and µCB-cell contact which supports our claim of activating mechanotransduction by shear stress impulse exposure. For the drug discovery process, the µTsunami approach presents a HTS platform with the potential to identify hits and repurpose current therapeutics capable of modulating cellular mechanotransduction.

Chapter 3

Mechanism of µTsunami Initiated Ca^{2+} Mechanosignalling in HUVECs

3.1 Introduction and Background

In the previous chapter, we presented an optical technology for high-throughput screening of potential drug compounds capable of targeting and modifying cellular mechanotransduction pathways known as the µTsunami platform. The ability to evoke calcium signalling in confluent HUVEC monolayers with our µTsunami method led us to postulate a specific biomolecular mechanism for the observed signalling. However, evidence supporting such a mechanism arising from µTsunami stimulation has yet to be reported[73]. In this chapter, we address the underlying molecular pathway and stimulatory mechanism involved in µTsunami initiated Ca^{2+} mechanosignalling[74]. In addition, we also give attention to the application of the µTsunami platform to investigate cellular mechanotransduction.

Previously, mechanical activation of the IP_3 pathway was inferred to elicit the observed cytosolic calcium cascade in HUVECs post-µTsunami exposure. We theorized that the activation of the IP_3 pathway is initiated through mechanical stimulation of stretch-sensitive G Protein-Coupled Receptors (ssGPCRs) at the cell surface due to impulsive shear stresses generated from the µTsunami. The $\alpha_{q/11}$ subunit of the G Protein shuttles off and interacts with phospholipase C β (PLCβ) bound to the inner cell membrane. PLCβ cleaves phosphatidylinositol 4,5-biphosphate (PIP_2), which is restricted to the plasma cell membrane, via hydrolysis into inositol 1,4,5-triphosphate (IP_3) and diacylglycerol (DAG). IP_3 diffuses and binds to the IP_3 receptor (IP_3R) which releases Ca^{2+} ions stored within the endoplasmic reticulum (ER) into the cytoplasm[75].

Our administration of 2-aminoethoxydiphenyl borate (2-APB), a competitive binder of the IP_3R, demonstrated inhibition of µTsunami initiated Ca^{2+} signalling. The reasons that this inhibition result itself is unable to exclude involvement of other potential pathways are two-fold: (1) competitive inhibition occurs at the IP_3R level which lies downstream from the mechanically stimulated stretch-sensitive GPCRs and (2) 2-APB is a non-specific antagonist of proteins or receptors connected to Ca^{2+} signalling[76]. Presumably, intracellular Ca^{2+} signalling induced by diffusible factors released from cells proximal to the µTsunami that activates a purinergic pathway remains a possibility. P2X (ligand-gated ion channels) and P2Y (GPCRs) are purinergic receptors that specifically activate by chemical factors including ATP[77]. Purinoceptor activation induces calcium signalling via either ionic influx from the extracellular space (P2X) or biochemical activation of the IP_3 cascade (P2Y). The influx of calcium through ion channels that are activated by stretch is also possible. Fig. 3-1 depicts these possible pathways for inducing intracellular calcium signalling via activation of GPCRs and ion channels that are either stretch-sensitive or purinergic receptors.

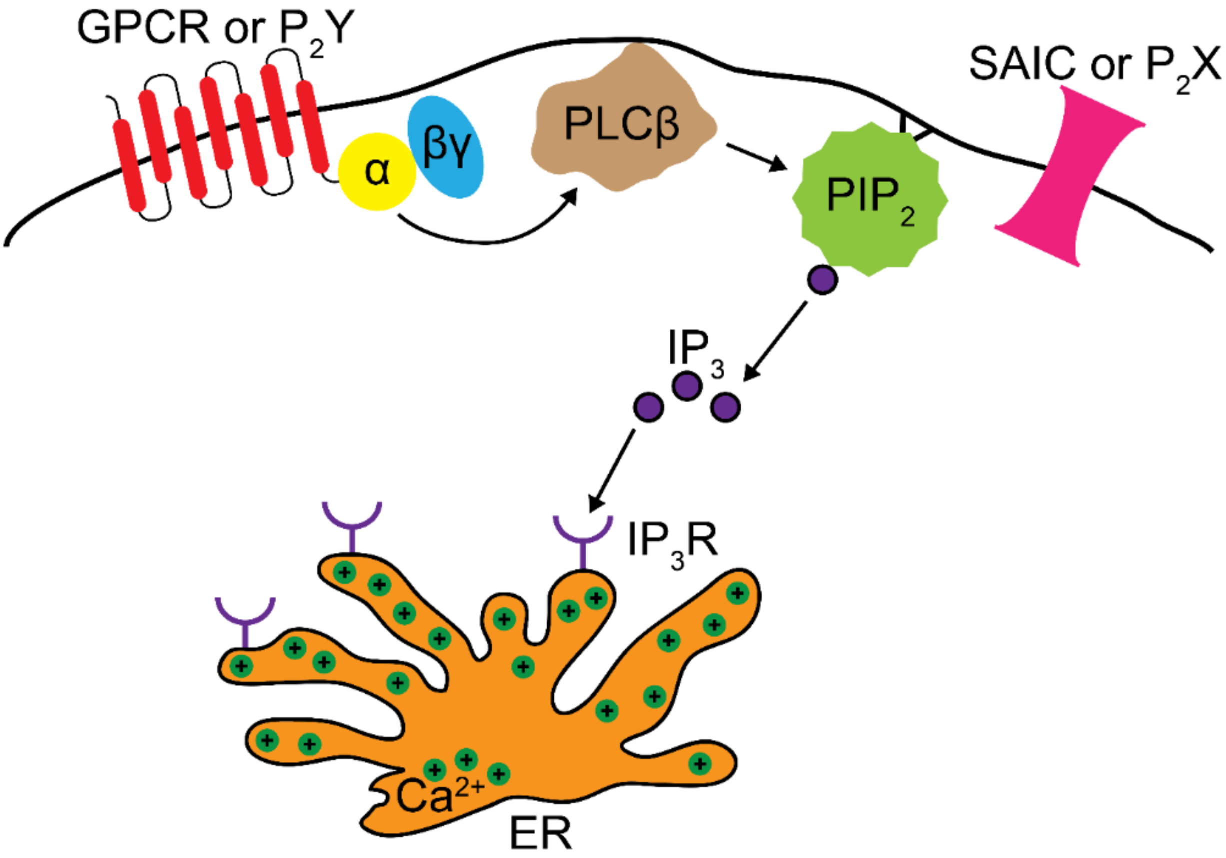

Fig. 3-1 | IP_3 pathway, stretch-sensitive receptors, and purinoceptors.

Therefore, further inhibition experiments along the IP_3 pathway and purinergic receptors are necessary to confirm our hypothesis. Moreover, we tested the ability to modulate the spatial range of the calcium cascade propagation by varying impulse severity and mapped a dose-response relationship to ascertain the mechanical nature of µTsunamis.

3.2 Materials and Methods

µTsunami Platform

The laser microscope setup detailed in Fig. 2-4 was also employed here. Briefly, 500 ps duration pulses at λ = 532 nm emitted from a Q-switched pulsed microchip laser (PNG-M03012, Teem Photonics) created µTsunamis. We used a pair of diverging and converging lenses with focal lengths *f* of -25 mm and 500 mm, respectively, to expand and collimate the laser microbeam. Pulse energy was controlled via λ/2 wave-plate and polarizing beamsplitter. An iris cropped the outer laser beam edge to allow only the central portion to enter the right port of an inverted microscope (IX-81, Olympus). The laser pulse was directed by a dichroic mirror (ZT532NBDC, Chroma) to the rear aperture of a 20x 0.45 NA objective (LUCPlanFLN, Olympus) which focused the beam 10 µm above the HUVEC monolayer. This offset was introduced by slightly defocusing the laser microbeam collimation that enabled placement of the laser microbeam focus at a height of 10 µm above the imaging plane while simultaneously acquiring images of cellular fluorescence.

Fluorescence imaging was accomplished using epi-illumination was provided from a mercury vapor short arc lamp (X-Cite 120PC Q, Lumen Dynamics). The filter turret contains a cube equipped with 480/40 excitation, 535/50 emission, and 505 long pass dichroic filters (41001, Chroma) which were selected based on the absorption/emission spectra of the fluorescent dye Fluo-3/AM. Fluorescence emission was imaged by a charge-coupled device (CCD) camera (Orca-R2, Hamamatsu) mounted to the left port of the inverted microscope. Micromanager software (https://micro-manager.org/) was utilized to control image acquisition and timing the delivery of laser pulses[66]. Coupling the laser to a microcontroller board (UNO, Arduino) enabled the ability to control microbeam delivery via computer software.

Cell Culture

Primary HUVECs (generously provided by Prof. Chris Hughes; University of California, Irvine) at passage 4 were cultured in 35 mm #1.5 glass-bottomed dishes (FluoroDish, WPI) coated with 4.61 $\mu g \cdot cm^{-2}$ fibronectin derived from human plasma (F2006, Sigma) to confluency in Endothelial Cell Basal Medium-2 (EBM-2) supplemented with Endothelial Cell Growth Medium-2 (EGM-2) BulletKit (CC-3162, Lonza).

Ca^{2+} Indicator Loading and Imaging Experiment

Prior to indicator loading, HUVEC cultures were washed thrice with Hank's Balanced Salt Solution with Ca^{2+} as well as Mg^{2+} ions (HBSS+) and without phenol red (14025-092, Gibco). Fluo-3/AM (F-1242, Molecular Probes), a fluorescent dye that increases emission upon binding to cytosolic calcium, was dissolved in 20 mM HEPES (15630-080, Gibco) buffered

HBSS+ (HHBSS+) supplemented with 2 g/L D-(+)-glucose (G7021, Sigma) and 0.5% DMSO (276855, Sigma) as the probe vehicle. HUVECs were incubated in 5 µM Fluo-3/AM for 45 min at 37°C and 5% CO_2. The cells were rinsed thrice with HBSS+ following dye loading and incubated in EGM-2 for 30 min at 37°C and 5% CO_2. Before experimentation, HUVECs were cleansed thrice with Hank's Balanced Salt Solution with neither Ca^{2+} nor Mg^{2+} ions (HBSS-) and no phenol red (14175-095, Gibco). HUVECs were kept on Ca^{2+} free 20 mM HEPES buffered HBSS- (HHBSS-) supplemented with Mg^{2+} ions, 2 g/L D-(+)-glucose, and 3 mM EGTA to chelate any remaining traces of extracellular calcium during the imaging experiment[67].

A time-series of the Ca^{2+}-signalling response was acquired over 35 s in intervals of 1 s with µTsunami delivery following the 5 s mark. Application of µTsunamis to HUVEC cultures and Ca^{2+} imaging were performed at room temperature.

Chemical Agonist and Antagonists

HUVEC cultures following µTsunami exposure were chased with 50 µM ATP (A6559, Sigma) to confirm their responsivity by chemically initiating Ca^{2+} signalling. Purinoceptors were inhibited by treatment with Cibacron Blue 3G-A (ab141504, abcam) and PPADS (sc-202770, Santa Cruz Biotechnology) at doses up to 100 µM. PLCβ was antagonized by 20 µM U-73122 (BML-ST391, Enzo Life Sciences). 200 ng/mL Pertussis Toxin (P7208, Sigma) and 100 µM Suramin (S2671, Sigma) were utilized to broadly interfere with GPCRs.

3.3 Results and Discussion

The possibility of evoking Ca^{2+} signalling in HUVECs by diffusible factors secreted from cells proximal to the µTsunami was addressed by our results from lysate[37] administration reported in the previous Chapter 2.4. We reported that HUVECs exhibited minimal calcium signalling following administration of its lysate which presumably contains the released factors, supposedly due to µTsunami exposure, capable of activating purinoceptors including ATP. HUVECs were also kept on buffer free of calcium with EGTA during experiments to chelate traces of external Ca^{2+} ions, if any, for ensuring that the detected cascade originated internally and prevents involvement of ion channels such as P2X receptors in the observed signalling. To further investigate the extent of purinergic involvement, we conducted inhibition studies by administering antagonists of P2X and P2Y receptors to HUVEC cultures. Treatment with Cibacron Blue 3G-A and PPADS, for broad purinoceptor inhibition, at doses up to 100 µM were surprisingly ineffective in abolishing Ca^{2+} signalling chased chemically by a bolus of ATP which questions their effectiveness. Moreover, purinergic receptors of various subtypes $P2X_1$, $P2X_2$, $P2X_4$, $P2X_6$, $P2X_7$, $P2Y_1$, $P2Y_2$, and $P2Y_{11}$ are established to be expressed in HUVECs[78]. However, the current literature expresses uncertainty regarding the efficacy of these compounds as well as susceptibility to target and poison purinergic subtypes expressed by HUVECs[79,80]. These results cast doubt that µTsunami initiated calcium signalling is dictated by purinergics.

Our focus shifted towards dissecting the IP_3 pathway and we conducted inhibition experiments on key molecular proteins involved in the activation of calcium signalling. We examined the effect of blockers on Ca^{2+} signalling in HUVECs evoked by µTsunamis and ATP. PLCβ, whose activation occurs immediately downstream of GPCRs, was antagonized by the administration of 20 µM U-73122. Following treatment with U-73122, we discover a 68.8% suppression in the cytosolic Ca^{2+} cascade due to µTsunami exposure and signalling by ATP was not significantly affected as illustrated in Fig. 3-2. 81.9% and 82.5% of HUVECs exhibited Ca^{2+} signalling from ATP induction with and without U-73122, respectively.

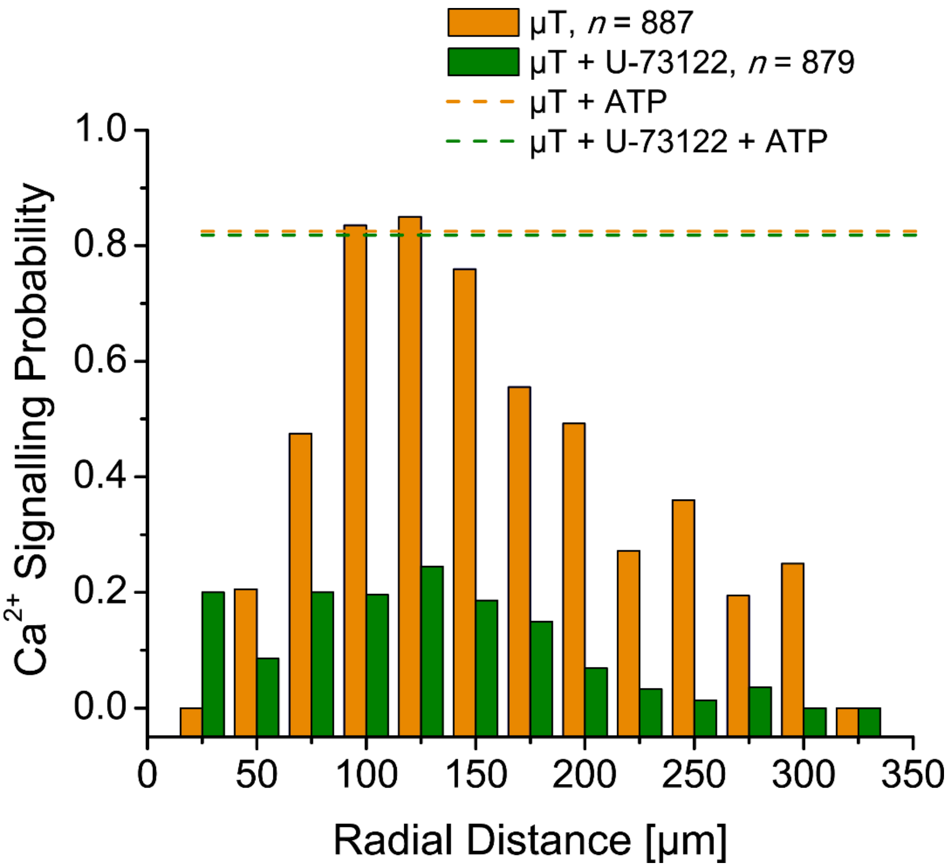

Fig. 3-2 | Probability of Ca^{2+} signalling in HUVECs via μTsunamis or exogenous ATP administration with or without U-73122 presence. Solid bars indicate calcium signalling probabilities from μTsunami stimulation with n being the number of cells analyzed. Dotted horizontal lines signify probabilities of Ca^{2+} signalling by administering ATP following μTsunami exposure with and without U-73122 inhibition. μTsunamis were generated from a laser pulse of E_p = 5 μJ that resulted in R_{max} = 108 μm μCB.

Fig. 3-3 depicts the result of administering 200 ng · mL^{-1} Pertussis Toxin to broadly interfere with GPCRs by catalyzing ADP-ribosylation on the α subunit of the G Protein[81]. Similarly, we find the Ca^{2+} signalling response initiated by μTsunamis was reduced by 87%. Again, chemical induction of the cascade by ATP was not changed significantly where 79% and 87.2% of HUVECs Ca^{2+} signalled when either poison or no toxin was applied culminating in a reduction by 9.2%.

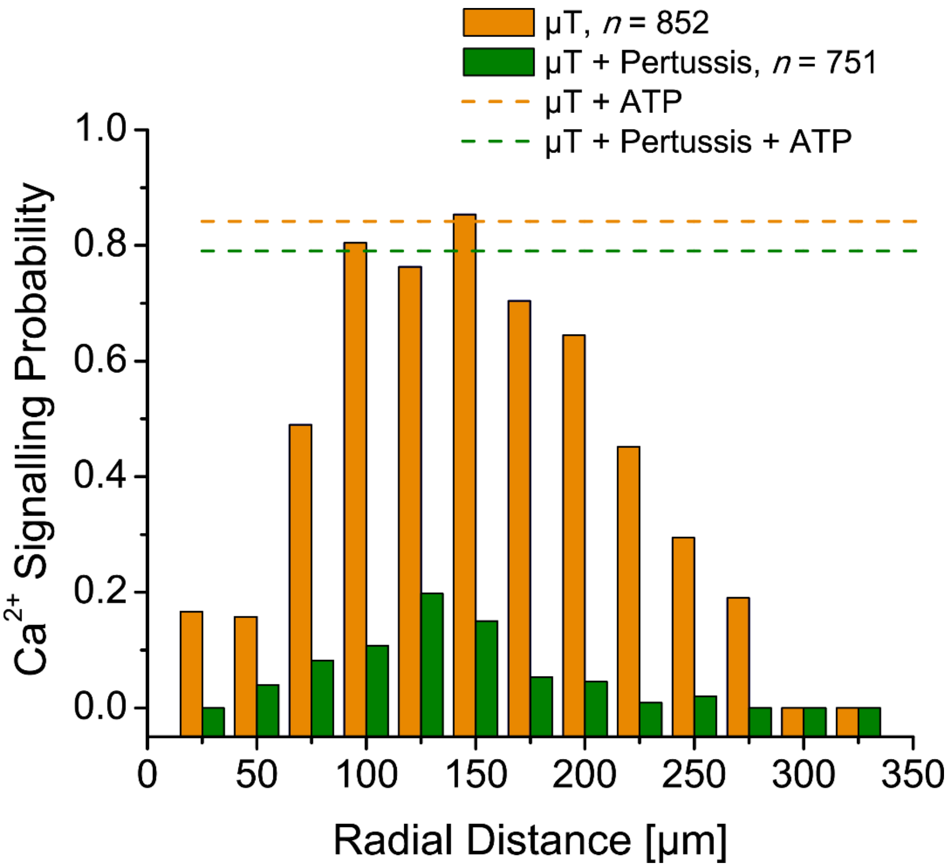

Fig. 3-3 | Probability of Ca^{2+} signalling in HUVECs via μTsunamis and exogenous ATP administration with or without pertussis toxin presence. Solid bars represent Ca^{2+} signalling probabilities from μTsunami stimulation with n being the number of cells analyzed. Dotted horizontal lines correspond to probabilities of calcium signalling by administering ATP following μTsunami exposure with and without pertussis toxin inhibition. μTsunamis were created from a E_p = 5 μJ laser pulse which resulted in R_{max} = 108 μm μCB.

Moreover, we administered 100 μM Suramin to broadly inhibit GPCRs by uncoupling G Proteins from its receptor[82]. Our results, shown in Fig. 3-4, indicate Ca^{2+} signalling in HUVECs exposed to μTsunamis was inhibited by 95.5%. Yet, the observed cascade by ATP was not significantly altered. HUVECs displayed signalling levels of 87.7% without the addition of inhibitor and 83.3% when poisoned by the blocker. These results in conjunction with the previous 2-APB inhibition data support our hypothesis that calcium signalling initiated by μTsunamis occur along the ssGPCR-PLCβ-IP_3R pathway.

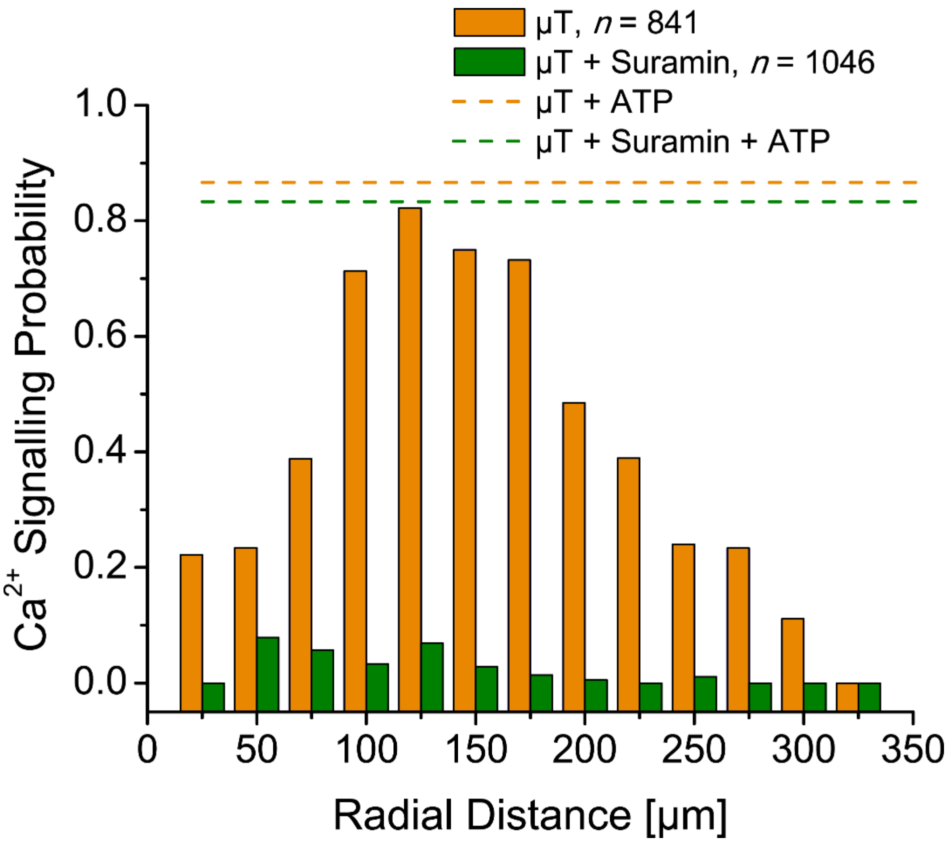

Fig. 3-4 | Probability of Ca^{2+} signalling initiated mechanically by μTsunamis and chemically via exogenous ATP administration for HUVECs either with or without suramin presence. Solid bars indicate calcium signalling probabilities from μTsunami stimulation with n being the number of cells analyzed for blocker or no suramin added. Dotted horizontal lines signify probabilities of Ca^{2+} signalling by administering ATP following μTsunami exposure with and without inhibitor. μTsunamis were generated from a laser pulse of E_p = 5 μJ that resulted in a μCB with R_{max} = 108 μm.

To further support our assertion that μTsunamis are mechanical in nature, we assessed the possibility of modulating the spatial propagation extent of Ca^{2+} signalling in HUVECs by dosing the magnitude of shear stress impulse exposure. Tuning laser pulse energy which creates varying sized μCBs enables generating a range of impulses differing in severity. HUVECs were dosed mechanically with μTsunami induced shear stress impulses ranging in severity by utilizing pulse energies of 2-9 μJ which correlates to maximum μCB radii from 70 to 136 μm. Our results are displayed in Fig. 3-5 where we discovered the spatial extent of Ca^{2+} signalling probability or propagation, ranging from 200 to 500 μm radially, has a dependency on the degree of impulse severity.

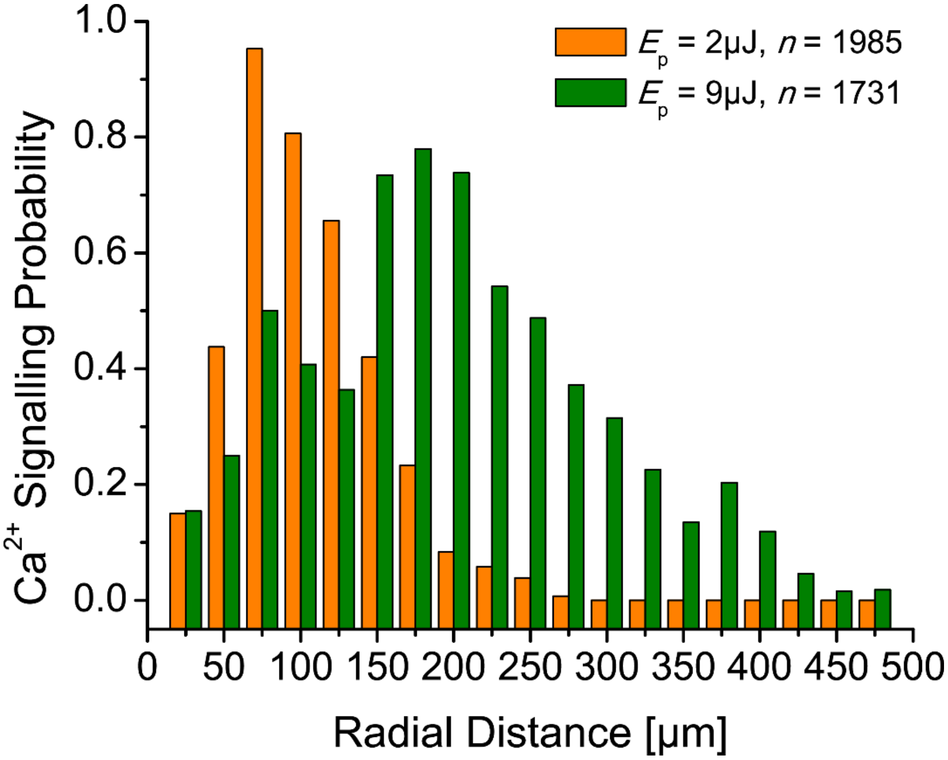

Fig. 3-5 | μTsunami initiated Ca^{2+} signalling probabilities in HUVECs dosed mechanically. HUVECs were mechanically dosed with μTsunamis produced by pulse energies of 2 and 9 μJ which demonstrated the increased range in spatial propagation of the calcium signalling response.

Fig. 3-6 portrays our findings following consolidation of the data across pulse energies where probability of calcium signalling falls under a single 'universal' curve when plotted against impulse. Together, these results support the mechanistic nature of μTsunami initiated Ca^{2+} signalling in HUVECs from exposure to shear stress impulses.

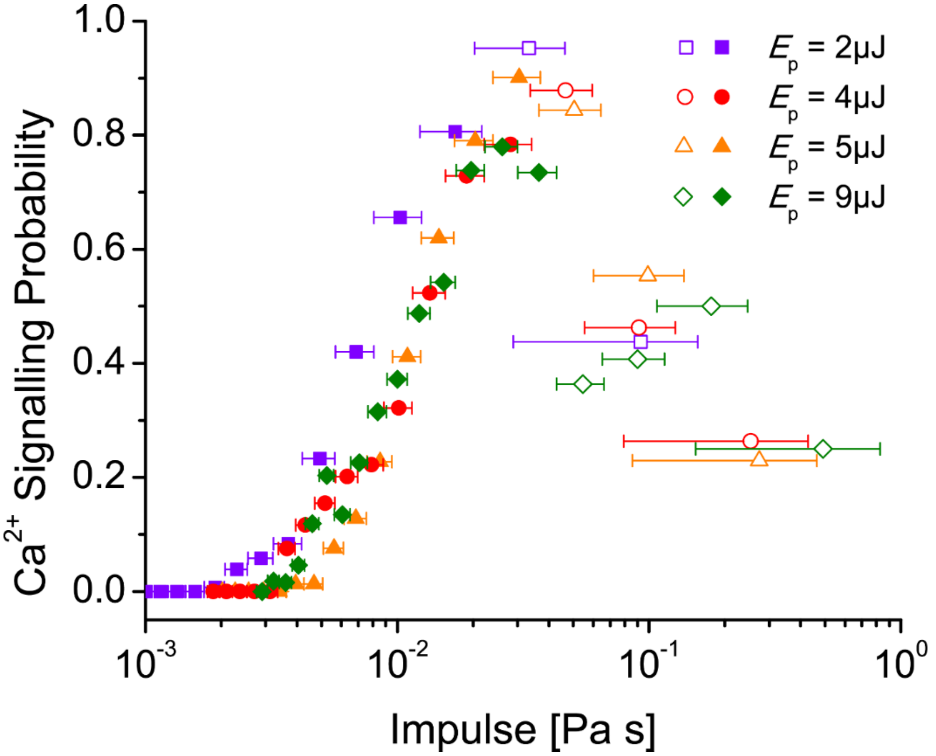

Fig. 3-6 | Universal mechanical dose-response curve. μTsunami initiated calcium signalling probabilities overlap when plotted against impulse across laser pulse energies ranging from 2-9 μJ. This indicates the dependency of Ca^{2+} signalling probability with the μTsunami generated shear stress impulses. The open symbols indicate cells situated within the μCB maximum radius whereas closed symbols correspond to locations beyond the maximum radius of the μCB.

3.4 Conclusion

Collectively, our reported data supports the hypothesis that Ca^{2+} signalling initiated in HUVECs was due to mechanical stimulation of ssGPCRs via μTsunami generated shear stress impulses and not dictated by chemical activation of purinergics. This was determined by conducting appropriate control and inhibition studies along the GPCR / PLCβ / PIP$_2$ / IP$_3$ pathway where we administered antagonists of key molecular intermediates involved in the calcium cascade. Although purinergic receptors were inhibited, we discovered that ATP was still capable of inducing Ca^{2+} signalling and led us to question purinergic involvement. Antagonizing proteins along the IP$_3$ pathway, specifically GPCRs and PLCβ, established the suppression of μTsunami initiated Ca^{2+} mechanosignalling. Moreover, we demonstrated that μTsunamis are mechanical in nature upon discovering the probability and spatial extent of calcium signalling in HUVECs is governed by the magnitude of shear stress impulse exposure.

Chapter 4

Pulsed Laser Microbeam Induced Cavitation Measurement of Elastic Moduli within Hydrogels

4.1 Introduction

The previous chapter established that the initiation of cellular signalling using µTsunamis is due to the application of impulsive mechanical stimuli and further identified the underlying molecular proteins associated with the observed of intracellular Ca^{2+} mechanosignalling in HUVECs. In our previous experiments, HUVECs were grown in a 2D confluent monolayer configuration which is a represents a context that differs from many *in vivo* situations and demonstrates the importance of transitioning into 3D culture systems[83-86]. In 3D culture, cells are embedded in soft materials derived either naturally or synthetically and fabricated into viscoelastic hydrogels to mimic their endemic habitat *in vivo*. Moreover, there is extensive evidence that cell function and phenotype are dynamically influenced by its mechanical microenvironment and the capacity of cells to dynamically modify local mechanical properties of the extracellular matrix in which they reside[87-90]. This not only establishes the motivation to investigate mechanobiology in 3D contexts, but also to characterize the mechanical properties of the scaffold material in which cells are cultured in. In this chapter we present a technique for assessing viscoelastic material properties and providing mechanical perturbation to cells cultured in 3D.

In a 3D context, investigating pericellular stiffness[91] and mechanotransduction requires a method with the ability to access the interior of the 3D viscoelastic material, such as hydrogels, within which the cells reside to either interrogate material properties or deliver mechanical stimulation. Several techniques are frequently employed for mechanical characterization of soft materials including rheometry[92], atomic force microscopy[93] (AFM), and optical[94] or magnetic[95] traps. Rheometers and AFM enable deducing viscoelastic characteristics in bulk at the macroscale level and on the surface at the nanoscale level, respectively, but are unable to apply mechanical perturbation to the interior of a material. Optical and magnetic traps on the other hand are capable of probing the internal properties of soft matter at the microscale level, but require the introduction of exogenous particles. The approach in which we term Laser-Induced Cavitation Rheology (LICR) presented here represents a non-invasive technique for determination of the interior elastic moduli of soft materials without the need for the introduction of exogenous particles. Given that we utilize laser microbeam generated cavitation bubbles for probing soft materials, such measures of elastic moduli are specific to microscopic and mesoscopic spatial scales at high strain-rates. Moreover, the capability of delivering mechanical stimulation to cells cultivated within 3D scaffolds opens new avenues for the pursuit of mechanobiological studies in 3D tissues.

4.2 Approach and Background

Laser-Induced Cavitation Rheology Platform

Our objective is to translate the µTsunami approach introduced in Chapters 2 & 3 for 2D confluent cell monoloayers into a physiologically relevant 3D context. The LICR approach presented here for mechanically measuring the properties of soft matter including hydrogels non-invasively is comprised of three elements: (1) deformation of the material using a single pulsed laser induced microcavitation bubble, (2) determination of the cavitation bubble dynamics using time-resolved photography with automated image analysis, and (3) extraction of the elastic modulus by comparing the experimentally measured cavitation bubble dynamics with that predicted by a numerical model of bubble dynamics within a viscoelastic material with non-linear elasticity through the utilization of a non-linear least squares optimization algorithm.

By focusing pulsed laser microbeam irradiation, cavitation bubbles are produced within the interior of hydrogels which impart finite strains or deformations in the material. We theorized that the cavitation dynamics are influenced by the viscoelastic properties of the material. The frequency, magnitude, and spatial coverage of the strains imparted by the cavitation bubble within soft materials are modifiable by adjusting laser pulse energy. Using this approach, we examined the properties of fibrin and polyethylene glycol (600) diacrylate (PEG (600) DA) gels. Fibrin gels at concentrations of 2.5 and 10 mg · mL^{-1} were tested using pulse energies of 12 and 18 µJ while 6% and 7% PEG (600) DA hydrogels were examined utilizing pulse energies of 2, 5, and 12 µJ. Moreover, we investigate the potential of this approach to initiate Ca^{2+} mechanosignalling in HUVECs embedded within 2.5 mg · mL^{-1} fibrin gels.

Viscoelastic Bubble Dynamics Modelling

Following the measurement of cavitation dynamics experimentally by time-resolved imaging, we utilized predictions from a non-linear viscoelastic bubble dynamics model for fitting our empirical data to determine soft material properties[96]. This model assumes incompressibility while accounting for the effects of viscosity, surface tension, and elasticity of the medium on bubble dynamics. In spherical coordinates, we consider vapor content within the cavity is constant and irrotational flow whereas heat as well as mass transfer across the bubble wall are neglected. The equation that describes bubble dynamics in viscoelastic materials is given by:

$$R_B\ddot{R}_B + \frac{3}{2}\dot{R}_B^2 = \frac{p_B - p_\infty}{\rho_\infty} - \frac{4\nu_l}{R_B}\dot{R}_B - \frac{2S}{\rho_\infty R_B} - \frac{E}{\rho_\infty}$$

where R_B represents the bubble wall radius, $\dot{R}_B$ the bubble wall velocity, $\ddot{R}_B$ the bubble wall acceleration, p_B the pressure within the bubble, p_∞ = 101325 Pa the fluid pressure far away from the bubble or hydrostatic pressure, ρ_∞ = 997 kg · m^{-3} denotes liquid density at an infinite distance from the bubble, ν_l = μ_l · $\rho_\infty$$^{-1}$ symbolizes the fluid kinematic viscosity with liquid viscosity μ_l = 0.894 × 10^{-3} kg · m^{-1} · s^{-1}, S = 0.072 N · m^{-1} the surface tension, and E which is elasticity of the material. p_B is formulated by:

$$p_B = p_v \left(\frac{R_o}{R_B}\right)^{3\kappa}$$

where p_v = 3169 Pa corresponds to the vapor pressure inside the bubble, R_o signifies the equilibrium bubble radius, and κ = 4/3 is a polytropic constant. R_o is equated as:

$$R_o = \sqrt[3]{{R_{max}}^3 \frac{p_v}{p_\infty}}$$

with R_{max} being the maximum bubble radius. All parameter values listed here are for water at 25°C.

Integrating Material Elasticity and Failure

To model elasticity of the material, we substitute a neo-hookean hyperelastic constitutive equation into the E term. Material failure is accounted for by introducing variations of this constitutive model derived from a stress-strain relationship[97] depicted in Fig. 4-1.

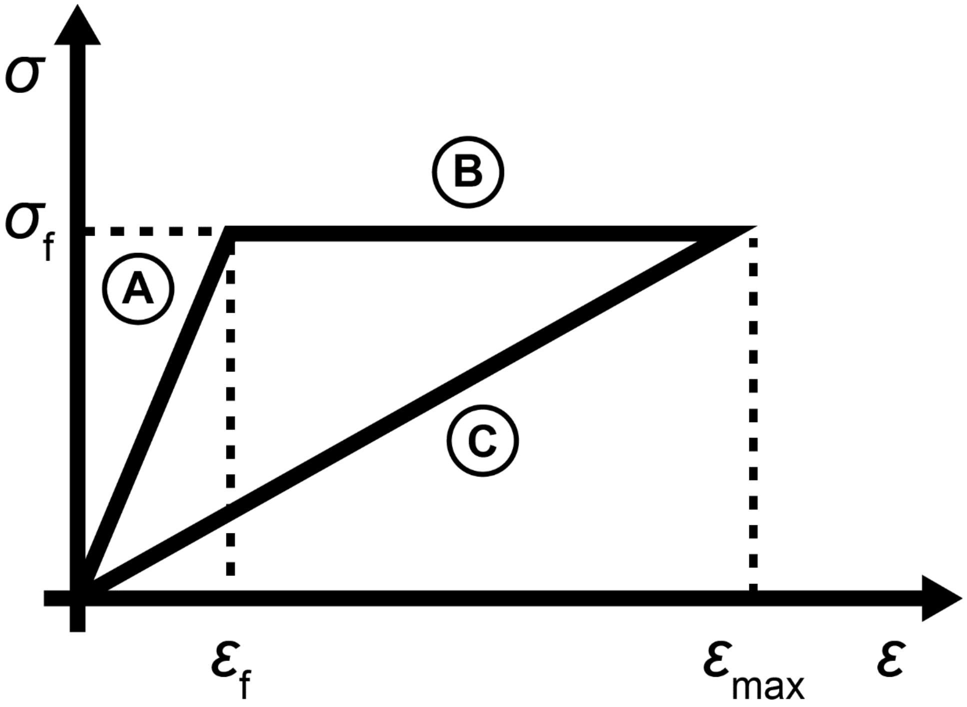

Fig. 4-1 **|** Stress-strain curve modelling viscoelastic material failure. The letters correspond to behavior of the material under deformation where: A. Linear Elastic, B. Plastic Deformation, and C. Recovery. Adapted from [97].

For the expanding bubble when the material has yet to fail denoted as A in the figure, we implement a linear elastic variation described by:

$$E_L = \frac{\eta}{2}\left[5 - 4\left(\frac{R_o}{R_B}\right) - \left(\frac{R_o}{R_B}\right)^4\right]$$

where η is the elastic modulus which represents stiffness of the material. Upon reaching a critical cavitation bubble radius or strain the material ruptures indicated as B in the stress-strain curve, we transition to the plastic deformation version given by:

$$E_f = \frac{\eta}{2}\left[5 - 4\left(\frac{R_o}{R_f}\right) - \left(\frac{R_o}{R_f}\right)^4\right]$$

where R_f represents the bubble radius at which the material fails. At the peak radius of the bubble or strain and during the collapse which is C in the figure, the viscoelastic bubble model is numerically evaluated with the recovery variation formulated as:

$$E_R = \frac{E_f\left[5 - 4\left(\frac{R_o}{R_B}\right) - \left(\frac{R_o}{R_B}\right)^4\right]}{\left[5 - 4\left(\frac{R_o}{R_{max}}\right) - \left(\frac{R_o}{R_{max}}\right)^4\right]}$$

Switching between these constitutive variations entails comparing the strain at the bubble wall ε_{bw} and the material failure strain ε_f. The bubble wall strain is equated as:

$$\varepsilon_{bw} = -\frac{1}{2}\left[\left(\frac{R_o}{R_{max}}\right)^4 - 1\right]$$

When $\varepsilon_{bw} < \varepsilon_f$, the linear elastic variation is introduced into the E term. The plastic deformation version is implemented for $\varepsilon_{bw} > \varepsilon_f$. The recovery term E_R is substituted upon reaching ε_{max} and for all times thereafter.

Recovery of Elastic Moduli in Soft Viscoelastic Materials

Mechanical properties of soft viscoelastic materials are recovered by determining the parameters that enable a ‘best fit’, in a least squares sense, between the experimental data and predictions provided by our cavitation bubble dynamics models. These parameters are determined by implementing a standard non-linear least squares optimization algorithm. The protocol involves the specification of initial values (guesses) to fit for R_{max}, η, and ε_f which are parameters in the viscoelastic bubble model. Specifically, the elastic modulus η and failure strain ε_f represent the material properties that we wish to determine. The theoretical cavitation dynamics are numerically computed by our fitting program at the time points corresponding to the experimental data measured by time-resolved photography. We determine the χ^2 or least squared difference between the theoretical model results and the experimental data. This process is repeated to optimize for a set of parameter values that results in the minimum achievable error.

Finite Strain Field Computation

Cavitation formed in the hydrogel interior deforms the material during expansion. These deformations within the material are described by radial and circumferential strains imparted by the bubble. We can determine the strain field, which describes an associated quantity of strain at specific points in the material, via computation for a single cavitation bubble surrounded in an infinite, homogeneous, isotropic, and incompressible medium. By adhering to standard continuum mechanics formalism, a Lagrangian spherical coordinate system is defined where the origin is at the center of the bubble. The bubble wall and surrounding material points begin in an unstrained or initial configuration with radius R_o and r_o, respectively, at time t = 0. At any time thereafter, the surrounding material points are displaced by cavitation expansion. In this deformed configuration, radial locations of the surrounding material coordinates as well as the bubble wall radius are designated as $r(r_o, t)$ and $R_B(R_o, t)$. Fig. 4-2 depicts a schematic of the model problem setup which describes radial displacement of material points from the initial configuration into the deformed state.

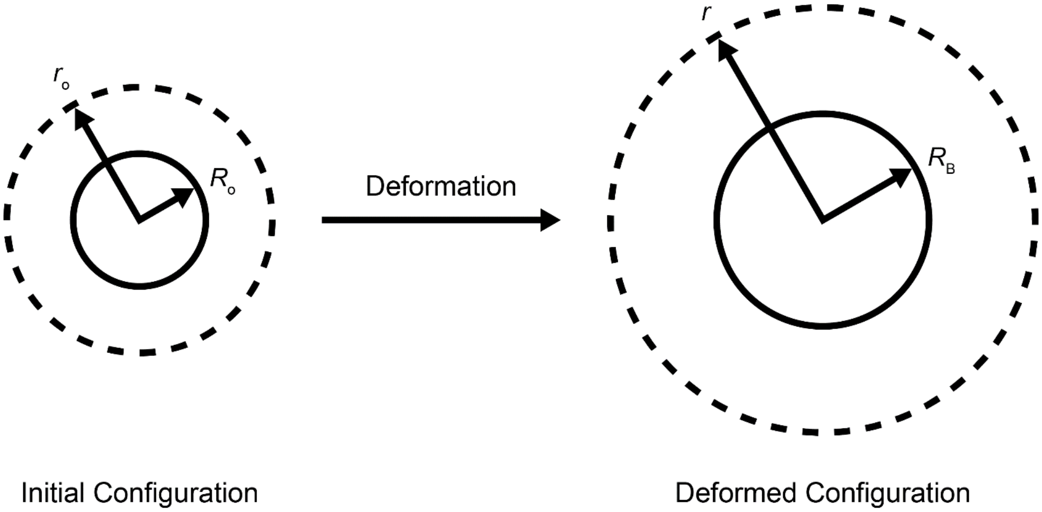

Fig. 4-2 | Model problem setup for displacement of material coordinates by an expanding bubble from the initial state into the deformed configuration.

Displacement for any material point is expressed by:

$$u(r_o, t) = b(t) + r(r_o, t) - r_o$$

where $b(t)$ signifies the rigid body translation vector which is 0 for the case of an expanding bubble. The deformation gradient tensor is given by:

$$F = \begin{bmatrix} \frac{dr}{dr_o} & 0 & 0 \\ 0 & \frac{r}{r_o} & 0 \\ 0 & 0 & \frac{r}{r_o} \end{bmatrix}$$

We derived an expression to relate $r(r_o, t)$ in the deformed configuration to r_o in the initial unstrained state by solving the incompressibility condition $\det(F) = 1$:

$$\left(\frac{dr}{dr_o}\right)\left(\frac{r}{r_o}\right)^2 = 1 \rightarrow r(r_o, t) = \sqrt[3]{{r_o}^3 - {R_o}^3 + {R_B}^3}$$

Following finite deformation theory, the Almansi strain tensor is defined as:

$$\varepsilon = \frac{1}{2}(I - c)$$

where $c = F^{-T}F^{-1}$ is the Cauchy deformation tensor.

4.3 Materials and Methods

Hydrogel Fabrication

Fibrinogen from human plasma (F3879, Sigma) was dissolved in Hank's Balanced Salt Solution without the addition of either Ca^{2+} or Mg^{2+} ions (HBSS-) and phenol red (14175-095, Gibco) in a 37°C water bath for an hour. The fibrinogen solution was then sterilized using a 0.2 µm PES syringe filter. Polymerization into fibrin hydrogels was initiated following the administration of 1 U · mL^{-1} thrombin from human plasma (T7009, Sigma) into the fibrinogen solution. Fibrin hydrogels were incubated at room temperature for 5 minutes, transferred to a 37°C incubator for 25 minutes, hydrated with HBSS-, and incubated at 37°C for an additional 2 hours to ensure full polymerization. Polyethylene glycol (600) diacrylate (Sartomer) was diluted in HBSS- buffer and 0.5% by volume of Darocur 1173 (Ciba) which is a free radical photoinitiator. PEG (600) DA hydrogels were cured by exposing to UV (OmniCure S1000, EXFO) for 45 seconds.

Time-Resolved Cavitation Imaging Setup

The µTsunami platform and time-resolved imaging setup were utilized to determine cavitation dynamics in the hydrogel interior. Cavitation was produced by pulsed laser microbeam irradiation using 500 ps duration pulses at λ = 532 nm emitted from a Q-switched pulsed microchip laser (PNG-M03012, Teem Photonics). We utilized a diverging lens as well as a converging optic with focal length *f* of -25 mm and 500 mm for expanding and collimating the laser microbeam, respectively. Pulse energy was adjusted via λ/2 wave-plate and polarizing beamsplitter. An iris cropped the outer laser beam edge for allowing only the central portion to enter the right port of an inverted microscope (IX-81, Olympus). The laser was directed by a dichroic mirror (ZT532NBDC, Chroma) to the rear aperture of a 20x 0.45 NA objective (LUCPlanFLN, Olympus) which focused the microbeam in the hydrogel. Cavitation dynamics were determined using an ultra-fast intensified gated charge-coupled device (ICCD) camera (4-Picos, Stanford Computer Optics). Fluorescence emission from a dye cell (LDS 698, Exciton) pumped by a separate λ = 532 nm frequency-doubled Q-switched Nd:YAG laser (Brilliant B, Quantel) provided imaging illumination. Illumination from the dye cell was collected and directed to the microscope condenser via fiber optic. Timing for the delivery of the cavitation producing laser pulse, image illumination, and camera gate were controlled with a delay generator (BNC Model 575, Berkeley Nucleonics Corporation). Electronic signals were examined on an oscilloscope (WaveRunner 6051A, LeCroy) for synchronizing the camera gate and illumination relative to the cavitation inducing laser.

Cavitation bubbles were generated at a height of 550 µm and 10 µm above the glass surface for fibrin and PEG (600) DA hydrogels, respectively. A single full bubble oscillation cycle comprising the formation, expansion, and collapse was characterized in all hydrogel experiments where at least 5 data points were recorded per delay time in 1 µs increments.

Cavitation Bubble Dynamics Measurement

Determining the time evolution of the cavitation bubble radius was automated with a MATLAB script. All images were read into MATLAB as a matrix of intensities and segmented using k-means clustering with 2 classes. Cavitation was assumed to be symmetric in all cases where we calculated an equivalent radius from the segmented pixel area. Refer to Appendix B1 for the software.

Non-Linear Least Squares Optimization

We implemented the viscoelastic cavitation model incorporated with material failure into a standard non-linear least squares fitting algorithm by writing a script in MATLAB for determination of the elastic modulus and failure stain of the fibrin and PEG (600) DA hydrogels when subjected to laser microbeam cavitation bubble stimulation. Refer to Appendix B2 for the actual program code.

Finite Strain Field Computation

The finite deformation model to compute the strain field was implemented by coding in MATLAB. Refer to Appendix B3 for the code.

Hydrogel Rheology

Rheological measurements were carried out using stress controlled rheometers. Fibrin gel rheology was performed on a MCR-301 (Anton Paar). Rheology of PEG (600) DA hydrogels were conducted on a DHR-3 (TA Instruments) equipped with a borosilicate glass stage for curing. A 25 mm sand blasted parallel plate geometry was used for all tests at room temperature. Hydrogel samples were polymerized between the parallel plate geometry and rheometer stage following addition of their respective initiators. Frequency sweeps ranging from 0.01–100 Hz were carried out with amplitude set at 1% strain. Amplitude sweeps ranging from 0.01–1000% strain were accomplished with frequency set to 1 Hz.

3D Cell Culture

Fibrinogen from human plasma (F3879, Sigma) was dissolved in EGM-2 without fetal bovine serum (FBS). Following sterilization by a 0.2 µm PES syringe filter, primary HUVECs (generously provided by Prof. Chris Hughes; University of California, Irvine) at passage 4 were resuspended in the fibrinogen solution. Polymerization into cellularized fibrin gels was initiated following administration of the fibrinogen-cell solution combined now with 2% FBS into a 35 mm #1.5 glass-bottomed dish (FluoroDish, WPI) blotted with 1 U · mL^{-1} thrombin from human plasma (T7009, Sigma). HUVEC embedded fibrin hydrogels were incubated at room temperature for 5 minutes, incubated at 37°C as well as 5% CO_2 for 25 minutes, and hydrated using EGM-2 with 2% FBS.

Dye Loading and Imaging

Prior to indicator loading, HUVECs cultured in fibrin gels were washed thrice using Hank's Balanced Salt Solution with Ca^{2+} as well as Mg^{2+} ions (HBSS+) and no phenol red (14025-092, Gibco). Fluo-3/AM (F-1242, Molecular Probes), a fluorescent dye that increases emission upon binding to intracellular calcium, was dissolved in 20 mM HEPES (15630-080, Gibco) buffered HBSS+ (HHBSS+) supplemented with 2 $g{\cdot}L^{-1}$ D-(+)-glucose (G7021, Sigma) and 0.5% DMSO (276855, Sigma) as the probe vehicle. HUVECs embedded within fibrin hydrogels were incubated in 5 µM Fluo-3/AM for an hour at 37°C and 5% CO_2. The enclosed cells were rinsed thrice with HBSS+ following dye loading and incubated in EGM-2 for 30 min at 37°C and 5% CO_2. Before experimentation, HUVEC-fibrin gels were cleansed thrice using Hank's Balanced Salt Solution with neither Ca^{2+} nor Mg^{2+} ions (HBSS-) and without phenol red (14175-095, Gibco). During the imaging experiment, HUVECs were kept on Ca^{2+}-free 20 mM HEPES buffered HBSS- (HHBSS-) supplemented with Mg^{2+} ions, 2 $g{\cdot}L^{-1}$ D-(+)-glucose, and 3 mM EGTA to chelate any remaining traces of extracellular calcium[67].

A time-series of the Ca^{2+} signalling response was acquired over 100 s in intervals of 1 s with the cavitation bubble delivered following the 5 s mark. Delivery of cavitation bubbles to HUVECs embedded in fibrin gels and Ca^{2+} imaging were performed at room temperature.

4.4 Results and Discussion

Cavitation bubble cycles formed within fibrin and polyethylene glycol (600) diacrylate (PEG (600) DA) hydrogels captured from time-resolved photography are depicted in Fig. 4-3a and Fig. 4-3b, respectively. A single full bubble oscillation constituting the formation, expansion, and collapse produced in both hydrogel material types occurred within tens of microseconds. This timescale translates to a frequency of approximately 10^5 Hz and establishes the inertia dominated dynamics of cavitation bubbles perturb soft materials at high strain-rates. Bubble duration and size are readily altered by adjusting laser pulse energy to enable delivery of variable strain-rates. The application of specifically tailored strain-rates renders the ability to mechanically characterize materials of viscoelastic nature at various frequencies and provide differential stimuli to 3D cultures mechanically.

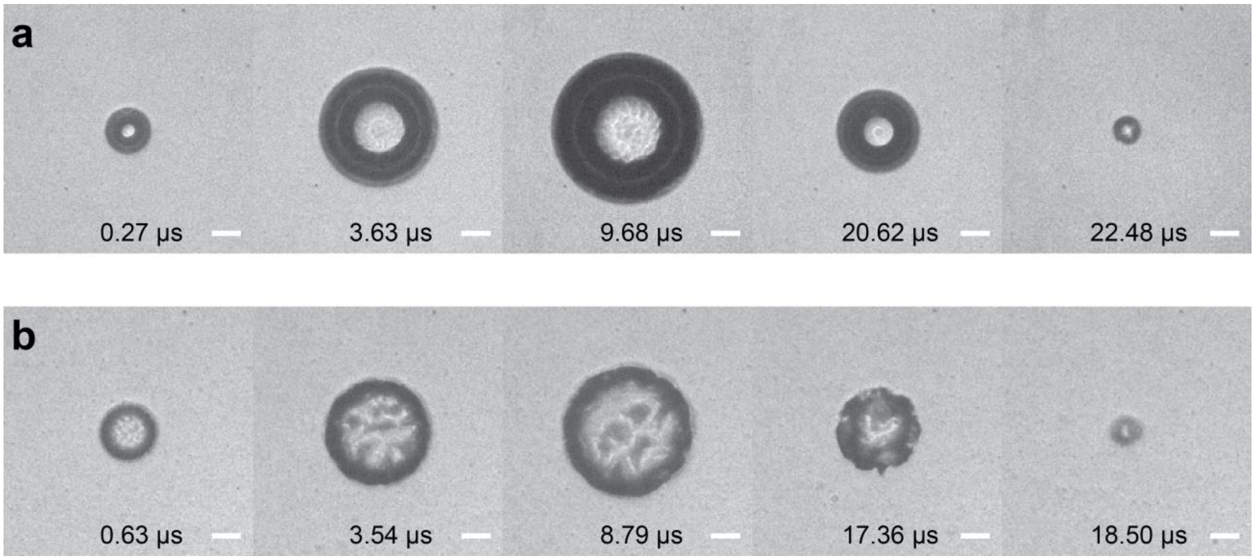

Fig. 4-3 | Cavitation bubble cycle captured by time-resolved photography within hydrogel. **a**, Images of cavitation produced at separate time points within 2.5 mg · mL^{-1} fibrin gels by a E_p = 12 μJ laser pulse with R_{max} = 126.20 μm. **b**, Cavitation bubbles characterized at various time points inside 6% PEG (600) DA hydrogels from a E_p = 5 μJ laser pulse with R_{max} = 112.17 μm. Scale bar = 50 μm.

In Fig. 4-4, we graph the bubble dynamics captured within 2.5 and 10.0 mg · mL^{-1} fibrin gels. The dynamics were measured for cavitation generated from laser pulse energies of 12 and 18 μJ in fibrin gels at both concentrations. It should be noted that each data point was measured from separate bubbles. Since we employ time-resolved photography, this requires acquiring cavitation at various time points and piecing together an entire cycle to determine the bubble dynamics for an entire bubble growth/collapse cycle. As expected, we qualitatively find a decrease in the maximum radius and duration of the bubble cycle oscillation with increasing concentration in fibrin gels for a fixed pulse energy. The reduced bubble cycle oscillation times are apparent when we plot the predictions for the cavitation bubble dynamics in water evaluated from our model in the absence of material elasticity with η = 0. These observations led us to postulate the material fibers in fibrin gels are hindering the dynamics. Interestingly, bubble radii measured from the initial portion of the rise or expansion are quite consistent whereas more variability was discovered during the collapse. We suspected that this variation is due in part to plastic deformation had transpired upon failure of fibrin fibers.

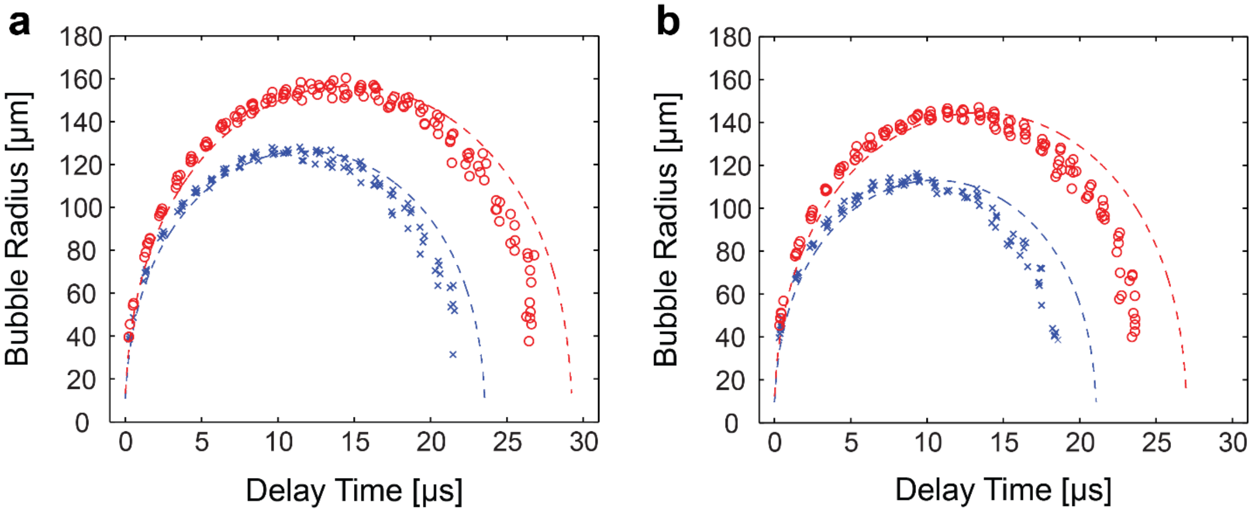

Fig. 4-4 | Cavitation dynamics in fibrin gels. **a**, Bubble dynamics characterized in 2.5 mg · mL^{-1} fibrin gels. **b**, Cavitation dynamics measured in 10.0 mg · mL^{-1} fibrin hydrogels. Red o and blue x symbolize bubble dynamics determined at E_p = 12 μJ and E_p = 18 μJ, respectively. Dashed lines represent cavitation dynamics predicted in water by evaluating the model without elasticity.

Fig. 4-5 portrays bubble dynamics acquired in 6 and 7% PEG (600) DA hydrogels. For both concentrations, we determined the dynamics of bubbles induced by laser pulse energies of 2, 5, and 12 μJ. We observed the cavitation dynamics in PEG (600) DA hydrogels behaved similarly to the dynamics measured in fibrin gels. Moreover, microcracks remaining within PEG (600) DA gels were discovered following the initiation of bubbles, shown in Fig. 4-6, which affirms our hypothesis on material rupture and provided the insight to integrate failure into the viscoelastic bubble model.

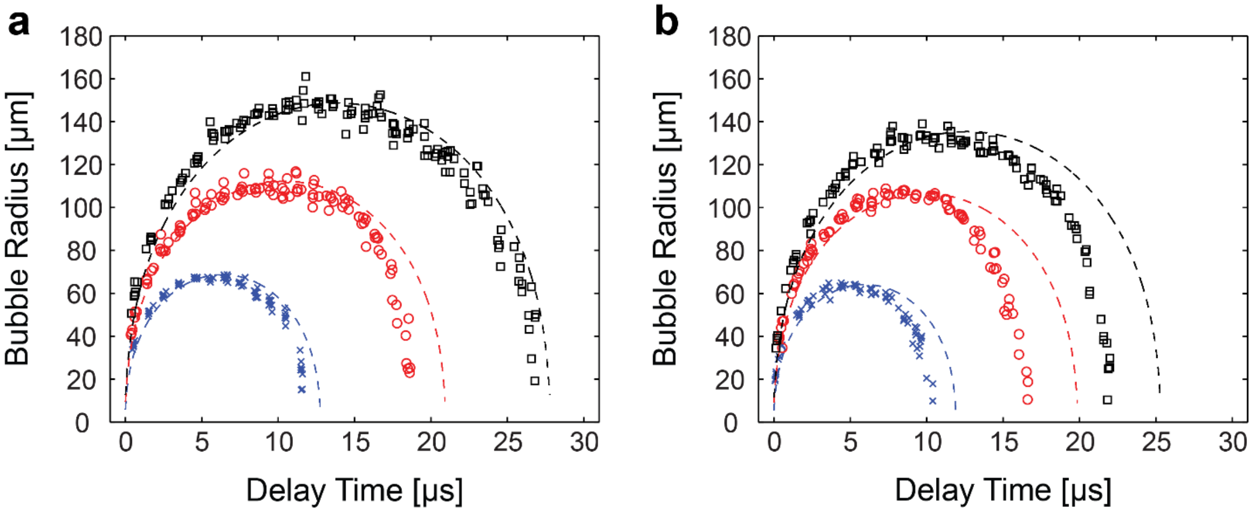

Fig. 4-5 | Bubble dynamics in PEG (600) DA hydrogels. **a**, Cavitation dynamics measured in 6% PEG (600) DA hydrogels. **b**, Bubble dynamics characterized in 7% PEG (600) DA gels. Blue x, red o, and black □ are symbols that represent dynamics determined at E_p = 2 µJ, E_p = 5 µJ, and E_p = 12 µJ. Dashed lines signify predicted bubble dynamics in water by evaluating the model without elasticity.

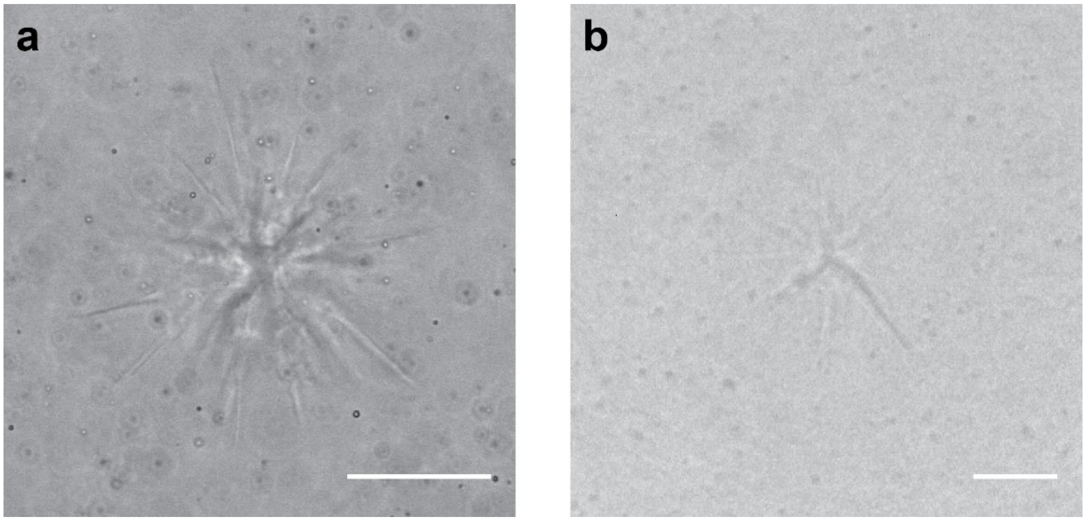

Fig. 4-6 | Microcrack within PEG (600) DA hydrogel. **a**, Phase image of material fracture within a 6% PEG (600) DA gel following single cavitation induction by a 12 µJ laser pulse. **b**, Time-resolved photograph of a microcrack remaining inside a 7% PEG (600) DA gel after cavitation was generated via E_p = 12 µJ laser pulse. Scale Bar = 50 µm.

Table 4-1 lists best fit values inversely extracted from bubble dynamics in fibrin gels with our algorithm by optimizing for the parameters maximum bubble radius R_{max}, elastic modulus η, and failure strain ε_f. The results represent the parameters values in the viscoelastic bubble model that provide predictions for the cavitation bubble dynamics that best fit the experimentally measured data points. As expected, we find that for a fixed pulse energy,

R_{max} diminishes when fibrin gel concentration increased from 2.5 to 10.0 mg/mL. We also observed a rise in η when pulse energy was kept consistent and fibrin gel concentration increased where this stiffening was intuitively anticipated as well. Remarkably, the strain at which fibrin fails remains quite uniform across concentration and pulse energies.

Table 4-1 | Best fits for R_{max}, η, and ε_f in fibrin gels.

Fibrin Gel Concentration	E_p [μJ]	R_{max} [μm]	η [kPa]	ε_f [ ]
2.5 mg · mL^{-1}	12	124.15 ± 2.02	25.28 ± 2.76	0.2063 ± 0.0622
	18	155.21 ± 1.04	23.56 ± 0.66	0.2370 ± 0.0226
10.0 mg · mL^{-1}	12	112.11 ± 1.02	40.63 ± 1.15	0.2426 ± 0.0412
	18	142.27 ± 2.35	37.04 ± 4.35	0.2576 ± 0.0624

The best fits obtained from cavitation dynamics formed in PEG (600) DA hydrogels via our fitting algorithm for R_{max}, η, and ε_f are tabulated in Table 4-2. Analogously, we also find decreased R_{max} with PEG (600) DA concentration increased for unchanging pulse energies. PEG (600) DA gels also stiffened as indicated by greater η values upon increasing material concentration from 6 to 7%. As suggested by the values of ε_f, PEG (600) DA hydrogels are perhaps more resistant to radial stresses from the bubble than fibrin gels with greater material failure strains. Except for two instances, specifically 5 and 12 μJ for 6% PEG (600) DA gels, the strain at which these hydrogels fail were also determined to be fairly consistent. Our results from fitting are indicative of heterogeneity in fibrin and PEG (600) DA hydrogels where we also qualitatively observed in the experimentally measured bubble dynamics data.

Table 4-2 | Best fit values for R_{max}, η, and ε_f in PEG (600) DA hydrogels.

PEG (600) DA Gel Concentration	E_p [µJ]	R_{max} [µm]	η [kPa]	ε_f [ ]
6%	2	67.67 ± 0.83	22.10 ± 0.98	0.3007 ± 0.0642
	5	108.27 ± 4.28	22.79 ± 8.41	0.1884 ± 0.1451
	12	150.67 ± 1.53	26.54 ± 1.61	0.1451 ± 0.0516
7%	2	64.61 ± 0.77	35.86 ± 0.80	0.3187 ± 0.0403
	5	100.67 ± 1.01	28.49 ± 1.87	0.3214 ± 0.0388
	12	132.23 ± 1.57	39.72 ± 2.66	0.2962 ± 0.0287

We evaluated our viscoelastic bubble model using the recovered parameter values to predict theoretical cavitation dynamics and plotted them with the experimental data points for fibrin and PEG (600) DA gels as depicted in Fig. 4-7 and Fig. 4-8, respectively. These graphs establish that the theoretically calculated cavitation dynamics conforms well to the experimentally measured dynamics. This indicates our method is not only able to capture the R_{max} formed within hydrogels, but also deduce the interior stiffness and failure strain of the viscoelastic material.

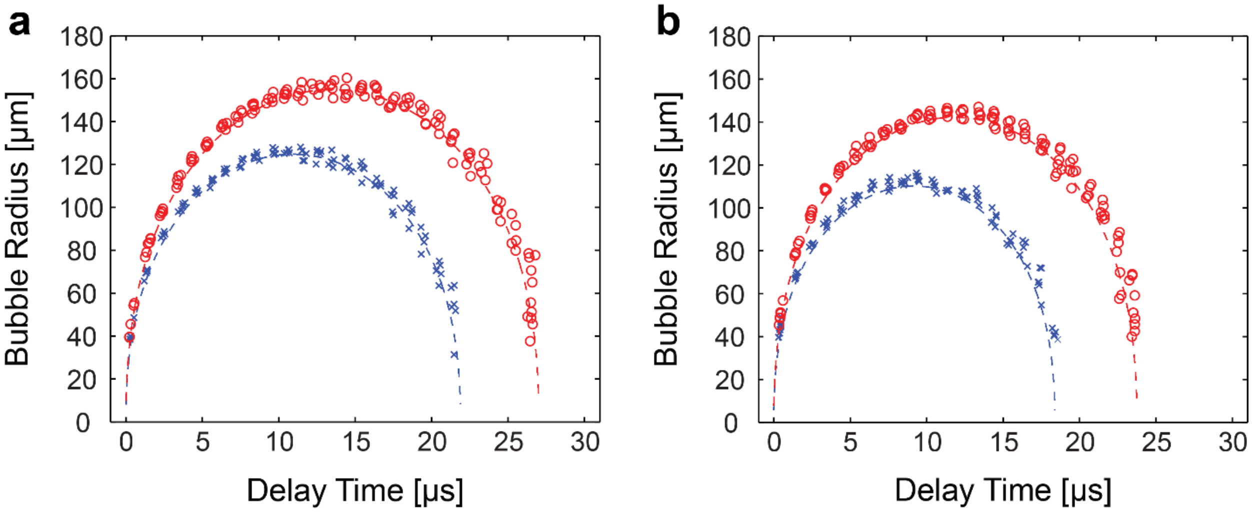

Fig. 4-7 | Conformity between theoretical bubble dynamics evaluated from the best parameter fits and experimental data points in fibrin gels. **a**, The theoretically predicted best fit curve for bubble dynamics plotted with experimentally characterized dynamics in 2.5 mg · mL^{-1} fibrin gels. **b**, Experimental bubble dynamics graphed with the theoretically predicted best fit curve in 10.0 mg · mL^{-1} fibrin hydrogels. Red o and blue x are symbols that correspond to cavitation dynamics determined at E_p = 12 µJ and E_p = 18 µJ, respectively. Dashed lines represent viscoelastic model predictions of cavitation dynamics that best fit the experimental data points.

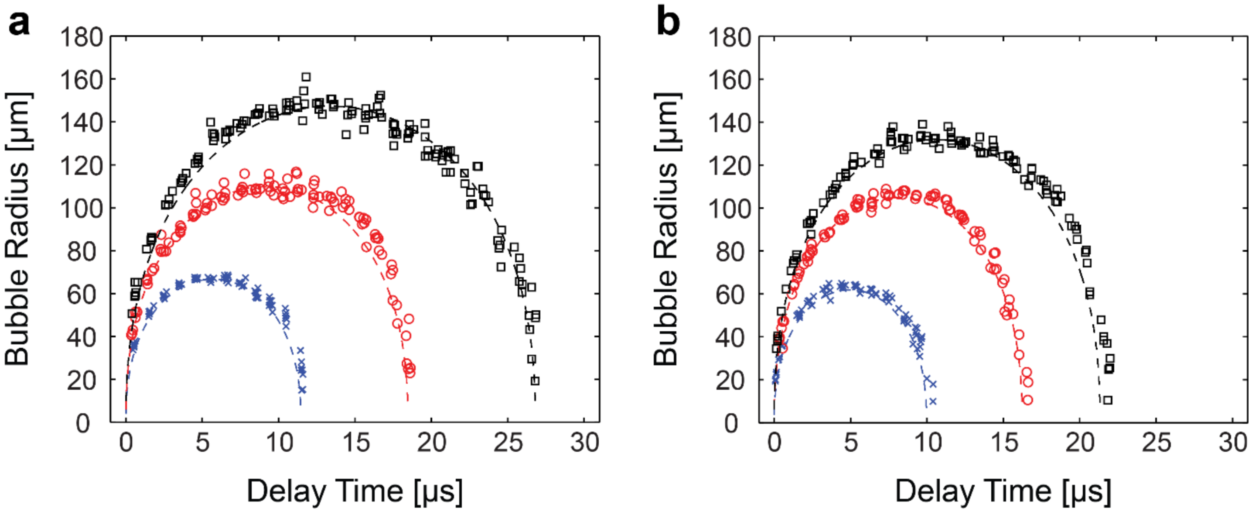

Fig. 4-8 | Agreement of theoretically predicted and experimentally measured cavitation dynamics in PEG (600) DA hydrogels. **a**, Plot of bubble dynamics characterized experimentally with theoretical predictions of the best fit curve for 6% PEG (600) DA gels. **b**, Best fitting curve predicted from the viscoelastic bubble model graphed with the experimental dynamics data points in 7% PEG (600) DA hydrogels. Blue x, red o, and black □ symbolize cavitation dynamics measured at E_p = 2 µJ, E_p = 5 µJ, and E_p = 12 µJ, respectively. Dashed lines signify cavitation dynamics predicted theoretically which best fit the dynamics determined experimentally.

The bulk properties of fibrin and PEG (600) DA gels were determined by rheometry for comparison. We acknowledge the dissimilarity between rheology and our technique (LICR) in quantifying the mechanical properties of materials. Rheometers measure G' which represents the shear modulus and our technique inversely extracts η or the elastic modulus, respectively. Frequency and amplitude sweeps on fibrin gels were conducted via rheometry as illustrated in Fig. 4-9. Although less stiff in shear, we find stiffening of fibrin gels as indicated by greater G' when concentration was increased from 2.5 to 10.0 mg·mL^{-1}. This increase in gel stiffness was also observed in the inversely extracted elastic moduli as well. As indicated in the amplitude sweep, fibrin fails approximately at 200-300% by shear quite consistently across either concentration. Fig. 4-10 depicts sweeps of frequency and amplitude for PEG (600) DA gels. Similarly, we also find that increasing PEG (600) DA concentrations from 6 to 7% led to stiffer hydrogels as indicated by greater values of G'. PEG (600) DA gels were also discovered to rupture fairly consistently near 100% strain in shear. These results demonstrate the limitations of assessing viscoelastic material properties by rheometry which is unable to exceed 100 Hz typically due to hardware and/or software restrictions.

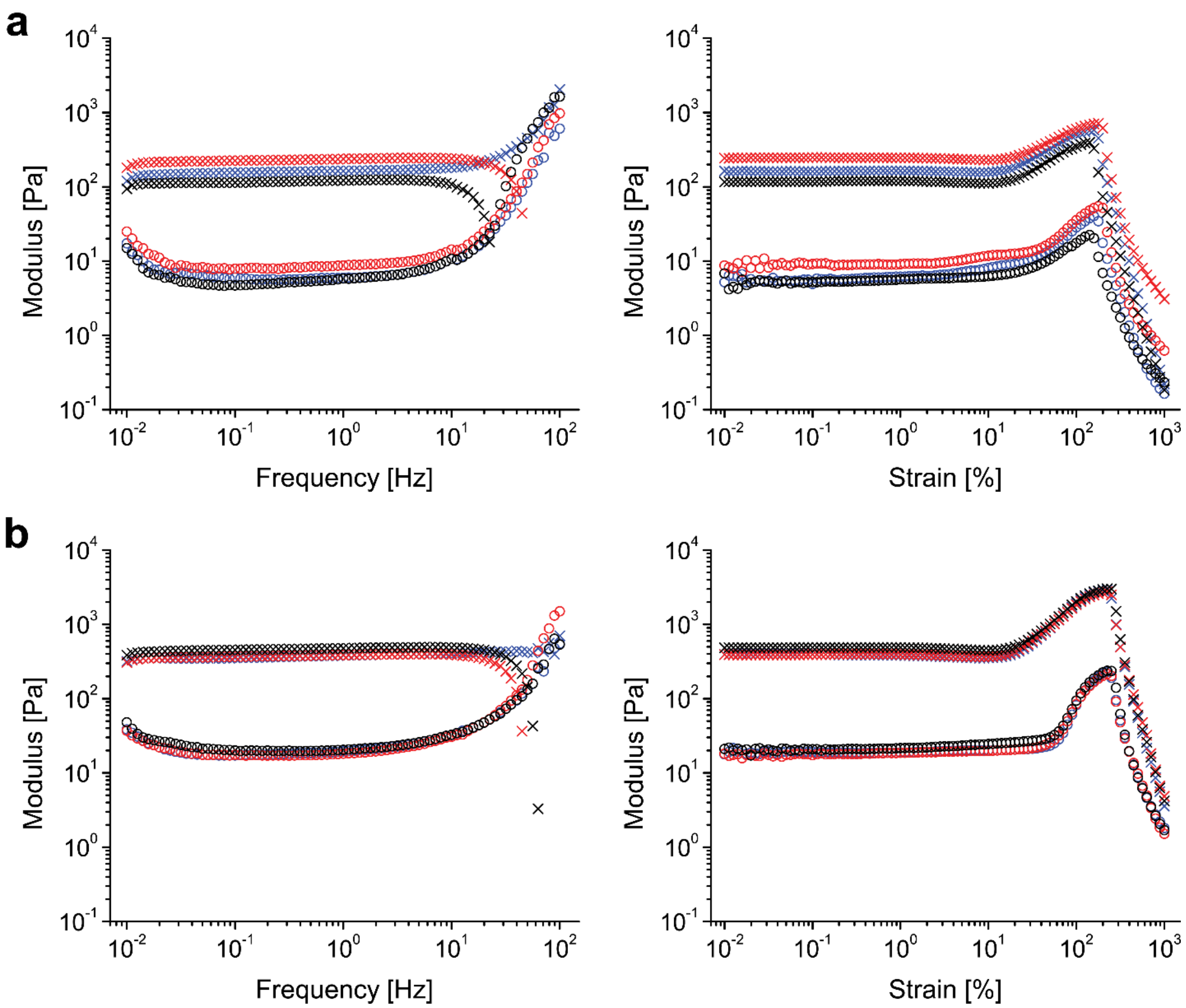

Fig. 4-9 | Frequency and amplitude sweeps for fibrin gels. **a**, 2.5 mg · mL^{-1} fibrin gel. **b**, 10.0 mg · mL^{-1} fibrin hydrogel. The x as well as o symbolize G' and G'' which are storage and loss moduli, respectively. G' corresponds to a stiffness whereas G'' represents the viscosity. Color signifies the rheological tests conducted on separate samples.

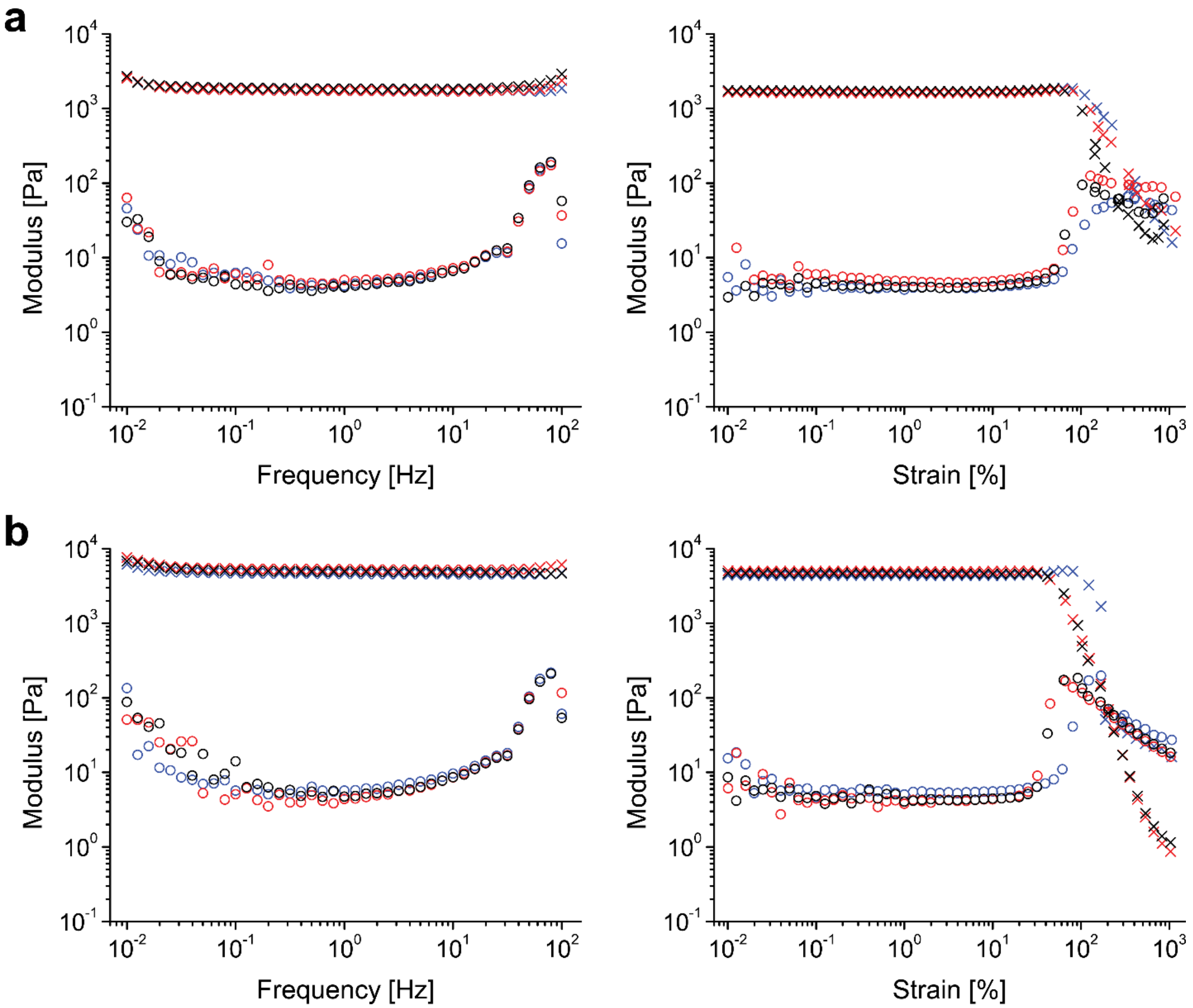

Fig. 4-10 | Frequency and amplitude sweeps for PEG (600) DA hydrogels. **a**, 6% PEG (600) DA hydrogels. **b**, 7% PEG (600) DA gels. The symbols, x and o, denote G' which is the storage moduli as well as G'' the moduli of loss. Color corresponds to the individual samples subjected to rheometry.

Previously, we established the ability of initiating calcium signalling in a confluent monolayer of primary adherent HUVECs stimulated mechanically by µTsunami generated shear stress impulses. HUVECs were cultured in a 2D configuration of non-physiological significance in our previous studies. This led us to test the possibility of providing mechanical stimulation to cells cultured in a 3D context with our method. We present here preliminary evidence of inducing cytosolic Ca^{2+} mechanosignalling in HUVECs embedded in 2.5 mg · mL^{-1} fibrin gels. The Ca^{2+} signalling response is observed in Fig. 4-11, which depicts HUVECs within a fibrin gel before and after stimulation by a cavitation bubble of approximately R_{max} = 80 µm. Instead of impulsive fluid shear stress, we postulated strains imparted by the bubble stimulates ssGPCR which activate the IP_3 pathway and leads to the observed calcium signalling. Fig. 4-12 portrays a plot of radial and circumferential finite strain field imparted by the bubble. The calcium signalling HUVEC enveloping the material point at roughly 93.23 µm from the bubble origin experienced a radial and circumferential strain of -1.27 (tension) and 0.23 (compression), respectively. Our analysis of the strain field enables us to determine a specific quantity of strain that cells experience depending on their location in relation to the material coordinate space.

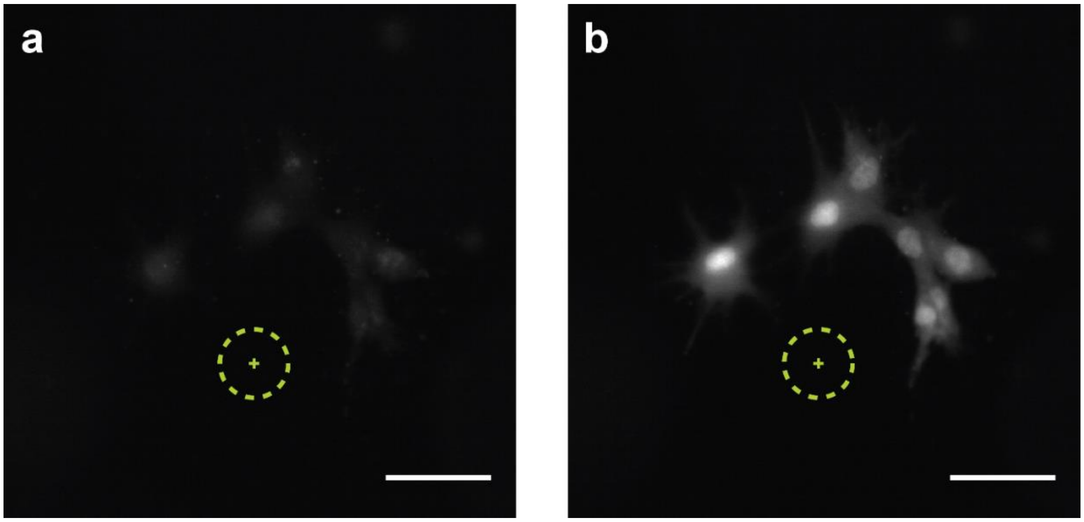

Fig. 4-11 | Initiation of intracellular Ca^{2+} signalling within HUVECs embedded within a 2.5 mg · mL^{-1} fibrin gel. **a**, Fluorescence image of HUVECs cultured in a fibrin gel prior to cavitation delivery where signalling has yet to occur. **b**, Fluorescence image of HUVECs embedded within a fibrin hydrogel following bubble delivery where signalling is indicated by the increased intensity. A cavitation bubble of approximately R_{max} = 80 µm was generated by a E_p = 5 µJ laser pulse delivered to the center region of the dotted ring. The size of this dotted ring does not reflect the actual bubble size. Scale bar = 100 µm.

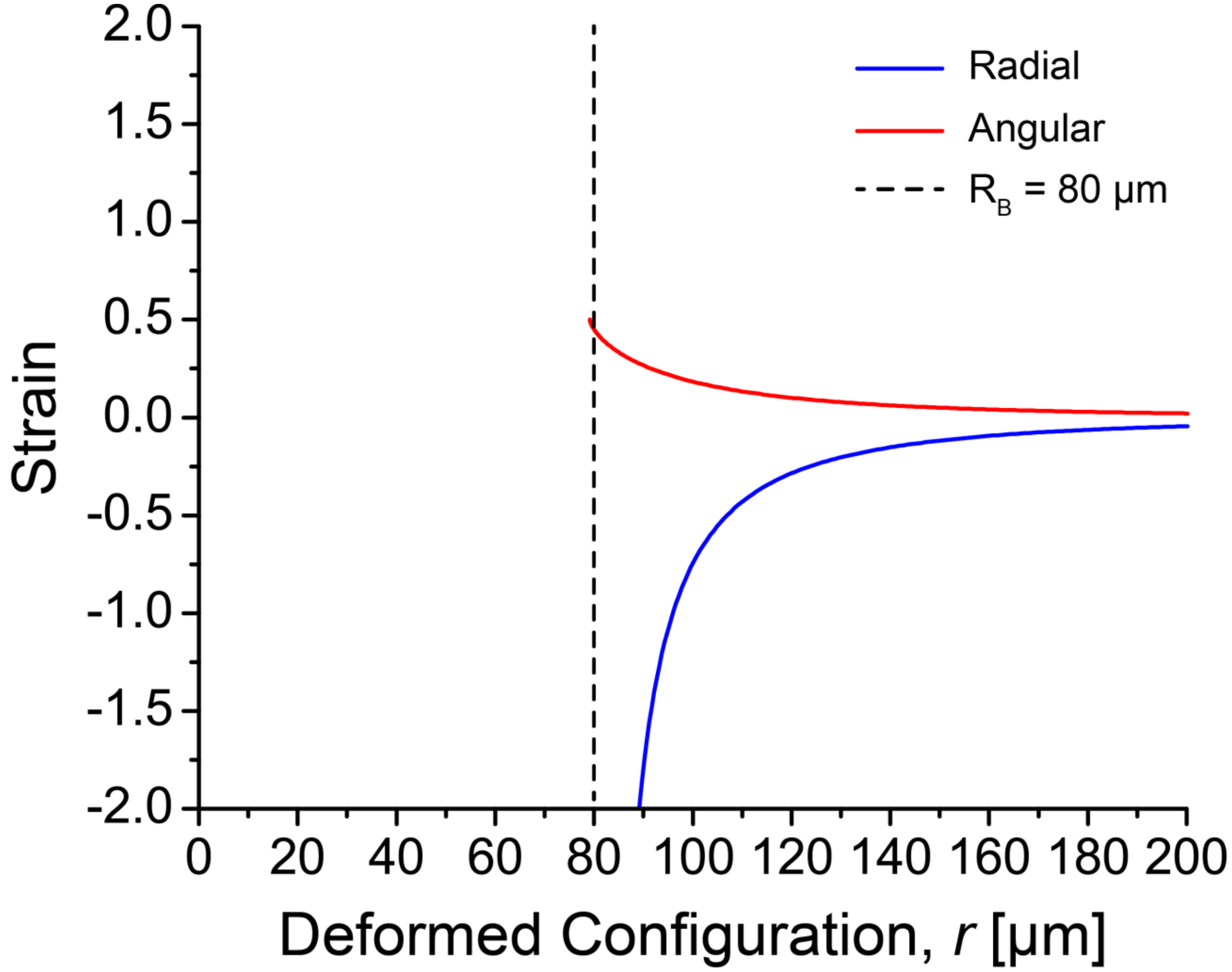

Fig. 4-12 | Strain field imparted by a cavitation bubble of R_{max} = 80 µm plotted for material coordinates in the deformed state. Blue and red curves signify the radial and circumferential strain, respectively. Dashed vertical black line indicates the radial location for deformed material points that correspond to the maximum bubble wall radius.

4.5 Conclusion

Our results establish the LICR platform for the non-invasive measurement of the physical properties of soft viscoelastic hydrogels at high strain-rates. This was achieved via the characterization of bubble dynamics, via time-resolved photography, formed within fibrin and PEG (600) DA gels which represent both biological and synthetically-derived soft materials. We recover hydrogel material characteristics from the experimental bubble dynamics data and determined that our technique is not only able to optimize for the maximum cavitation bubble radius R_{max}, but also extract the elastic modulus η and failure strain ε_f of the material.

The capability of our platform in delivering mechanical perturbation within a 3D context was also examined. We reported preliminary data whereby delivery of a single cavitation bubble to the vicinity of HUVECs embedded in fibrin gels induced cytosolic Ca^{2+} signalling. Furthermore, we attributed the activation of Ca^{2+} signalling was due to the material strain imparted by the expanding bubble. In a 3D context, our method offers the potential to stimulate cells mechanically whilst deducing mechanical properties of soft materials through measurement of the cavitation bubble dynamics. Potentially, this opens up opportunities for the mechanobiology community investigating mechanotransduction pathways in 3D which is a setting of physiological relevance and the soft matter community for the characterization of materials at high strain-rates.

Chapter 5

Conclusion and Potential Directions

5.1 Summary

In this dissertation, we focused on the development of an optical platform to expose cells to mechanical perturbation in the context of either 2D or 3D cell culture. Our approach enables investigating/screening mechanotransduction and is significant given the importance of mechanical stimuli in regulating cellular processes as well as the etiology and progression of disease.

We presented the development of our optical technology known as the µTsunami platform in Chapter 2. This platform integrates a pulsed laser to provide physical perturbation of cells by µTsunami exposure and fluorescence microscopy for interpreting the stimulated signalling response. Cellular exposure to µTsunami-induced shear stress impulses enabled activation of mechanotransduction as established by the initiation of Ca^{2+} signalling in HUVEC monolayers. The detection of dose-dependent suppression of cellular mechanosignalling with the µTsunami technology by adding putative inhibitor into HUVEC cultures indicates its suitability for HTS that was further reinforced by completion a mock screening experiment just shy of an hour whose speed was limited by the kinetics of the Ca^{2+} signalling process.

Chapter 3 addressed the basic molecular and physical mechanism of Ca^{2+} mechanosignalling elicited by µTsunami stimulation. By conducting inhibition studies, we demonstrated µTsunami initiated Ca^{2+} signalling in HUVECs is dictated by the mechanical activation of ssGPCR and not the chemical activation of purinergics. Moreover, the mechanical nature of µTsunamis was bolstered by discovery that spatial extent in signal propagation depends on impulse magnitude and is governed by a universal curve.

In Chapter 4, we introduced a method to non-invasively quantify the viscoelastic properties of soft materials at high strain-rates known as Laser-Induced Cavitation Rheology (LICR). LICR involves quantitative measurement of the cavitation bubble dynamics formed within the hydrogel interior, viscoelastic modelling of the cavitation bubble dynamics in a manner that accounts for material rupture for comparison with the experimental data, and non-linear least squares optimization to retrieve material properties. LICR was demonstrated to be capable of measuring not only the maximum bubble radius R_{max}, but also the elastic moduli η as well as the material failure strain ε_f in fibrin/PEG (600) DA gels. Furthermore, we presented preliminary data that affirms the ability of our technique to provide mechanical perturbation in the 3D context as revealed by the mechanical activation of Ca^{2+} signalling in HUVECs embedded within fibrin gels.

5.2 Future Directions

Ca^{2+} Signalling Analysis Software

We previously quantified the mechanoresponse of HUVECs by manually determining the probability of Ca^{2+} signalling binned by radial distance from the µTsunami delivery origin. Characterizing the cytosolic calcium signalling probability provides a measure to gauge effectiveness of potential drug compounds. The efficacy of this metric was displayed in our inhibition and mock HTS experiments results where Ca^{2+} signalling probability was significantly diminished following administration of chemical antagonists. Our assessment of the calcium cascade and determination of signalling probabilities were performed by visual inspection. We utilized an image processing program known as ImageJ[98] to monitor cytosolic

Ca^{2+} signalling elicited by HUVECs in the acquired time-series. Cells were manually tracked where we verified whether the calcium cascade occurred and recorded their location relative to the µTsunami delivery site by calculating radial distance. By binning this data, we generated the previously displayed Ca^{2+} signalling probability plots. For our mock HTS results, we reported the probability of calcium signalling within an annular region ranging between 100-150 µm. However, the method we utilized to process our results is not adequate for HTS. Data analysis by hand is low-throughput which attests the necessity of an automated method. Moreover, the quantification of Ca^{2+} signalling probability must also be rapid and consistent for our platform to be truly high-throughput. In accordance, we preliminarily automated this process of analyzing the Ca^{2+} cascade and calculating signalling probabilities through image processing software.

Our software is scripted in MATLAB due to its capabilities in matrix manipulation and image processing. For any given image series, we monitor the calcium fluorescence signals ratiometrically in radial sectors progressing through time instead of tracking individual cells. Each pixel in an image is assigned an angle and radius relative to the coordinates of the µTsunami delivery site. We obtain sectors by introducing constraints on radial and angular ranges which selects or indexes the location of all pixels that fall within criteria. Sector area was equalized by limiting the number of angular divisions at further radial distances. Fig. 5-1 depicts an image divided into radial sectors.

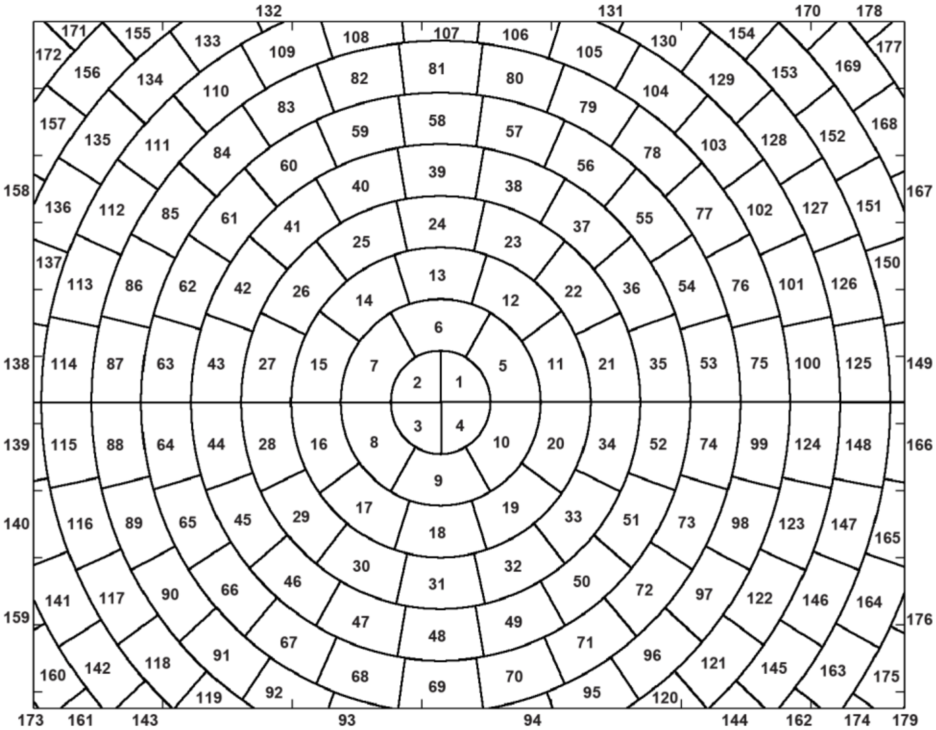

Fig. 5-1 | Image sectorization. An image with 1344 pixel x 1024 pixel that translates to a 436.22 µm x 332.56 µm field of view was divided into sectors and labelled.

Converting the indices into binary masks and applying them on images enabled pulling pixel intensities. The location of these indexed intensities correspond to sector pixel coordinates. Following extraction, we determined the mean intensity of every sector in an image. This was performed on all images in a time-series. A baseline value for each sector was computed by averaging the mean intensities over the number of images prior to µTsunami delivery. The mean intensities of each sector were normalized by dividing with their respective baseline value which yielded a ratio that we monitored. Determining the max(ratio) for each sector and declaring a threshold ratio are required to essentially identify whether a sector exhibited signalling. Sectors with a max ratio value exceeding or equivalent to the threshold are deemed signalling and assigned a value of 1, otherwise 0. Potentially, we can readily calculate the signalling probabilities by determining the radial distance of each sector relative to the pulsed laser delivery origin. Moreover, the ability of our algorithm to detect signalling sectors would be evaluated by subjection to binomial classification testing. This requires manually processing a data set for comparison with the results outputted by the algorithm. Refer to Appendix C for the analysis software.

Bibliography

[1] Mofrad, M.R.K. and Kamm, R.D. *Cellular Mechanotransduction*. Cambridge: Cambridge University Press, 2009.

[2] Blass, B.E. Basic *Principles of Drug Discovery and Development*. Amsterdam: Academic Press, 2015.

[3] Mecham, R.P. The Extracellular Matrix: an Overview. Heidelberg: Springer, 2011.

[4] Ingber, D.E. Cellular mechanotransduction: putting all the pieces together again. *The FASEB Journal*. **20**, 811-827 (2006).

[5] Bao, G. Mechanics of biomolecules. *Journal of the Mechanics and Physics of Solids*. **50**, 2237-2274 (2002).

[6] Iskratsch, T., Wolfenson, H., and Sheetz, M.P. Appreciating the force and shape – the rise of mechanotransduction in cell biology. *Nature Reviews Molecular Cell Biology*. **15**, 825-833 (2014).

[7] Vogel, V. and Sheetz, M. Local force and geometry sensing regulate cell functions. *Nature Reviews Molecular Cell Biology*. **7**, 265-275 (2006).

[8] Chen, C.S. Mechanotransduction – a field pulling together? *Journal of Cell Science*. **121**, 3285-3292 (2008).

[9] Gillespie, P.G. and Müller, U. Mechanotransduction by Hair Cells: Models, Molecules, and Mechanisms. *Cell*. **139**, 33-44 (2009).

[10] Hahn, C. and Schwartz, M.A. Mechanotransduction in vascular physiology and atherogenesis. *Nature Reviews Molecular Cell Biology*. **10**, 53-62 (2009).

[11] Harada, S. and Rodan, G.A. Control of osteoblast function and regulation of bone mass. *Nature*. **423**, 349-355 (2003).

[12] Jaalouk, D.E. and Lammerding, J. Mechanotransduction gone awry. *Nature Reviews Molecular Cell Biology*. **10**, 63-73 (2009).

[13] Orr, A.W., Helmke, B.P., Blackman, B.R., and Schwartz, M.A. Mechanisms of Mechanotransduction. *Developmental Cell*. **10**, 11-20 (2006).

[14] Ingber, D. Mechanobiology and diseases of mechanotransduction. *Annals of Medicine*. **35**, 564-577 (2003).

[15] Schwander, M., Kachar, B., and Müller, U. The cell biology of hearing. *Journal of Cell Biology*. **190**, 9-20 (2010).

[16] Malek, A.M., Alper, S.L., and Izumo, S. Hemodynamic Shear Stress and Its Role in Atherosclerosis. *The Journal of the American Medical Association*. **282**, 2035-2042 (1999).

[17] Chin, L., Xia, Y., Discher, D.E., and Janmey, P.A. Mechanotransduction in cancer. *Current Opinion in Chemical Engineering*. **11**, 77-84, (2016).

[18] Papachroni, K.K., Karatzas, D.N., Papavassiliou, K.A., Basdra, E.K., and Papavassiliou, A.G. Mechanotransduction in osteoblast regulation and bone disease. *Trends in Molecular Medicine*. **15**, 208-216 (2009).

[19] Marcus, R., Feldman, D., Dempster, D.W., Luckey, M., and Cauley, J.A. *Osteoporosis, 4th Edition*. Amsterdam: Academic Press, 2013.

[20] Hughes, J.P., Rees, S., Kalindjian, S.B., and Philpott, K.L. Principles of early drug discovery. *British Journal of Pharmacology*. **162**, 1239-1249 (2010).

[21] Paul, S.M., Mytelka, D.S., Dunwiddie, C.T., Persinger, C.C., Munos, B.H., Lindborg, S.R., and Schacht, A.L. How to improve R&D productivity: the pharmaceutical industry's grand challenge. *Nature Reviews Drug Discovery*. **9**, 203-214 (2010).

[22] Macarron, R., Banks, M.N., Bojanic, D., Burns, D.J., Cirovic, D.A., Garyantes, T., Green, D.V.S., Hertzberg, R.P., Janzen, W.P., Paslay, J.W., Schopfer, U., and Sittampalam, G.S. Impact of high-throughput screening in biomedical research. *Nature Reviews Drug Discovery*. **10**, 188-195 (2011).

[23] Gottlieb, P.A., Suchyna, T.M., Ostrow, L.W., and Sachs, F. Mechanosensitive Ion Channels as Drug Targets. *Current Drug Targets-CNS & Neurological Disorders*. **3**, 287-295 (2004).

[24] Huh, D., Hamilton, G.A., and Ingber, D.E. From 3D culture to organs-on-chips. *Trends in Cell Biology*. **21**, 745-754 (2011).

[25] Scannell, J.W., Blanckley, A., Boldon, H., and Warrington, B. Diagnosing the decline in pharmaceutical R&D efficiency. *Nature Reviews Drug Discovery*. **11**, 191-200 (2012).

[26] Katsumi, A., Orr, A.W., Tzima, E., and Schwartz, M.A. Integrins in Mechanotransduction. *Journal of Biological Chemistry*. **279**, 12001-12004 (2004).

[27] Hay, E.D. *Cell Biology of Extracellular Matrix, 2nd Edition*. New York: Springer, 1991.

[28] Baker, B.M. and Chen, C.S. Deconstructing the third dimension – how 3D culture microenvironments alter cellular cues. *Journal of Cell Science*. **125**, 3015-3024 (2012).

[29] Deakin, N.O. and Turner, C.E. Paxillin comes of age. *Journal of Cell Science*. **121**, 2435-2444 (2008).

[30] Engler, A.J., Sen, S., Sweeney, H.L., Discher, D.E. Matrix Elasticity Directs Stem Cell Lineage Specification. *Cell*. **126**, 677-689 (2006).

[31] Watt, F.M. and Huck, W.T.S. Role of the extracellular matrix in regulating stem cell fate. *Nature Reviews Molecular Cell Biology*. **14**, 467-473 (2013).

[32] Nelson, C.M. and Bissell, M.J. Modeling dynamic reciprocity: Engineering three-dimensional culture models of breast architecture, function, and neoplastic transformation. *Seminars in Cancer Biology*. **15**, 342-352 (2005).

[33] Debnath, J. and Brugge, J.S. Modelling glandular epithelial cancers in three-dimensional cultures. *Nature Reviews Cancer*. **5**, 675-688 (2005).

[34] Hebner, C., Weaver, V.M., and Debnath, J. Modeling Morphogenesis and Oncogenesis in Three-Dimensional Breast Epithelial Cultures. *Annual Review of Pathology: Mechanisms of Disease*. **3**, 313-339 (2008).

[35] Krishnan, R., Park, J., Seow, C.Y., Lee, P.V., and Stewart, A.G. Cellular Biomechanics in Drug Screening and Evaluation: Mechanopharmacology. *Trends in Pharmacological Sciences*. **37**, 87-100 (2016).

[36] Caliari, S.R. and Burdick, J.A. A practical guide to hydrogels for cell culture. *Nature Methods*. **13**, 405-414 (2016).

[37] Compton, J.L., Luo, J.C., Ma, H., Botvinick, E., and Venugopalan, V. High-throughput optical screening of cellular mechanotransduction. *Nature Photonics*. **8**, 710-715 (2014).

[38] Drews, J. Drug Discovery: A Historical Perspective. *Science*. **287**, 1960-1964 (2000).

[39] Charras, G.T. and Horton, M.A. Single Cell Mechanotransduction and Its Modulation Analyzed by Atomic Force Microscope Indentation. *Biophysical Journal*. **82**, 2970-2981 (2002).

[40] Wang, Y., Botvinick, E.L., Zhao, Y., Berns, M.W., Usami, S., Tsien, R.Y., and Chien, S. Visualizing the mechanical activation of Src. *Nature*. **434**, 1040-1045 (2002).

[41] Valberg, P.A. and Butler, J.P. Magnetic particle motions within living cells. Physical theory and techniques. *Biophysical Journal*. **52**, 537-550 (1987).

[42] Kaunas, R., Nguyen, P., Usami, S., and Chien, S. Cooperative effects of Rho and mechanical stretch on stress fiber organization. *Proceedings of the National Academy of Sciences of the United States of America*. **102**, 15895-15900 (2005).

[43] Chien, S. Effects of Distrubed Flow on Endothelial Cells. *Annals of Biomedical Engineering*. **36**, 554-562 (2008).

[44] Rau, K.R., Quinto-Su, P.A., Hellman, A.N., and Venugopalan, V. Pulsed Laser Microbeam-Induced Cell Lysis: Time-Resolved Imaging and Analysis of Hydrodynamic Effects. *Biophysical Journal*. **91**, 317-329 (2006).

[45] Hellman, A.N., Rau, K.R., Yoon, H.H., and Venugopalan, V. Biophysical Response to Pulsed Laser Microbeam-Induced Cell Lysis and Molecular Delivery. *Journal of Biophotonics*. **1**, 24-35 (2008).

[46] Sacchi, C.A. Laser-induced electric breakdown in water. *Journal of the Optical Society of America B*. **8**, 337-345 (1991).

[47] Ready, J.F. *Effects of High-Power Laser Radiation*. Orlando: Academic Press, 1971.

[48] Vogel, A., Noack, J., Hüttman, G., and Paltauf, G. Mechanisms of femtosecond laser nanosurgery of cells and tissues. *Applied Physics B*. **81**, 1015-1047 (2005).

[49] Vogel, A. and Venugopalan, V. Mechanisms of Pulsed Laser Ablation of Biological Tissues. *Chemical Reviews*. **103**, 577-644 (2003).

[50] Venugopalan, V., Guerra, A., III., Nahen, K., and Vogel, A. Role of Laser-Induced Plasma Formation in Pulsed Cellular Microsurgery and Micromanipulation. *Physical Review Letters*. **88**, 078103 (2002).

[51] Vogel, A., Nahen, K., Theisen, D., Birngruber, R., Thomas, R.J., and Rockwell, B.A. Influence of optical aberrations on laser-induced plasma formation in water and their consequences for intraocular photodisruption. *Applied Optics*. **38**, 3636-3643 (1999).

[52] Vogel, A. Nonlinear absorption: intraocular microsurgery and laser lithotripsy. *Physics in Medicine & Biology*. **42**, 895-912 (1997).

[53] Gilmore, F.R. (1952) *The growth or collapse of a spherical bubble in a viscous compressible liquid*. Office of Naval Research. Technical Report 26-4, Hydrodynamics Laboratory, California Institute of Technology, Pasadena, CA.

[54] Knapp, R.T., Daily, J.W., and Hammitt, F.G. *Cavitation*. New York: McGraw-Hill, 1970.

[55] Vogel, A., Busch, S., and Parlitz, U. Shock wave emission and cavitation bubble generation by picosecond and nanosecond optical breakdown in water. *The Journal of the Acoustical Society of America*. **100**, 148-165 (1996).

[56] Vogel, A., Linz, N., Freidank, S., and Paltauf, G. Femtosecond-Laser-Induced Nanocavitation in Water: Implications for Optical Breakdown Threshold and Cell Surgery. *Physical Review Letters*. **100**, 038102 (2008).

[57] Compton, J.L., Hellman, A.N., and Venugopalan, V. Hydrodynamic Determinants of Cell Necrosis and Molecular Delivery Produced by Pulsed Laser Microbeam Irradiation of Adherent Cells. *Biophysical Journal*. **105**, 2221-2231 (2013).

[58] Davies, P.F. Flow-mediated endothelial mechanotransduction. *Physiological Reviews*. **75**, 519-560 (1995).

[59] Fung, Y.C. Biomechanics: Circulation, 2nd Edition. New York: Springer, 1997.

[60] Sigurdson, W.J., Sachs, F., and Diamond, S.L. Mechanical perturbation of cultured human endothelial cells causes rapid increases of intracellular calcium. *American Journal of Physiology Heart and Circulatory Physiology*. **264**, H1745-H1752 (1993).

[61] Clapham, D.E. Calcium Signaling. *Cell*. **131**, 1047-1058 (2007).

[62] Tran, Q.-K. and Watanabe, H. Calcium signalling in the endothelium. *Handbook of Experimental Pharmacology*. **2**, 145-187 (2006).

[63] Frangos, J.A., Eskin, S.G., McIntire, L.V., and Ives, C.L. Flow effects on prostacyclin production by cultured human endothelial cells. *Science*. **227**, 1477-1479 (1985).

[64] Tran, Q., Ohashi, K., and Watanabe, H. Calcium signalling in endothelial cells. *Cardiovascular Research*. **48**, 13-22 (2000).

[65] Chachisvilis, M., Zhang, Y.L., and Frangos, J.A. G protein-coupled receptors sense fluid shear stress in endothelial cells. *Proceedings of the National Academy of Sciences of the United States of America*. **103**, 15463-15468 (2006).

[66] Edelstein, A., Amodaj, N., Hoover, K., Vale, R., and Stuurman, N. Computer Control of Microscopes Using µManager. *Current Protocols in Molecular Biology*. **92**, 14.20.1-14.20.17 (2010).

[67] Palmer, A.E. and Tsien, R.Y. Measuring calcium signaling using genetically targetable fluorescent indicators. *Nature Protocols*. **1**, 1057-1065 (2006).

[68] Park, J.W., Vahidi, B., Taylor, A.M., Rhee, S.W., and Jeon, N.L. Microfluidic culture platform for neuroscience research. *Nature Protocols*. **1**, 2128-2136 (2006).

[69] Yang, M.T., Fu, J., Wang, Y.K., Desai, R.A., and Chen, C.S. Assaying stem cell mechanobiology on microfabricated elastomeric substrates with geometrically modulated rigidity. *Nature Protocols*. **6**, 187-213 (2011).

[70] Malek, A.M., Alper, S.L., and Izumo, S. Hemodynamic Shear Stress and Its Role in Atherosclerosis. *The Journal of the American Medical Association*. **282**, 2035-2042 (1999).

[71] Liu, B., Lu, S., Zheng, S., Jiang, Z., and Wang, Y. Two distinct phases of calcium signalling under flow. *Cardiovascular Research*. **91**, 124-133 (2011).

[72] Bishara, N.B., Murphy, T.V., and Hill, M.A. Capacitative Ca^{2+} entry in vascular endothelial cells is mediated via pathways sensitive to 2 aminoethoxydiphenyl borate and xestospongin C. *British Journal of Pharmacology*. **135**, 119-128 (2002).

[73] He, H., Nakagawa, K., Wang, Y., Hosokawa, Y., and Goda, K. Mechanism for microtsunami-induced intercellular mechanosignalling. *Nature Photonics*. **9**, 623 (2015).

[74] Luo, J.C., Botvinick, E.L., and Venugopalan, V. Reply to 'Mechanism for microtsunami-induced intercellular mechanosignalling.' *Nature Photonics*. **9**, 624-625 (2015).

[75] Alberts, B., Johnson, A., Lewis, J., Raff, M., Roberts, K., and Walter, P. *Molecular Biology of the Cell, 4th Edition*. New York: Garland Science, 2002.

[76] Missiaen, L., Callewaert, G., De Smedt, H., and Parys, J.B. 2-aminoethoxydiphenyl borate affects the inositol 1,4,5-triphosphate receptor, the intracellular Ca^{2+} pump and the non-specific Ca^{2+} leak from the non-mitochondrial Ca^{2+} stores in permeabilized A7r5 cells. *Cell Calcium*. **29**, 111-116 (2001).

[77] Burnstock, G. Purinergic signalling. *British Journal of Pharmacology*. **147**, S172-S187 (2006).

[78] Kaczmarek, E. Nucleotides and Novel Signaling Pathways in Endothelial Cells: Possible Roles in Angiogenesis, Endothelial Dysfunction and Diabetes Mellitus. In: Gerasimovskaya, E. and Kaczmarek, E. (eds) *Extracellular ATP and Adenosine as Regulators of Endothelial Cell Function*. Dordrecht: Springer, 2010.

[79] Erlinge, D. and Burnstock, G. P2 receptors in cardiovascular regulation and disease. *Purinergic Signal*. **4**, 1-20 (2008).

[80] Jacobson, K.A. *P2X and P2Y Receptors*. Tocris Bioscience, 2010.

[81] Kaslow, H.R. and Burns, D.L. Pertussis toxin and target eukaryotic cells: binding, entry, and activation. *FASEB Journal*. **6**, 2684-2690 (1992).

[82] Beindl, W., Mitterauer, T., Hoheneggar, M., Ijzerman, A.P., Nanoff, C., and Freissmuth, M. Inhibition of receptor/G protein coupling by suramin analogues. *Molecular Pharmacology*. **50**, 415-423 (1996).

[83] Griffith, L.G. and Swartz, M.A. Capturing complex 3D tissue physiology *in vitro*. *Nature Reviews Molecular Cell Biology*. **7**, 211-224 (2006).

[84] Yamada, K.M. and Cukierman, E. Modeling Tissue Morphogenesis and Cancer in 3D. *Cell*. **130**, 601-610 (2007).

[85] Pampaloni, F., Reynaud, E.G., and Stelzer, E.H.K. The third dimension bridges the gap between cell culture and live tissue. *Nature Reviews Molecular Cell Biology*. **8**, 839-845 (2007).

[86] Huh, D., Torisawa, Y., Hamilton, G.A., Kim, H.J., and Ingber, D.E. Microengineered physiological biomimicry: Organs-on-Chips. *Lab Chip*. **12**, 2156-2164 (2012).

[87] Paszek, M.J., Zahir, N., Johnson, K.R., Lakins, J.N., Rozenberg, G.I., Gefen, A., Reinhart-King, C.A., Margulies, S.S., Dembo, M., Boettiger, D., Hammer, D.A., and Weaver, V.M. Tensional homeostasis and the malignant phenotype. *Cancer Cell*. **8**, 241-254 (2005).

[88] Przybyla, L., Muncie, J.M., and Weaver, V.M. Mechanical Control of Epithelial-to-Mesenchymal Transitions in Development and Cancer. *Annual Review of Cell and Developmental Biology*. **32**, 527-554 (2016).

[89] Muncie, J.M. and Weaver, V.M. The Physical and Biochemical Properties of the Extracellular Matrix Regulate Cell Fate. *Current Topics in Developmental Biology*. **130**, 1-37 (2018).

[90] Leight, J.L., Drain, A.P., and Weaver, V.M. Extracellular Matrix Remodeling and Stiffening Modulate Tumor Phenotype and Treatment Response. *Annual Review of Cancer Biology*. **1**, 313-334 (2017).

[91] Keating, M., Kurup, A., Alvarez-Elizondo, M., Levine, A.J., and Botvinick, E. Spatial distributions of pericellular stiffness in natural extracellular matrices are dependent on cell-mediated proteolysis and contractility. *Acta Biomaterialia*. **57**, 304-312 (2017).

[92] Piechocka, I.K., Bacabac, R.G., Potters, M., MacKintosh, F.C., and Koenderink, G.H. Structural Hierarchy Governs Fibrin Gel Mechanics. *Biophysical Journal*. **98**, 2281-2289 (2010).

[93] Engler, A.J., Rehfeldt, F., Sen, S., and Discher, D.E. Microtissue Elasticity: Measurements by Atomic Force Microscopy and Its Influence on Cell Differentiation. *Methods in Cell Biology*. **83**, 521-545 (2007).

[94] Chen, D.T.N., Wen, Q., Janmey, P.A., Crocker, J.C., and Yodh, A.G. Rheology of Soft Materials. *Annual Review of Condensed Matter Physics*. **1**, 301-322 (2010).

[95] Lang, N.R., Skodzek, K., Hurst, S., Mainka, A., Steinwachs, J., Schneider, J., Aifantis, K.E., and Fabry, B. Biphasic response of cell invasion to matrix stiffness in three-dimensional biopolymer networks. *Acta Biomaterialia*. **13**, 61-67 (2015).

[96] Gaudron, R., Warnez, M.T., and Johnsen, E. Bubble dynamics in a viscoelastic medium with nonlinear elasticity. *Journal of Fluid Mechanics*. **766**, 54-75 (2015).

[97] Glinsky, M.E., Bailey, D.S., London, R.A., Amendt, P.A., Rubenchik, A.M., and Strauss, M. An extended Rayleigh model of bubble evolution. *Physics of Fluids*. **13**, 20-31 (2001).

[98] Schneider, C.A., Rasband, W.S., and Eliceiri, K.W. NIH Image to ImageJ: 25 years of image analysis. *Nature Methods*. **9**, 671-675 (2012).

Appendices

Appendix A. Computational Scripts to Calculate µTsunami Generated Shear Stress Impulse in 2D Cell Cultures

Gilmore_Solver.m

```
clear all; close all; clc; %Clear All Variables; Close All Figure Windows;
Clear All Command Window Text;

Rmax_Actual = (107)*1.0e-6; %Actual Maximum Bubble Radius Measured From Time-
Resolved Imaging For Comparison [m]
R_Gilmore = (139)*1.0e-6; %Rmax Inputted Into Gilmore Model... Accounted For
Reduced Size Due To Compressibility [m]

tspan = 0:1.0e-10:1.0e-4; %Time Points Evaluated with 0.1 ns Spacing From 0
To 100 us [s]

options = odeset('RelTol',1.0e-10,'AbsTol',1.0e-13); %Set Error Tolerances
RBVB = zeros(length(tspan),2); %Creates Array For Storing Bubble Radius And
Velocity

tic %Start Timer 1
[t,RBVB(:,:)] = ode113(@ODESolver_Gilmore,tspan,[R_Gilmore
0],options,R_Gilmore); %Calls Gilmore Equation Function And Evaluates
Numerically With ode113()
% LHS Output Format: [time, Bubble Radius & Velocity]
% RHS Format: ode113(@Call Gilmore Solver To Numerically Compute Compressible
Cavitation Dynamics, Timespan, Initial Conditions, Options, R_Gilmore)
%Outputs: [time span output, bubble radius & velocity output] = Inputs:
ode113(@ call gilmore equations function, time span, initial conditions,
error tolerances, R_Gilmore)
toc %Stop Timer 1 And Display Duration Elapsed In Seconds

RB = RBVB(:,1); %Bubble Radius
VB = RBVB(:,2); %Bubble Velocity
```

```
% figure(1); %Create Figure 1
% plot(t*1.0e6,RB*1.0e6,'b-'); %Plot Bubble Radius
% xlabel('Time (\mus)'); ylabel('Bubble Radius (\mum)'); %Axis Labels

[pks,locs] = findpeaks(RB-(1.01*RB)); %Determines Start And End Of Bubble
Cycle

t_bubble_cycle = t(locs(1):locs(2)); %Indexes Time Points Of 1st Full Bubble
Cycle
t_bubble_cycle_normalized = t_bubble_cycle - t(locs(1)); %Shifts Start Of
Bubble Cycle To 0
RB_bubble_cycle = RB(locs(1):locs(2)); %Indexes Radii Of 1st Full Bubble
Cycle
VB_bubble_cycle = VB(locs(1):locs(2)); %Indexes Velocity Of 1st Full Bubble
Cycle

% figure(2); %Create Figure 2
% plot(t_bubble_cycle_normalized*1e6,RB_bubble_cycle*1e6,'b-'); %Plot Indexed
Bubble Radius
% xlabel('Time (\mus)'); ylabel('Bubble Radius (\mum)'); %Axis Labels

% figure(3); %Create Figure 3
% plot(t_bubble_cycle_normalized*1e6,VB_bubble_cycle*1e6,'b-'); %Plot Indexed
Bubble Velocity
% xlabel('Time (\mus)'); ylabel('Bubble Velocity (m/s)'); %Axis Labels

tic %Start Timer 2
[AB_bubble_cycle] =
Acceleration_Gilmore(R_Gilmore,RB_bubble_cycle,VB_bubble_cycle); %Calculate
Bubble Acceleration [m/s^-2]
% LHS Format: [Bubble Cycle Acceleration]
% RHS Format: Acceleration_Gilmore(Gilmore Rmax, Bubble Cycle Radius, Bubble
Cycle Velocity)
toc %Stop Timer 2 And Display Duration Elapsed In Seconds

r = [25 50 75 100 125 150 175 200 225 250 275 300 325 350 375 400 425 450 475
500]*1.0e-6; %Radial Position To Evaluate Shear Stress And Impulse
tic %Start Timer 3
[tau,singletime,ddtV_inf,ddtrho_b,rho_b,P_wall_new] =
ShearStress_Gilmore(r,R_Gilmore,RB_bubble_cycle,VB_bubble_cycle,AB_bubble_cyc
le,t_bubble_cycle_normalized); %Calculate Shear Stress, tau [Pa]
% LHS Format: [Shear Stress, Time Point For Evaluating Shear Stress,
Derivative Of V Infinity, Derivative Of Bubble Density, Bubble Density,
Bubble Wall Pressure]
% RHS Format: ShearStress_Gilmore(Radial Locations To Evaluate Shear Stress,
Gilmore Rmax, Bubble Cycle Radius, Bubble Cycle Velocity, Bubble Cycle
Acceleration, Bubble Cycle Time Normalized)
toc %Stop Timer 3 And Display Duration Elapsed In Seconds

ImpulseFull = max(cumtrapz(t_bubble_cycle_normalized,abs(tau(:,:))))';
%Compute Impulse
```

ODESolver_Gilmore.m

```
function yp = ODESolver_Gilmore(tspan,RBVB,R_Gilmore) %Gilmore ODE Solver
Function
% Format: ODESolver_Gilmore(Time To Evaluate, Array To Store Bubble
Radius/Velocity, Gilmore Rmax)
% Function For Passing A System Of Equations Converted From The Gilmore Model
To Solve For Bubble Radius And Velocity

kappa = 4/3; %Polytropic Constant [ ]
rho_l = 997; %Density Of Water At 25C [kg/m^3]
mu_l = 0.894e-3; %Viscosity Of Water At 25C [kg/(m s)]
sigma = 0.072; %Surface Tension Of Water At 25C [N/m]
P_vap = 3169; %Vapor Pressure At 25C [Pa]
P_stat = 101325; %Static Pressure Of Water [Pa]
P_inf = P_stat; %Pressure Far Away From The Bubble
n = 7; %Tait Equation Constant [ ]
B = 314000000; %Tait Equation Constant [Pa]
c_l = 1483; %Speed Of Sound In Water [m/s]

%Equilibrium Bubble Radius, Rn [m]
Rn = ((R_Gilmore^3) * (P_vap/P_inf)).^(1/3);

%Pressure At The Bubble Wall, P [Pa]
P_wall = (P_inf + 2 * sigma / Rn) * ((Rn / RBVB(1))^(3 * kappa)) - (2 * sigma
/ RBVB(1)) - (4 * mu_l * RBVB(2) / RBVB(1));

%Enthalpy At The Bubble Wall, H
H = n * (P_inf + B) / ((n - 1) * rho_l) * ((((P_wall + B) / (P_inf + B))^((n
- 1) / n)) - 1);

%Derivative Of Pressure At The Bubble Wall With Respect To R (Bubble Radius)
dPdR = -3 * kappa * (P_inf + (2 * sigma / Rn)) * ((Rn / RBVB(1))^(3 * kappa))
/ RBVB(1) + (2 * sigma / (RBVB(1) * RBVB(1))) + (4 * mu_l * RBVB(2) /
(RBVB(1) * RBVB(1)));

%Derivative Of Enthalpy At The Bubble Wall With Respect To R (Bubble Radius)
dHdR = (1 / rho_l) * (((P_inf + B) / (P_wall + B))^(1 / n)) * dPdR;

%Speed Of Sound In Water, C
C = (((c_l)^2) + ((n - 1) * H))^0.5;

%yp = yprime = bubble velocity
%y3(1) = RBVB(1) = bubble radius [m]
%y3(2) = RBVB(2) = bubble velocity [m/s]

yp = zeros(2,1); %Create Column Vector To Insert Gilmore System Of Equations
yp(1,1) = RBVB(2);
yp(2,1) = (((-3/2)*(1-(RBVB(2)/(3*C)))*(RBVB(2)*RBVB(2))) + ((1 +
(RBVB(2)/C))*H) + ((RBVB(2)/C)*(1-(RBVB(2)/C))*RBVB(1)*dHdR)) * ((RBVB(1)*(1-
(RBVB(2)/C)))^(-1));
```

Acceleration_Gilmore.m

```
function [AB_bubble_cycle] =
Acceleration_Gilmore(Rmax_Actual,RB_bubble_cycle,VB_bubble_cycle)
%Acceleration Function
% Format: Acceleration_Gilmore(Actual Measured Rmax, Bubble Cycle Radius,
Bubble Cycle Velocity)
% Computes Bubble Cycle Acceleration

kappa = 4/3; %Polytropic Constant [ ]
rho_l = 997; %Density Of Water At 25C [kg/m^3]
mu_l = 0.894e-3; %Viscosity Of Water At 25C [kg/(m s)]
sigma = 0.072; %Surface Tension Of Water At 25C [N/m]
P_vap = 3169; %Vapor Pressure At 25C [Pa]
P_stat = 101325; %Static Pressure Of Water [Pa]
P_inf = P_stat; %Pressure Far Away From The Bubble
n = 7; %Tait Equation Constant [ ]
B = 314000000; %Tait Equation Constant [Pa]
c_l = 1483; %Speed Of Sound In Water [m/s]

%Equilibrium Bubble Radius, Rn [m]
Rn = ((Rmax_Actual^3) * (P_vap/P_inf)).^(1/3);

%Pressure At The Bubble Wall, P [Pa]
P_wall = (P_inf + 2 * sigma / Rn) * ((Rn ./ RB_bubble_cycle).^(3 * kappa)) -
(2 * sigma ./ RB_bubble_cycle) - (4 * mu_l * VB_bubble_cycle ./
RB_bubble_cycle);

%Enthalpy At The Bubble Wall, H
H = n * (P_inf + B) / ((n - 1) * rho_l) * ((((P_wall + B) ./ (P_inf +
B)).^((n - 1) / n)) - 1);

%Derivative Of Pressure At The Bubble Wall With Respect To R (Bubble Radius)
dPdR = -3 * kappa * (P_inf + (2 * sigma / Rn)) * ((Rn ./ RB_bubble_cycle).^(3
* kappa)) ./ RB_bubble_cycle + (2 * sigma ./ (RB_bubble_cycle .*
RB_bubble_cycle)) + (4 * mu_l * VB_bubble_cycle ./ (RB_bubble_cycle .*
RB_bubble_cycle));

%Derivative Of Enthalpy At The Bubble Wall With Respect To R (Bubble Radius)
dHdR = (1 / rho_l) * (((P_inf + B) ./ (P_wall + B)).^(1 / n)) .* dPdR;

%Speed Of Sound In Water, C
C = (((c_l)^2) + ((n - 1) * H)).^0.5;

%Bubble Cycle Acceleration
[AB_bubble_cycle] = (((-3/2) * (1 - (VB_bubble_cycle ./ (3 * C))) .*
(VB_bubble_cycle .* VB_bubble_cycle)) + ((1 + (VB_bubble_cycle ./ C)) .* H) +
((VB_bubble_cycle ./ C) .* (1 - (VB_bubble_cycle ./ C)) .* RB_bubble_cycle .*
dHdR)) .* ((RB_bubble_cycle .* (1 - (VB_bubble_cycle ./ C))).^(-1));

end
```

ShearStress_Gilmore.m

```
function [tau,singletime,ddtV_inf,ddtrho_b,rho_b,P_wall_new] =
ShearStress_Gilmore(r,R_Gilmore,RB_bubble_cycle,VB_bubble_cycle,AB_bubble_cyc
le,t_bubble_cycle_normalized) %Shear Stress Function
% LHS Format: [Shear Stress, Time Points For Evaluating Shear Stress,
Derivative Of V Infinity, Derivative Of Bubble Density, Bubble Density,
Bubble Wall Pressure]
% RHS Format: ShearStress_Gilmore(Radial Locations To Evaluate Shear Stress,
Gilmore Rmax, Bubble Cycle Radius, Bubble Cycle Velocity, Bubble Cycle
Acceleration, Bubble Cycle Time Normalized)
% Computes Shear Stress

kappa = 4/3; %Polytropic Constant [ ]
rho_l = 997; %Density Of Water At 25C [kg/m^3]
mu_l = 0.894e-3; %Viscosity Of Water At 25C [kg/(m s)]
sigma = 0.072; %Surface Tension Of Water At 25C [N/m]
P_vap = 3169; %Vapor Pressure At 25C [Pa]
P_stat = 101325; %Static Pressure Of Water [Pa]
P_inf = P_stat; %Pressure Far Away From The Bubble
n = 7; %Tait Equation Constant [ ]
B = 314000000; %Tait Equation Constant [Pa]
c_l = 1483; %Speed Of Sound In Water [m/s]
nu_l = mu_l/rho_l; %Kinematic Viscosity Of Water At 25C [m^2/s], 0.8966e-6

ddtV_inf = zeros(length(RB_bubble_cycle),length(r)); %Creates Matrix To Store
Derivative Of V Infinity Values

for i = 1 : length(r) %Loops Through Radial Locations

    %Equilibrium Bubble Radius, Rn [m]
    Rn = ((R_Gilmore^3) * (P_vap/P_inf)).^(1/3);

    %Pressure At The Bubble Wall, P [Pa]
    P_wall_new = (P_inf + 2 * sigma / Rn) * ((Rn ./ RB_bubble_cycle).^(3 *
kappa)) - (2 * sigma ./ RB_bubble_cycle) - (4 * mu_l * VB_bubble_cycle ./
RB_bubble_cycle);

    %Bubble Density From The Tait Equation
    rho_b = rho_l * ((P_wall_new + B) ./ (P_inf + B)).^(1 / n);

    %Derivative Of Pressure At The Bubble Wall With Respect To Time
    dPdt = ((-3 * kappa) ./ RB_bubble_cycle) .* (P_inf + ((2 * sigma) /
Rn)) .* ((Rn ./ RB_bubble_cycle).^(3 * kappa)) + (((2 * sigma) ./
(RB_bubble_cycle .* RB_bubble_cycle)) .* VB_bubble_cycle) + ((4 * mu_l *
VB_bubble_cycle) ./ (RB_bubble_cycle .* RB_bubble_cycle)) - ((4 * mu_l *
AB_bubble_cycle) ./ RB_bubble_cycle);

    %Derivative Of Bubble Density With Respect To Time
    ddtrho_b = (rho_l / (n * (P_inf + B))) .* (((P_wall_new + B) ./ (P_inf +
B)).^((1 / n) - 1)) .* dPdt;

    %Derivative Of V_inf With Respect To Time
```

```
    ddtV_inf(:,i) = (1 / (rho_l * r(i) * r(i))) * ((ddtrho_b .*
RB_bubble_cycle .* RB_bubble_cycle .* VB_bubble_cycle) + (rho_b .*
RB_bubble_cycle .* RB_bubble_cycle .* AB_bubble_cycle) + (2 .* rho_b .*
RB_bubble_cycle .* VB_bubble_cycle .* VB_bubble_cycle));

end %Radial Location Loop End

timepoints = length(t_bubble_cycle_normalized); %Time Points To Evaluate
Shear Stress

Integral = zeros(timepoints,length(r)); %Create Matrix To Store Integral
Values

for j = 1 : length(r) %Loops Through # Of Radial Positions

    for k = 4 : timepoints %Loops Through Time Points

        tprime = t_bubble_cycle_normalized(1 : k - 1);
        dotV_inf = ddtV_inf(1 : k - 1, j);
        y = dotV_inf ./ (sqrt(t_bubble_cycle_normalized(k) - tprime));
        leny = length(y);
        const = (t_bubble_cycle_normalized(k) - t_bubble_cycle_normalized(1))
/ (3 * (length(y) - 1));

        if ~rem(leny,2)

            simp13 = [1, repmat([4,2],1,(leny - 2) / 2),1];

        else

            simp13 = [1, repmat([4,2],1,(leny - 3) / 2),4,1];

        end

        Integral(k,j) = const * sum(y .* simp13');

    end %Time Point Loop End

end %# Of Radial Position Loop End

singletime = t_bubble_cycle_normalized(1:timepoints);
tau = rho_l * sqrt((mu_l / rho_l) / pi) * Integral; %Compute Shear Stress

end
```

Appendix B. Programs for Modelling Cavitation Bubble Dynamics in Viscoelastic Media to Compute the Compressive Modulus, Material Rupture Strain, and Finite Strain Field

B1. Cavitation Dynamics Measurement

cavitation_measurement.m

```
clear all; close all; clc; %Clear All Variables; Close All Figure Windows;
Clear Command Window Text

image_list = dir('*.tif'); %Reads All .tif Files In Current Folder
image_size = size(double(imread(image_list(1).name))); %Determines Image
Resolution, Outputs In [Row,Column] Format

k = 2; %Number Of Clusters

for i = 1 : length(image_list) %Loops Through Cavitation Images

image = (2^(16+1)) - double(imread(image_list(i).name)); %Reads In Cavitation
Images And Converts To Double Precision... Subtract By 16-bit Intensity Limit
So Cavitation Pixels Are Greater Intensity
figure(); imagesc(image); %colormap(gray); %Creates Figure And Displays
Cavitation Image

[idx,C] =
kmeans(image(:),k,'EmptyAction','singleton','Replicates',1,'Start','Uniform')
; %Cluster Partitions Linearised Cavitation Images Into k Pixel Classes
class = reshape(idx,image_size); %Reshapes Classified Linearised Cavitation
Images Into Original Resolution

[SA,SI] = sort(mean(C,2)); %Sorts Pixel Classes In Ascending Order And
Assigns Index Value
class_temp = class; %Creates Temporary Class Variable, Prevents Overriding
Original Reshaped Partitioned Image Variable
class_temp(class_temp == SI(1,1)) = 0; %Sets Background Or Lowest Class
Pixels To 0, Cavitation Pixels Retain Index Value
% figure(); imagesc(class_temp); %colormap(gray); %Creates Figure And
Displays Image Of Retained Classified Cavitation Pixels

bw = im2bw(class_temp); %Convert Classified Cavitation Images To Binary
bw2 = bwareaopen(bw,1000); %Removes Small Objects With Number Of Pixels Less
Than Specified Value From Binary Image
bw3 = imfill(bw2,'holes'); %Fill Image Regions And Holes
figure(); imagesc(bw3); %colormap(gray); %Creates Figure And Displays Binary
Filled Image
stats(i) =
regionprops(bw3,'MajorAxisLength','MinorAxisLength','EquivDiameter');
%Measures Cavitation Major/Minor Axis Length And Equivalent Diameter
```

```
end %Image Loop End

list = reshape(struct2array(stats),[3,length(image_list)])'; %Extract
Measured Values From Structure

close all; %Close All Figure Windows
```

B2. Non-Linear Least Squares Optimization

lsq_ERP_Euler_switch_NH.m

```
clear all; close all; clc; %Clear All Variables; Close All Figure Windows;
Clear All Command Window Text;

rng('shuffle'); %Shuffles RNG Seed Based On Current Time

load('filename.mat'); %Imports Experimental Data Of Cavitation Dynamics In
Hydrogels

iguess_number = 35; %# Of Initial Guesses Or Times To Run lsqcurvefit-ting
Algorithm
rng_range = rand(iguess_number,3); %Initializes Matrix With Random Values To
Generate A Specified Range Of Initial Guesses

iG_random = (47693.58 - 21467.70) * rng_range(:,1) + 21467.70; %Random
Initial Guess Range For Elastic Moduli [Pa]
iRmax_random = (108.66 - 98.37) * rng_range(:,2) + 98.37; %Random Initial
Guess Range For Maximum Bubble Radius, Rmax [um]
ief_random = (0.4051 - 0.2162) * rng_range(:,3) + 0.2162; %Random Initial
Guess Range For Material Failure Strain, epsilon f [ ]
iGRmax_random = [iG_random*1e-9,iRmax_random*1e-6,ief_random*1e-5]; %Compile
Initial Guesses Inputted Into Fitting Algorithm

options1 = optimset('diagnostics','on','Algorithm','levenberg-
marquardt','Display','iter-detailed','TolX',1e-12,'TolFun',1e-12);
Set Fitting Options: Turn On Diagnostics, Use Levenberg-Marquardt Algorithm,
Display Output Iteratively, And Function/Step Tolerance At 1e-12
lb = []; ub = []; %Lower And Upper Bound Values;

tic %Start Timer
for r = 1 : length(iGRmax_random) %Loops Through # Of Initial Guesses

[fitGRmax(r,:),resnorm(r,:),residual(:,r),exitflag(r,:),output(r,:),lambda(r,
:),jacobian(:,:,r)] =
lsqcurvefit(@forward_solver_ERP_Euler_switch_NH_1em9,iGRmax_random(r,:),test_
time,test_radius,lb,ub,options1);
% LHS Format: [Parameter Best Fit Values, Chi2 Error, Residual, Reason For
Stopping Solver, Optimization Process Information, Lagrange Multipliers At
Solution, Jacobian At Solution]
```

```
% RHS Format: lsqcurvefit(@Call Forward Solver To Compute Error Between
Experimental & Model Data, Initial Guesses, Experimental X & Y Data Points,
Lower & Upper Bound, Options)

end %Initial Guess Loop End
toc %End Timer And Display Duration Elasped In Seconds

ci =
nlparci(fitGRmax(min_index,:),residual(:,min_index),jacobian(:,:,min_index));
%95% Confidence Interval For Best Fits
ci(1,:) = ci(1,:) * 1e9; % Elastic Moduli 95% Confidence Interval [Pa]
ci(2,:) = ci(2,:) * 1e6; % Maximum Bubble Radius, Rmax, 95% Confidence
Interval [um]
ci(3,:) = ci(3,:) * 1e5; % Material Failure Strain 95% Confidence Interval
[ ]

save('output.mat'); %Save Outputted Variables In Workspace
```

forward_solver_ERP_Euler_switch_NH.m

```
function R = forward_solver_ERP_Euler_switch_NH(iGRmax,xdata) %Forward Solver
Function
% Format: (Initial Guesses, Experimental Data Time Points)
% Numerically Outputs Viscoelastic Bubble Model Results And Compares With
Experimental Data To Compute Chi2 Error

RB(1) = iGRmax(2); disp(sprintf('Rmax_Actual = %e',RB(1))); %Set And Display
Initial Maximum Bubble Radius Guess, Rmax [m]
VB(1) = 0; %Initial Bubble Velocity [m/s]
G = iGRmax(1)*1e9; disp(sprintf('iG = %e',G)); %Set And Display Initial
Elastic Modulus Guess [Pa]

dt = 1.0e-9; %Time Steps [s]
t = 0:dt:1.0e-4; %Time Points Evaluated With 0.1 ns From 0 To 100 us [s]

kappa = 4/3; %Polytropic Constant [ ]
rho_l = 997; %Density Of Water At 25C [kg/m^3]
mu_l = 0.894e-3; %Viscosity Of Water At 25C [kg/(m s)]
S = 0.072; %Surface Tension Of Water At 25C [N/m]
P_vap = 3169; %Vapor Pressure At 25C [Pa]
P_inf = 101325; %Pressure Far Away From The Bubble Or Static Pressure Of
Water [Pa]
ef = iGRmax(3)*1e5; disp(sprintf('ief = %e',ef)); %Set And Display Initial
Material Failure Strain Guess [ ]

Ro = ((RB(1)^3) * (P_vap / P_inf)).^(1/3); %Initial Or Equilibrium Radius [m]
% PBB(1) = P_vap*(RB(1)./RB(1)).^(3*kappa); %Initial Partial Gas Pressure
[Pa]
E = (G / 2) * (5 - (4 * Ro / RB(1)) - ((Ro / RB(1))^4)); %EE(1) = E; %Initial
Neo-Hookean Elasticity [Pa] - Linear, Johnsen
ebw = -(1 / 2) * (((Ro / RB(1))^4) - 1); %eebw(1) = ebw; lol(1) = 25;
%Initial Bubble Wall Strain [ ]
```

```
counter = 1; n_switch = 1; %Counters To Determine Start Of Actual Bubble
Cycle & Rmax And Switching Between Elastic Term Variations

tic %Start Timer
for i = 1 : length(t)-1 %Loops Through Time Steps

    if (VB(i) > 0) && (counter == 1) %Checks When Actual Bubble Cycle
Starts... If So,...
        counter = counter + 1; %Increases Counter By 1
        Rmin = RB(i); %Stores Minimum Bubble Radius At Start Of Cycle, Rmin
[m]
        Rmin_index = find(Rmin == RB(1:i)); %Stores Index At Rmin
    elseif (counter == 1) %If Not, Implement...
        E = (G / 2) * (5 - (4 * Ro / RB(i)) - ((Ro / RB(i))^4)); %EE(i+1) =
E; %Neo-Hookean Elastic Term [Pa] - Linear, Johnsen
    end %Actual Bubble Cycle Start Check End

    if (VB(i) < 0) && (counter == 2) && (i >= Rmin_index) %Checks When
Maximum Bubble Radius Is Reached... If So,...
        counter = counter + 1; %Increases Counter By 1
        Rmax = RB(i); %Stores Maximum Bubble Radius At Apex Of Cycle, Rmax
[m]
        Rmax_index = find(Rmax == RB(1:i)); %Stores Index At Rmax
    end %Rmax Check End

    if (counter == 2) && (i >= Rmin_index) && (G ~= 0) %1st Checks: (1) After
Actual Bubble Cycle Starts, (2) Current Index Is Greater Than Index At Rmin,
And (3) Elasticity > 0... If So,...
        if (ebw < ef) && (n_switch == 1) %2nd Checks: (1) Bubble Wall Strain
< Material Failure Strain And (2) n_switch Value = 1... If So, Implement...
            E = (G / 2) * (5 - (4 * Ro / RB(i)) - ((Ro / RB(i))^4)); %EE(i+1)
= E; %Neo-Hookean Elastic Term [Pa] - Linear, Johnsen
        elseif (ebw > ef) && (n_switch == 1) %Otherwise, Check: (1) Bubble
Wall Strain > Material Failure Strain And (2) n_switch Value = 1... If So,
Implement...
            n_switch = n_switch + 1; %Increases n_switch By 1
            Rf = RB(i); %Stores Radius At Which Material Failures [m]
            Rf_index = find(Rf == RB(1:i)); %Stores Index At Rf
            E = (G / 2) * (5 - (4 * Ro / Rf) - ((Ro / Rf)^4)); %EE(i+1) = E;
%Neo-Hookean Elastic Term [Pa] - Fixed Failure, Johnsen
            Yf = E; %Store Fixed Failure Stress [Pa]
        elseif (n_switch == 2) %Otherwise, Check n_switch Value = 2... If So,
Implement...
            E = (G / 2) * (5 - (4 * Ro / Rf) - ((Ro / Rf)^4)); %EE(i+1) = E;
%Neo-Hookean Elastic Term [Pa] - Fixed Failure, Johnsen
        end %2nd Checks End
    elseif (counter == 2) && (i >= Rmin_index) && (G == 0) %Otherwise,
Checks: (1) After Actual Bubble Cycle Starts, (2) Current Index Is Greater
Than Index At Rmin , And (3) Elasticity = 0... If So, Implement...
        E = 0; %EE(i+1) = E; %(G / 2) * (5 - (4 * Ro / RB(i)) - ((Ro /
RB(i))^4)); EE(i+1) = E; %Neo-Hookean Elastic Term [Pa] - Johnsen
    end %1st Checks End

    if (counter == 3) && (i >= Rmax_index) && (G ~= 0) %1st Checks: (1) After
Bubble Cycle Passes Apex, (2) Current Index Is Greater Than Index At Rmax,
And (3) Elasticity > 0... If So,...
```

```
        if (n_switch == 2) %2nd Check: n_switch Value = 2... If So, Implement...
            Emax = (5 - (4 * Ro / Rmax) - ((Ro / Rmax)^4)); %Neo-Hookean Elastic Term [Pa] - Fixed Rmax, Johnsen
            E = (5 - (4 * Ro / RB(i)) - ((Ro / RB(i))^4)) * (Yf / Emax); %EE(i+1) = E; %Neo-Hookean Elastic Term [Pa] - Recovery, Johnsen
        elseif (n_switch == 1) %Otherwise, Check n_switch Value = 1... If So, Implement...
            E = (G / 2) * (5 - (4 * Ro / RB(i)) - ((Ro / RB(i))^4)); %EE(i+1) = E; %Neo-Hookean Elastic Term [Pa] - Linear, Johnsen
        end %2nd Check End
    elseif (counter == 3) && (i >= Rmax_index) && (G == 0) %Otherwise, Checks: (1) After Bubble Cycle Passes Apex, (2) Current Index Is Greater Than Index At Rmax, And (3) Elasticity = 0... If So, Implement
        E = 0; %EE(i+1) = E; %(G / 2) * (5 - (4 * Ro / RB(i)) - ((Ro / RB(i))^4)); EE(i+1) = E; %Neo-Hookean Elastic Term [Pa] - Johnsen
    end %1st Checks End

    RB(i+1) = RB(i) + (dt * VB(i)); %Solves For Bubble Radius [m]

    PB = P_vap*(RB(1)./RB(i)).^(3*kappa); %PBB(i+1) = PB; %Partial Gas Pressure [Pa]
    ebw = -(1 / 2) * (((Ro / RB(i))^4) - 1); %eebw(i+1) = ebw; %Bubble Wall Strain []
    VB(i+1) = VB(i) + (dt * (((PB - P_inf)/(rho_l * RB(i))) - ((3 * VB(i) * VB(i))/(2 * RB(i))) - (((4 * mu_l * VB(i)) + (2 * S))/(rho_l * RB(i) * RB(i))) - (E / (rho_l * RB(i))))); %Solves For Bubble Velocity [m/s]

end %Time Step Loop End
toc %End Timer And Display Duration Elapsed In Seconds

offset_xdata = round((xdata + t(Rmin_index))*1e9)*1e-9; %Offset Experimental Time Points And Round At 1e-9

for j = 1 : length(offset_xdata) %Loops Through Offset Rounded Experimental Time Points

    R_index(j) = find(offset_xdata(j) == t); %Finds Corresponding Time Points To Index Out Viscoelastic Bubble Model Radius

end %Offset Time Points Loop End

R = RB(R_index)'; %Viscoelastic Bubble Model Radius Solved At Experimental Data Time Points
```

B3. Calculation of Strain Field

infinitesimal_finite_strain.m

```
clear all; close all; clc; %Clear All Variables In Workspace, Close All Windows, Clear All Text In Command Window
```

```
ro = (0:200)*1e-6; %Material Coordinates Before Deformation Or In The Initial
Unstrained Configuration [m]
RB = (80)*1e-6; %(Maximum) Bubble Wall Radius After Deformation Or In The
Deformed Configuration [m]

P_vap = 3169; %Vapor Pressure At 25C [Pa]
P_inf = 101325; %Pressure Far Away From The Bubble Or Static Pressure Of
Water [Pa]
Ro = ((RB^3) * (P_vap / P_inf)).^(1/3); %Initial/Equilibrium Bubble Wall
Radius [m]

r = ((ro.^3) - (Ro^3) + (RB^3)).^(1/3); %Material Coordinates After
Deformation Or In The Deformed Configuration [m]

I = eye(3); %3x3 Identity Matrix

for i = 1 : length(ro) %Loops Through Each Material Coordinate Before
Deformation

F = [((ro(i)/r(i))^2), 0, 0; 0, (r(i)/ro(i)), 0; 0, 0, (r(i)/ro(i))];
%Deformation Gradient Tensor

% Ei = ((1/2) * (transpose(F) + F)) - I; %Infinitesimal Strain Tensor
% Ei_radial(i) = Ei(1,1); %Infinitesimal Radial Strain
% Ei_angular(i) = Ei(2,2); %Ei(3,3); %Infinitesimal Angular Strain... Theta
And Phi Are Equivalent

% C = transpose(F) * F; %Right Cauchy-Green Deformation Tensor
% Egl = (1/2) * (C - I); %Green-Lagrangian Finite Strain Tensor
% Egl_radial(i) = Egl(1,1); %Green-Lagrangian Finite Radial Strain
% Egl_angular(i) = Egl(2,2); %Egl(3,3); %Green-Lagrangian Finite Angular
Strain... Theta And Phi Are Equivalent

c = inv(transpose(F)) * inv(F); %Cauchy Deformation Tensor
Eea = (1/2) * (I - c); %Eulerian-Almansi Finite Strain Tensor
Eea_radial(i) = Eea(1,1); %Eulerian-Almansi Finite Radial Strain
Eea_angular(i) = Eea(2,2); %Eea(3,3); %Eulerian-Almansi Finite Angular
Strain... Theta And Phi Are Equivalent

end %Initial Unstrained Material Coordinate Loop End

% Ei_radial(isnan(Ei_radial)) = 0; %Convert NaN To 0
% Ei_radial(isinf(Ei_radial)) = 0; %Convert Infinity To 0

% Ei_angular(isnan(Ei_angular)) = 0; %Convert NaN To 0
% Ei_angular(isinf(Ei_angular)) = 0; %Convert Infinity To 0

% Egl_radial(isnan(Egl_radial)) = 0; %Convert NaN To 0
% Egl_radial(isinf(Egl_radial)) = 0; %Convert Infinity To 0

% Egl_angular(isnan(Egl_angular)) = 0; %Convert NaN To 0
% Egl_angular(isinf(Egl_angular)) = 0; %Convert Infinity To 0
```

```
% Eea_radial(isnan(Eea_radial)) = 0; %Convert NaN To 0
% Eea_radial(isinf(Eea_radial)) = 0; %Convert Infinity To 0

% Eea_angular(isnan(Eea_angular)) = 0; %Convert NaN To 0
% Eea_angular(isinf(Eea_angular)) = 0; %Convert Infinity To 0

% figure(1); %Create Figure 1 - Infinitesimal
% plot(r(Ei_radial ~= 0)*1e6,Ei_radial(Ei_radial ~= 0),'b-'); hold on;
%Infinitesimal Radial Strain Plotted With Deformed Material Points
% plot(r(Ei_angular ~= 0)*1e6,Ei_angular(Ei_angular ~= 0),'r-');
%Infinitesimal Angular Strain Plotted With Deformed Material Points
% plot(RB*1e6,-2:0.05:2,'k--'); hold off; %Vertical Line At (Maximum) Bubble
Wall Radius After Deformation
% xlabel('Deformed Configuration, r [\mum]'); ylabel('Strain [ ]'); %Axis
Labels
% legend('radial','angular') %Legend
% axis([0,200,-2,2]) %Axis Limits

% figure(2); %Create Figure 2 - Finite, Green
% plot(r(Egl_radial ~= 0)*1e6,Egl_radial(Egl_radial ~= 0),'b-'); hold on;
%Green-Lagrangian Finite Radial Strain Plotted With Deformed Material Points
% plot(r(Egl_angular ~= 0)*1e6,Egl_angular(Egl_angular ~= 0),'r-'); %Green-
Lagrangian Finite Angular Strain Plotted With Deformed Material Points
% plot(RB*1e6,-2:0.05:2,'k--'); hold off; %Vertical Line At (Maximum) Bubble
Wall Radius After Deformation
% xlabel('Deformed Configuration, r [\mum]'); ylabel('Strain [ ]'); %Axis
Labels
% legend('radial','angular') %Legend
% axis([0,200,-2,2]) %Axis Limits

figure(3); %Create Figure 3 - Finite, Almansi
plot(r(Eea_radial ~= 0)*1e6,Eea_radial(Eea_radial ~= 0),'b-'); hold on;
%Eulerian-Almansi Finite Radial Strain Plotted With Deformed Material Points
plot(r(Eea_angular ~= 0)*1e6,Eea_angular(Eea_angular ~= 0),'r-'); %Eulerian-
Almansi Finite Angular Strain Plotted With Deformed Material Points
plot(RB*1e6,-2:0.05:2,'k--'); hold off; %Vertical Line At (Maximum) Bubble
Wall Radius After Deformation
xlabel('Deformed Configuration, r [\mum]'); ylabel('Strain [ ]'); %Axis
Labels
legend('radial','angular') %Legend
axis([0,200,-2,2]) %Axis Limits
```

Appendix C. Ca^{2+} Signalling Analysis Software

calcium_signalling_analysis.m

```
clear all; close all; clc; %Clear All Variables; Close All Figure Windows,
Clear Command Window Text

img_list = dir('*.tif'); %Only Lists .tif Files In Current Folder

laser_fire = [568,628]; %Laser Fire Spot Pixel Location, Coordinates In [Y,X]
Or [Row,Column] Format
pixel_conversion = 3.081; %Conversion From Pixels To Micrometers, [pix/um]

[szr,szc] = size(imread(img_list(1).name)); %Determines Image Resolution,
Outputs In [Row,Column] Format
[X,Y] = meshgrid(1:szc,1:szr); %Creates Matrices Correspond To Pixel
Coordinates, [X-Row,Y-Column] Format

pixel_radius = sqrt(((Y - laser_fire(1,1)).^2) + ((X -
laser_fire(1,2)).^2)) ./ pixel_conversion;
%Computes Radial Distance Of Each Image Pixel Relative To The Specified Laser
Fire Spot Pixel Location, [um]
pixel_theta = atan2d((Y - laser_fire(1,1)),(laser_fire(1,2) - X)) + 180;
%Calculates Angle Of Each Image Pixel Relative To The Laser Fire Spot Pixel
Location, [Deg]

angular_divisions = 360 ./ [4, 6, 10, 14, 18, 22, 26, 30, 34, 38, 42, 46];
%Dynamic Angular Divisions, [Deg]

counter1 = 1; %Initiates 1st Counter To Store Sector Indexes
counter2 = 1; %Initiates 2nd Counter To Loop Through Angular Divisions

for i = 25 : 25 : 300 %Loops Through Radial Divisions

    for j = angular_divisions(counter2) : angular_divisions(counter2) : 360
%Loops Through Angular Divisions

        if nnz((pixel_radius > (i-25)) & (pixel_radius <= i) & (pixel_theta >
(j-angular_divisions(counter2))) & (pixel_theta <= j)) >= 1; %Checks If
Actually Saving Sector Pixels, '0 --> No' And '>= 1 --> Yes'

        sector_idx(:,:,counter1) = (pixel_radius > (i-25)) & (pixel_radius <=
i) & (pixel_theta > (j-angular_divisions(counter2))) & (pixel_theta <= j);
%Stores Sector Pixels By Constraining Radial And Angular Divisions
%         sector_edges(:,:,counter1) = edge(sector_idx(:,:,counter1));
%Identifies And Stores Sector Edges
%         sector_centroid(counter1,:) =
round(struct2array(regionprops(sector_idx(:,:,counter1),'centroid')));
%Determines Center Sector Pixel Location
```

```
        counter1 = counter1 + 1; %Increases Sector Index Storage Counter In
Increments Of 1

        end %Check End

    end %Angular Division Loop End

    counter2 = counter2 + 1; %Increases Counter By 1 To Loop Through Angular
Divisions

end %Radial Division Loop End

% edges = sum(sector_edges,3); %Compounds All Sector Edges Into Single
Image/Matrix By 3D Sum
% edges(edges ~= 0) = 1; %Converts All Non-Zero Pixels Into A Value Of 1
% edges = imdilate(edges,strel('square',3)); %Dilates Edge Lines With
Additional Pixels
% figure(); imagesc(edges); colormap(parula); %Create Figure To Check Edge
Image In Parula Colormap

for k = 1 : length(img_list) %Loops Through Calcium Signalling Images

    calcium_img = double(imread(img_list(k).name)); %Reads In Image, Converts
To Double Precision, And Temporarily Stores Intensities

    for l = 1 : size(sector_idx,3) %Loops Through Sectors

        avg_sector_int(k,l) = mean(calcium_img(sector_idx(:,:,l))); %Indexes
Corresponding Calcium Image Intensity Sector Pixels And Computes Average

    end %Sector Loop End

end %Image Loop End

avg_sector_int_ratio =
bsxfun(@rdivide,avg_sector_int,mean(avg_sector_int(1:5,:))); %Compute Sector
Intensity (Average) Ratios... Divide Each Sector Intensity Average
(Progressing With Time/Images) By The Mean Of Sector Intensities Averaged
Over 1:5 Images
max_avg_sector_int_ratio = max(avg_sector_int_ratio); %Finds Maximum
Intensity (Average) Ratio For All Sectors

signal_sector = [11, 13:16, 18, 20,...
                 21:34,...
                 35:52,...
                 53:74,...
                 75:93, 95:99,...
                 100:119, 122:124,...
                 125:131, 132:141, 146:148,...
                 149:153, 155:157, 159, 163:164, 166,...
                 167:169, 171:172, 175:176, 177]; %Hand Counted Signalling
Sector Locations
hand_counted = zeros(1,size(sector_idx,3)); %Preallocates Array Of 0s For
Storing Hand Counted Signalling Sector Positions
```

```
hand_counted(signal_sector) = 1; %Converts Hand Counted Signalling Sector
Positions To A Value Of 1 For Logical Purposes... 0 - No Signal, 1 - Signal

counter3 = 1; %Initiates 3rd Counter To Store Signalling Threshold Ratios,
Code Counted Signalling Sector Positions, And Signalling Sector
Classifications

for m = 1 : 0.01 : str2double(sprintf('%0.2f',max(max_avg_sector_int_ratio)))
+ 0.01 %Loops Through Signalling Threshold Ratios

    signal_threshold_ratio(1,counter3) = m; %Stores Signalling Threshold
Ratios For Plotting

    code_counted(counter3,:) = double(max_avg_sector_int_ratio >= m); %Code
Counted Signalling Sector Positions... Sector Locations With Ratios >=
Threshold Considered Signalled And Assigned A Value Of 1, Otherwise 0 For No
Signalling

    TP = 0; TN = 0; FP = 0; FN = 0; %Initiates Counter To Store Sector
Classifications

    for n = 1 : length(hand_counted) %Loops Through Hand/Code Counted Array
For Conditional Classification Of Signalled Sectors

        if (hand_counted(1,n) == 1) && (code_counted(counter3,n) == 1) %True
Positive Condition

            TP = TP + 1; %Increases True Positive Counter By 1

        elseif (hand_counted(1,n) == 0) && (code_counted(counter3,n) == 0)
%True Negative Condition

            TN = TN + 1; %Increases True Negative Counter By 1

        elseif (hand_counted(1,n) == 0) && (code_counted(counter3,n) == 1)
%False Positive Condition

            FP = FP + 1; %Increases False Positive Counter By 1

        else %(hand_counted(1,n) == 1) && (code_counted(counter3,n) == 0)
%False Negative Condition

            FN = FN + 1; %Increases False Negative Counter By 1

        end %Classification Conditional Statements End

    end %Conditional Classification Loop End

    total_TP(1,counter3) = TP; total_TN(1,counter3) = TN;
total_FP(1,counter3) = FP; total_FN(1,counter3) = FN; %Storing
Classifications Across Varying Signalling Threshold Ratios
```

```
    counter3 = counter3 + 1; %Increases By Counter By 1 To Store Next
Signalling Threshold Ratio, Code Counted Signalling Sector Positions, And
Signalling Sector Classifications

end %Threshold Loop End

figure(1); %Create Figure 1 - Plot Classification Counts
plot(signal_threshold_ratio,total_TP,'bx--'); hold on; %Plot True Positive
Counts And Start Retaining Graph On Current Figure
plot(signal_threshold_ratio,total_TN,'ro--'); %Plot True Negative Counts
plot(signal_threshold_ratio,total_FP,'ks--'); %Plot False Positive Counts
plot(signal_threshold_ratio,total_FN,'md--'); hold off; %Plot False Negative
Counts And Stop Retaining Graph On Current Figure
xlabel('Signal Threshold Ratio'); ylabel('Number Of Sectors'); %Axis Labels
legend('TP','TN','FP','FN','Location','East'); %Legend
axis([0.98,1.42,-5,165]); %Axis Limits

ratio_TPR = total_TP ./ (total_TP + total_FN); %True Positive Rate Or
Sensitivity
ratio_TNR = total_TN ./ (total_TN + total_FP); %True Negative Rate Or
Specificity
ratio_FPR = total_FP ./ (total_FP + total_TN); %False Positive Rate
ratio_FNR = total_FN ./ (total_TP + total_FN); %False Negative Rate
ratio_ACC = (total_TP + total_TN) ./ (total_TP + total_TN + total_FP +
total_FN); %Accuracy

figure(2); %Create Figure 2 - Plot Classification Rates
plot(signal_threshold_ratio,ratio_TPR,'bx--'); hold on; %Plot True Positive
Rate Or Sensitivity And Start Retaining Graph On Current Figure
plot(signal_threshold_ratio,ratio_TNR,'ro--'); %Plot True Negative Rate Or
Specificity
plot(signal_threshold_ratio,ratio_FPR,'ks--'); %Plot False Positive Rate
plot(signal_threshold_ratio,ratio_FNR,'md--'); %Plot False Negative Rate
plot(signal_threshold_ratio,ratio_ACC,'g^--'); hold off; %Plot Accuracy And
Stop Retaining Graph On Current Figure
xlabel('Signal Threshold Ratio'); ylabel('%'); %Axis Labels
legend('TPR','TNR','FPR','FNR','ACC','Location','East'); %Legend
axis([0.98,1.42,-0.05,1.05]); %Axis Limits
```